Magnetic Fluctuations in Heavy Fermion Systems. A Neutron Scattering Study of UPt3, U2Zn17 and URu2Si2

Forskningscenter Risø, Roskilde

Publication date:
1989

Document Version
Publisher's PDF, also known as Version of record

Risø-M-2731

RISØ

Risø-M-2731

Magnetic Fluctuations in Heavy Fermion Systems

A Neutron Scattering Study of UPt_3, U_2Zn_{17} and URu_2Si_2

Collin Leslie Broholm

Risø National Laboratory, DK-4000 Roskilde, Denmark
June 1989

ATTENTION MICROFICHE USER,

The original document from which this microfiche was made was found to contain some imperfections that reduce full comprehension or some of the text despite the good technical quality of the microfiche itself. The failures may be:

- missing or illegible pages/figures;
- wrong pagination;
- poor overall printing quality, etc...

We normally refuse to microfiche such a document and request a replacement document (or page) from the national INIS Centre concerned. However, our experience shows that many months pass before such documents are replaced. Sometimes the Centre is not able to supply a better copy or, in some cases, the pages that were supposed to be missing correspond to a wrong pagination only. We feel that it is better to proceed with distributing the microfiche made of these documents than to withhold them till the imperfections are removed. If the removals are subsequently made then replacement microfiche can be issued. In line with this approach then, our specific practice for microfiching such documents is as follows:

1. A microfiche of an imperfect document will be marked with a special symbol (black circle) on the left of the title. This symbol will appear on all masters and copies of the document (1st fiche and trailer fiches) even if the imperfection is on one fiche of the report only.

2. If the incorrectnesses are not too general the reason will be specified on a sheet such as this, in the space below.

3. The microfiche will be considered as temporary, but sold at the normal price. Replacements, if they can be issued, will be available for purchase at the regular price.

4. A new document will be requested from the supplying Centre.

5. If the Centre can supply the necessary pages/document a new master fiche will be made to permit production of any replacement microfiche that may be required.

The original document from which this microfiche has been prepared has these imperfections:

- [x] missing pages/figures numbered: 63 + 64.
- [ ] wrong pagination
- [ ] poor overall printing quality
- [ ] combinations of the above
- [ ] other

INIS Clearinghouse
I.A.E.A.
P.O. Box 100
A-1400, VIENNA
AUSTRIA

Magnetic Fluctuations in Heavy Fermion Systems

Risø-M-2731

- A Neutron Scattering Study of UPt_3, U_2Zn_{17} and URu_2Si_2

Collin Leslie Broholm

Risø National Laboratory, DK-4000 Roskilde, Denmark
June 1989

Abstract. Magnetic order and fluctuations in the heavy Fermion systems UPt_3, U_2Zn_{17} and URu_2Si_2 have been studied by neutron scattering. Single crystalline samples and triple-axis neutron-scattering techniques with energy transfers between 0 and 40 meV and energy resolutions between 0.1 meV and 4 meV have been employed.

UPt_3 developes an antiferromagnetically ordered moment of $(0.02 \pm 0.005)\ \mu_B$ below $T_N = 5$ K which doubles the unit cell in the basal plane and coexists with superconductivity below $T_c = 0.5$ K. The magnetic fluctuations are relaxational, and enhanced at the antiferromagnetic zone center in a low-energy regime. The characteristic zone-center relaxation energy is 0.3 meV. The temperature- and field-dependence of the antiferromagnetic order in the superconducting phase suggest a close relation between these two properties in UPt_3. U_2Zn_{17} has a broad spectrum of magnetic fluctuations, even below $T_N = 9.7$ K, of which the transverse part below 10 meV is strongly enhanced at the antiferromagnetic zone center. The system has an anomalously extended critical region and the antiferromagnetic phase transition seems to be driven by the temperature-dependence of an effective RKKY interaction, as anticipated theoretically. URu_2Si_2, a strongly anisotropic heavy Fermion system, has a high-energy regime of antiferromagnetically-correlated overdamped magnetic fluctuations. Below $T_N = 17.5$ K weak antiferromagnetic order, $\mu = (0.04 \pm 0.01)\mu_B$, with finite correlations along the tetragonal c axis, develops along with a low-energy regime of strongly dispersive singlet-singlet excitations. Below $T_c = 1$ K antiferromagnetism coexists with superconductivity. A phenomenological model describing the exchange-enhanced overdamped magnetic fluctuations of heavy Fermion systems is proposed. Our experimental results are compared to the anomalous bulk properties of heavy Fermion systems, and to magnetic fluctuations in other metallic magnets.

Dette er en rapport over et licentiatstudium ved Fysisk Centralinstitut, Københavns Universitet. Arbejdet er udført på Fysikafdelingen, Forskningscenter Risø, og vejlederne var A.R. Mackintosh og J.K. Kjems.

This report has been submitted to The University of Copenhagen in partial fulfilment of the requirements for obtaining the lic. scient. (Ph.D) degree.

ISBN-87-550-1445-3
ISSN 0418-6435

Grafisk Service, Risø

Contents

I. Introduction

Correlations in many body systems are at the root of all magnetic phenomena. For this reason many important problems in magnetism remain controversial after decades of scientific effort. One of the most fundamental of these problems is understanding the combination of the strong atomic correlations characteristic of d and f electrons, and the translational degree of freedom associated with a metallic environment.

This cardinal difficulty manifests itself in several interesting fields of metallic magnetism, notably in the study of transition metal magnets, mixed valence systems, Kondo systems and most recently in so-called heavy Fermion systems.

The heavy Fermion systems present particularly challenging manifestations of the long-standing problems in our understanding of metallic magnetism. The experimental study of magnetic fluctuations in heavy Fermion systems is the subject of this thesis. To put heavy Fermion systems and in particular our work into a broader context we will briefly discuss some important concepts in metallic magnetism.

1.1. Conserved Local Moments in Metals

There is an important limit in which the correlated atomic states and the metallic Bloch states, to a large extent, can be treated independently. This situation occurs when the energies associated with the two lowest lying valencies of the localized states bracket the Fermi levels associated with both valence state. Furthermore the interaction energy between localized electrons and the conduction electrons must be much smaller than the separation of the lowest lying valence state from the Fermi level.

This limit is realized in most rare earth metals and leads to the existence of electrons, whose properties are essentially similar to those of the strongly localized 4f states of the free rare earth ion [1,2]. In this case the dynamics of the 4f electrons is governed primarily by atomic correlations arising from the central coulomb potential, intra electronic coulomb repulsion, the Pauli principle and spin-orbit coupling. In a low energy regime of order 0.1 eV the combined spin and orbital moment of the 4f electrons is thus a conserved quantity. This is shown directly by inelastic magnetic neutron scattering experiments in which the dipolar excitation spectra are found to be singular in the whole Brillouin zone [3]. In many ways these systems are similar to insulating magnets, but there are important distinctions concerning the influence of the crystalline environment.

In both cases the anisotropic environment lifts the rotational degree of freedom associated with the free atom. This may be modelled by a single-ion spin-Hamiltonian operator which operates on the Hund's rule ground-state multiplet and has the point-group symmetry of the rare earth ion site. This is the so-called crystal field operator. In magnetic salts the few parameters of this Hamiltonian can be related to the electrostatic fields of the ionic environment by the operator equivalence technique in the point charge model [4].

In metals, the crystal field operator represents the surprisingly simple effect on the local moment of the screened electrostatic fields of neighbouring atoms, and the interactions with conduction electrons [5,6]. Of the latter, the crystal field operator conventionally only involves those which are independent of the crystal field state of the neighbouring atom since, by definition, the crystal field operator is a single ion operator. In some cases the point charge model gives a reasonable first estimate of the parameters in the crystal field operator of a metal. In most cases, however, a first principle calculation cannot be performed and the parameters must be treated as phenomenological parameters to be determined experimentally.

Through the combined effect of the Pauli exclusion principle and the Coulomb interaction of the conduction electrons with the 4f electrons of each rare earth ion, the conduction electrons also induce an effective interaction between the localized moments. This is the so-called RKKY exchange interaction [7]. In most cases it is described by the Heisenberg bilinear exchange operator, in which the many-body nature of the problem is concentrated.

In some cases the conduction electrons and also magnetoelastic effects, can give rise to more

complicated interactions which are anisotropic [8], and may involve more complex combinations of spin operators than the simple bilinear form. In any case the fact that the conduction electron dynamics do not enter explicitly, but only through a small set of parameters, is a beautiful simplification which forms the basis of our near complete understanding of rare earth magnetism [9,10].

1.2. Itinerant Electron Magnetism

When the clear distinction between localized and itinerant electrons cannot be maintained the intricate nature of metallic magnetism is exposed. In this case the magnetic properties of the metal are governed by quasiparticles which form bands with a finite band width, and non-divergent magnetic fluctuation spectra in parts of the Brillouin zone result.

Traditionally itinerant magnetism is separated into several categories. It is fair to say that these categories are most clearly identified by the theoretical development associated with them. It is often harder, and sometimes even meaningless, to categorise a given experimental system in terms of one of these limiting theoretical models. Nevertheless many important physical ideas are contained in these models. We shall briefly discuss some of those which are related to the heavy Fermion systems.

1.2.1. The Anderson Model

A theoretical development of importance to the entire field of metallic magnetism was initiated by the experimental study of the occurence of magnetic moment on iron group ions dissolved in non-magnetic metals [11]. It resulted in the development of the Anderson model [12,13]. This model, in its original form, describes a 3d impurity state subject to on-site Coulomb repulsion of states with opposite spin and to interactions with a free electron band.

A localized moment occurs if the 3d level is placed well below the Fermi level, as compared to $\Delta = \pi < V^2 > \rho(\varepsilon_f)$. Here $< V^2 >$ is a measure of the strength of the 3d electron-free electron interaction, and $\rho(\varepsilon_f)$ is the Fermi surface density of states. On the other hand the doubly occupied singlet 3d state which is placed the energy U above the singly occupied 3d state must be similarly well above the Fermi level.

The crossover between the magnetic and non-magnetic state of the iron group impurity ion is found to be highly non-linearly dependent on the 3 energy scales of the problem. The Anderson model has subsequently been found to be a rather general model of the central problems of itinerant magnetism.

In particular the occurrence of magnetic moments in a concentrated metallic magnet, in which there are strongly correlated localized states on each site of the lattice, may be discussed in terms of an extended version of this model, the Anderson lattice model. Our discussion of the occurrence of conserved local moments in (1.1) was implicitly based on such a model. The situation is however more complicated in a concentrated magnetic system, since the Fermi level depends on the valence of the magnetic ion, as does the localized moment [14,15].

1.2.2. Magnetism in Transition Metals

In magnetic 3d metals the partially occupied 3d levels are so extended that they have significant overlap and form bands, the Fermi surface of which is readily observable by the de Haas-van Alphen effect [16,17].

In this case the so-called Hubbard Hamiltonian [18] is usually the theoretical starting point for describing the magnetic properties. In its simplest form, it describes a single tight-binding band of electrons whose spin degeneracy is lifted by Coulomb interactions between electrons localized at the same site.

The Stoner theory is essentially a Random Phase Approximation (RPA) to the magnetic fluctuations in the Hubbard model [19,20]. In this theory the dipolar excitation spectrum associated with the narrow 3d band is enhanced due to the Coulomb repulsion of 3d electrons occupying the same site.

When the product of this interaction energy and the Fermi surface density of states exceeds a critical value, the metal is ferromagnetic at $T = 0$. In the ferromagnetic state the spin degeneracy of the 3d band is lifted, creating a gap, Δ, between bands associated with each spin state. The transverse response in the ferromagnetic state correspondingly has a long wavelength spin wave regime. At higher momentum transfers the bandwidth of the 3d electrons however give continuous excitation spectra, the so-called Stoner continuum.

Antiferromagnetism can also occur in Stoner theory [19,21]. The ground state which is realized depends on at which Q the enhanced generalized susceptibility diverges. This in turn depends on the non-interacting susceptibility associated with the band structure and in particular the Fermi surface. It seems that antiferromagnetism in general occurs in bands close to half filling. Antiferromagnetism with a generally incommensurate modulation, Q, often denoted a Spin Density Wave (SDW), can result when Q is a characteristic vector of the Fermi surface giving rise to an enhanced non-interacting susceptibility corresponding to this modulation. Such a model was proposed by Overhauser to account for the incommensurate SDW in chromium [22,23,24].

The magnetic excitations in the Stoner model of itinerant antiferromagnetism have a low energy regime with a spinwave-like response which crosses into a continuum at higher momentum transfers. Only in the case of Fermi surface nesting is the long wavelength response however truly singular. In general the imaginary part of the enhanced generalized susceptibility is finite in an itinerant antiferromagnet even in the long wavelength regime and spin waves thus have a finite lifetime [21]. We shall return to this point in 3.

Stoner theory gives a correct picture of the ground state properties but cannot account for finite temperature properties [19]. In particular the ferromagnetic transition temperature is overestimated by up to an order of magnitude. In the simple Stoner theory the only temperature dependence of the response arises from the broadning of the Fermi-Dirac distribution function at the Fermi level. It seems that the deficiencies of the Stoner theory at finite temperatures arise because the renormalization of the ground-state associated with the thermal excitation of magnetic fluctuations is not taken into account.

This is done explicitly by Moriya in the so-called Self Consistent Renormalization (SCR) theory of itinerant magnetism [19], and by several others in related theoretical approaches [25]. The SCR theory has had considerable success in predicting and accounting quantitatively for a large variety of experimental results [19]. Most notably the SCR theory can account for the Curie Weiss susceptibility of an itinerant magnet without invoking the concept of localized moments. More detailed experimental studies of magnetic fluctuation in weak itinerant ferromagnets observed by neutron scattering and the associated mass enhancement of conduction electrons observed by the de Haas-van Alphen effect have also been successfully analysed in terms of the SCR and related theories [25].

1.2.3. Itinerant f-Electron Systems

A somewhat different approach is usually taken to describe f electron metallic magnets in which the simple atomic Hund's rule ground-state multiplet is not approximately conserved in the metallic environment (1.1). The f electrons (especially the 4f electrons) are certainly also much more localized than d electrons, and the interatomic correlation energies much larger than the f electron band-width. The physical description of such systems tend to distinguish between localized f states and conduction electron bands, although ultimately this is not possible.

The Anderson Lattice model is usually the basis for describing these systems. As discussed earlier this model can describe the interaction of localized f electrons, subject to strong interatomic Coulomb repulsion, with a band of free conduction electrons. In general if the two lowest valence states f^n and f^{n-1} are close in energy and close to the Fermi levels associated with ionization level, a so-called intermediate valence system results [14]. In such systems neither the one, nor the other valence state of the f shell is the ground state at $T = 0$. Real charge and spin fluctuations result, and give rise to a narrow band of predominantly f character situated close to the Fermi level, a large linear electronic contribution to the specific heat, and a non-magnetic ground state. The situation occurs most often in compounds of cerium, thulium, ytterbium, samarium and europium [26,27]. At high temperatures the Curie-Weiss susceptibility of these compounds can be accounted for as a combination of contributions from each of the competing valence states. Neutron scattering shows that the spin fluctuation spectra in these compounds are very different from those of metallic magnets with conserved local moments. The spectra are relaxational, with typical relaxation energies of the order 50 meV and often temperature-independent in a large temperature range.

In the limit when the competing valence states have larger separation in energy, real charge fluctuations are suppressed, and the so-called Kondo limit results [15]. In this limit the conduction electron - local moment interaction may be modelled by a spin Hamiltonian, the so-called Kon-

do Lattice Hamiltonian which may be obtained from the Anderson Lattice Hamiltonian in the Kondo limit by the Schrieffer-Wolf transformation [28].

The single-site version of the problem, the Kondo problem, has been solved exactly theoretically [29]. The single impurity Kondo systems are characterized by a logarithmic increasing resistivity for decreasing temperatures due to the formation of a compensating conduction electron spin polarization around the impurity spin. A single energy scale $k_B T_K$ governs the single impurity problem. In particular the spin fluctuations are relaxational with this characteristic energy scale.

The Kondo lattice problem is more complicated since an effective local moment interaction, the RKKY interaction, is also induced by the interactions with conduction electrons. This leads to a competition between the formation of a magnetically ordered ground state and a correlated singlet ground state. This has been studied theoretically in a two impurity model by Jones and Varma [30], and in a simplified Kondo lattice model by Coleman and Andrei [31].

We briefly mention that many of the ground states of itinerant magnetism discussed here find their simplest description within Landau's Fermi liquid theory. This general phenomenological theory describes the low temperature properties of an interacting Fermi system in terms of a set of parameters characterizing the quasiparticles, or elementary excitations of the system [32,33].

1.3. Heavy Fermion Systems

The classical concepts of itinerant magnetism gained renewed interest in the beginning of the eighties when a group of metallic magnets with particularly provoking properties was discovered [34].

Low temperature electronic specific heat enhanced by up to 3 orders of magnitude was what first aroused the interest of investigators in these materials. They were called heavy Fermion systems since this large low temperature electronic entropy, in a Fermi liquid description, corresponds to a quasiparticle mass similarly enhanced over the free electron mass.

Table 1.1 lists most of the heavy Fermion systems and some of their typical anomalous pro-

Table 1.1. Some characteristic properties of the most widely studied heavy Fermion systems. Literature references are given in paranthesis after each number. Numbers separated by a slash in one column correspond to measurements in the basal plane and along the unique c-axis of anisotropic structures.

Compound	$\gamma(0)$ [mJ/mole-K^2]	$\chi(0)$ [10^{-3} emu/mole]	μ_{eff} [μ_B]	θ_{cw} [K]	μ_{ord} [μ_B]	T_N [K]	T_c [K]
$CeAl_3$	1620 [35]	36 [35]	2.63 [35]	- 39 [36]	+	+	+
$CeCu_6$	1300 [37]	27 [38]	2.69 [38]	- 45 [38]	+	+	+
UAl_2	142 [39]	4.4 [40]	3.1 [40]	-245 [40]	+	+	+
$UAuPt_4$	725 [41]				+	+	+
UCd_{11}	840 [42]	3.84 [42]	3.45 [42]	-23 [42]		5 [42]	+
UCu_5	> 250 [43]		see ref.[44]		0.9 [57]	15.2 [43]	+
$U(Pt_{0.95}Pd_{0.05})_3$	500 [45]	14/5.9 [45]	2.8 [45]	-44/-190 [45]	0.6 [58]	6 [45]	+
$U_{0.95}Th_{0.05}Pt_3$	430 [46]				0.65 [47]	7 [47]	+
U_2Zn_{17}	500 [48]	9 [48]	3.3 [49]	-95/-130 [49]	0.81 (3.2.1)	9.7 [48]	+
$CeCu_2Si_2$	1000 [50]	11.8/19.8 [51]	2.75/2.54 [51]	-175/0 [51]	+	+	~0.65 [50]
UBe_{13}	1100 [43]	15 [43]	3.1 [43]	- 53 [43]	+	+	~0.9 [43]
UPt_3	450 [52]	8.55/4.46 [53]	2.5/2.4 [53]	-39/-151 [53]	0.02 (2.2.2)	5 [54]	0.5 [52]
URu_2Si_2	180 [55]	1.2 /4.9 [55]	+/3.5 [55]	+/-65 [55]	0.04 (4.2.1)	17.5 [55]	~1 [55]
$U_{0.97}Th_{0.03}Be_{13}$	1100 [56]					0.4 [56]	0.6 [56]
Na	1.5 [59]	0.024 [60]	+	+	+	+	+

perties. Sodium is included as a reference. Paramagnetic, Antiferromagnetic and Superconducting ground states occur, often with an extreme sensitivity to the introduction of non-magnetic impurities. Heavy Fermion systems have until now been found exclusively among metals containing either cerium or uranium. Cerium and uranium are the lightest magnetic elements of the 4f and 5f series, respectively. There is a general consensus of agreement that the heavy Fermion properties are related to the participation of 4f or 5f electrons in metallic properties.

We have already mentioned that cerium in some compounds has intermediate valence. When it does, it fluctuates between the magnetic $4f^1$ and the nonmagnetic $4f^0$ state. In the elemental fcc metal cerium the reduction of the unit cell volume by 20% below about 100 K is usually associated with the delocalization of the 4f electrons which then form narrow bands[61]. Cerium is also known to give rise to the single impurity Kondo effect when introduced as an impurity in metals, for example in the $La_{1-x}Ce_xB_6$ system [62].

The magnetism of the actinides has not been studied to the same extent as that of the rare earth systems [63]. Although the magnetic properties of both series are governed by f electrons, there are many important differences. Even the L-S coupling scheme is questionable for the actinides, and intermediate coupling may be necessary [64]. The 5f states become increasingly localized for the heavier elements and metals with actinides heavier than americium are believed to have conserved local 5f moments. This is suggested by a sharp increase of the lattice parameter for the heavier elemental actinide metals at americium. The continuously increasing trend of lattice parameters towards the lighter elemental actinide metals is however similar to the elemental transition metal series [63]. The 5f states of uranium are indeed somewhat more delocalized than the 4f states of the heavy rare earths and for uranium-uranium separations less than the so-called Hill limit [65], d = 3.25-3.5 Å, they form bands leading to paramagnetic uranium compounds. for uranium-uranium separations larger than this limit, as is for example the case in the uranium based heavy Fermion systems, most systems have a magnetic phase-transition, but singular magnetic response in the whole Brillouin zone is the exception rather than the rule in inelastic magnetic neutron scattering experiments [66]. Only in the singlet ground state system UPd_3, which undergoes quadropolar transitions at 5 K and 7 K [67] does it seem that the 5f electrons are confined to a single valence state, $5f^2$, and give rise to a conserved local moment [68].

In most magnetic uranium systems the magnetic excitations are more reminiscent of transition metal magnets with broad spectra showing the existense of quasiparticle bands with large 5f contributions. Only at the zone centers of magnetically ordered systems are singular responses in general observed [66]. Also the comparison of magnetism in uranium systems to transition metal magnetism however has its restrictions. In particular, beyond the Hill limit direct 5f-5f overlap is expected to be negligible and 5f-6d hybridization is responsible for the development of magnetic quasiparticle bands. Furthermore spin orbit coupling is larger than crystal field effects in 5f systems, contrary to the case for the transition metals.

Experimental and theoretical work on heavy Fermion systems has been concentrated on elucidating the nature and the origin of the low temperature paramagnetic or weakly antiferromagnetic state with the characteristic large electronic entropy. Analogies to almost all types of metallic magnetism have been proposed. Particularly popular has been the idea of heavy Fermion systems as concentrated Kondo systems. The experimental justification for this picture is the occurence at high temperatures of a Curie-Weiss susceptibility, which is usually associated with a paramagnetic local moment system, and the simultaneously increasing resistivity with decreasing temperature. The resistivity maximum observed in most heavy Fermion systems at lower temperatures is then associated with the increasing correlations of conduction electron scattering processes from neighbouring local moments.

From theoretical work there is also some support for these ideas, in particular from the work on the two-impurity Kondo problem mentioned previously. No doubt the theoretical description, and with it the rigorous understanding of heavy Fermion systems, is at an early stage, and still allows for exciting experimental discoveries.

1.4. The Scope of This Work

This thesis presents an experimental neutron scattering study of the magnetic order and fluctu-

ations in three heavy Fermion systems, UPt_3, U_2Zn_{17} and URu_2Si_2. The emphasis is on the exposition of qualitative features of the magnetic fluctuations in these systems, which we believe to be of importance in our understanding of heavy Fermion behaviour.

Our choice of experimental systems has also been governed by this criterion although the relatively short time available for our work made the sample availability an important issue too. Although we attempt to relate our neutron scattering data to the anomalous bulk properties of heavy Fermion systems, we do not give a thourough review of these, nor do we discuss the many theoretical advances made recently in detail. This is because we wish to concentrate on the direct results of our experimental contribution. We refer the reader to recent experimental [34,49] and theoretical [69] reviews, and will also give frequent references to original work in the following chapters.

After a short introduction to magnetic neutron scattering, the thesis is organised as 3 independent chapters concerning each of the uranium-based heavy Fermion systems which we have studied.

Chapter 2 concerns UPt_3 and focuses on the low energy magnetic fluctuations and proximity to antiferromagnetism of this compound. We also show experimental results proving a close relation between the antiferromagnetic and superconducting properties of UPt_3.

Chapter 3 describes our results of neutron scattering from U_2Zn_{17}. We regard this compound as a typical heavy Fermion antiferromagnet (T_N = 9.5 K) and have the most complete discussion of this phenomenon here. We also describe a model which we have developed for the magnetic fluctuations of heavy Fermion systems and with success applied to the low energy magnetic excitations in U_2Zn_{17}.

In Chapter 4 we present and discuss our experimental results on the heavy Fermion antiferromagnet and superconductor URu_2Si_2. Apart from demonstrating the coexistence of antiferromagnetism and superconductivity in this compound, our result show a facinating and complicated combination of crystal field effects and itinerant magnetism in URu_2Si_2.

We have attempted to separate the description of our experimental work from the analysis and discussion of it. Furthermore each chapter has a summary and Chapter 5 contains the conclusions of our work.

1.5. Magnetic Neutron Scattering

The neutron is a neutral spin ½ particle with a dipolar moment of $5 \cdot 10^{-4}\ \mu_B$. It interacts weakly, primarily through short range nuclear forces with the atomic nucleus, and through dipolar forces with the spin and orbital moment of the electrons [70,20]. The latter interaction makes neutron scattering a unique tool for providing detailed microscopic information on the magnetic excitations of electron systems. The scattering cross section associated with this interaction can be written [20]:

$$\frac{\partial^2\sigma}{\partial\Omega\partial E} = \frac{k_f}{k_i}\left(\frac{1}{2}r_o\right)^2 \cdot \exp(-2W(\varkappa))\frac{N_m}{\pi\mu_B^2} \mid F_m(\varkappa)\mid^2 \cdot (n(\hbar\omega)+1)Im\{\chi^{\perp}_{\varkappa}(\omega)\} \tag{1.1}$$

where $\hbar\varkappa = \hbar(\mathbf{k}_i - \mathbf{k}_f)$ is the momentum transfer, and $\hbar\omega = \hbar^2(k_i^2 - k_f^2)/2m$ is the energy transfer from the neutron to the sample. The mass of the neutron $m = 1.67 \cdot 10^{-27}$ kg, sets the scale of energy transfer conveniently in the meV regime for momentum transfers of order 1 Å^{-1}. In fact the quasiparticle mass in heavy Fermion systems is within an order of magnitude of the neutron mass which makes neutron scattering from these particularly informative as compared to scattering from band electrons of normal metals.

Formula (1.1) is discussed in mathematical detail in Appendix A.3. Here we shall only mention a few points which are of importance for understanding our experimental work.

Since the dipolar interactions are weak the scattered neutron intensity in a practical experiment in most cases may be assumed to be linearly related to the cross section (1.1). If the resolution of the experiment is furthermore sufficiently good, the scattered neutron intensity is essentially proportional to the scattering cross section (1.1). (See Appendix A.1 concerning the effect of finite experimental resolution).

The first line of (1.1) is slowly varying with $\varkappa$ and $\hbar\omega$ and primarily of importance when normalizing scattered neutron intensities to measure the absolute value of the cross section giving rise to the scattering (see Appendix A).

In the second line $|F_m(\varkappa)|^2$ is the magnetic formfactor of the spin and orbital density [20]. It is essentially the squared Fourier transformed density normalized to 1 at $\varkappa = 0$, and it falls off

at larger $\varkappa$ with a characteristic half width which is inversely proportional to the spatial extent of the scattering spin and orbital moment density [71]. For the 5f electron of uranium this half width is typically 3 Å^{-1}. For s and p electrons it is however only a fraction of an Å^{-1}. In our experimental work $\varkappa$ is typical of the order 1 Å^{-1} and we therefore are primarily probing the part of the spin and orbital moment localized within an Å or so.

We have expressed (1.1) in terms of the complex generalized susceptibility $\chi_\varkappa(\omega)$ associated with spin and orbital moment [72]. For the 4f and 5f electrons the spin-orbit coupling is strong and confines the spin and orbital moment to a definite relative orientation given by Hunds rules in an energy regime below $\sim$ 0.1 eV. $\chi_\varkappa(\omega)$ is then the response function associated with the resulting effective moment. Note however that our experiments do not distinguish spin and orbital moment nor do they directly access the strength of the spin-orbit coupling.

The superfix $\perp$ to $\chi_\varkappa(\omega)$ in (1.1) indicates that magnetic neutron scattering probes the response of the projection of the moment density on the normal plane to the scattering vector $\varkappa$. This property of the dipolar interaction may be used to determine the polarization of the magnetic fluctuations. Polarized neutron scattering involves stricter selection rules enabling a complete determination of the polarization of the magnetic fluctuations [73,20]. This is utilized experimentally in 3.2.1 and 3.2.3, but will not be discussed further here.

The magnetic neutron scattering is covenient-ly related to the bulk susceptibility by (1.1). The bulk susceptibility is simply the real part of the generalized susceptibility in the limit $\varkappa,\omega \to 0$. Since $\chi_\varkappa(\omega)$ is an analytical function the real and imaginary parts are related by the Kramers Krönig relation. In particular:

$$\chi_{bulk} = Real\{\chi^{\parallel}_{o}(0)\} = \frac{1}{\pi}\int_{-\infty}^{\infty}\frac{d\omega}{\omega} Im\{\chi^{\parallel}_{o}(\omega)\} \tag{1.2}$$

The superscript $\parallel$ indicates that obviously a bulk susceptibility measurement is related to the generalized susceptibility along the direction of the applied field.

Another rigorous mathematical relation associated with (1.1) is the so-called total-moment sum-rule:

$$\langle M^2\rangle = \frac{1}{\pi N_m}\cdot\sum_{q}\int_{-\infty}^{\infty} d\omega\langle n(\hbar\omega)+1\rangle Im\{Tr\chi_q(\omega)\} \tag{1.3}$$

which simply relates the total magnetic neutron scattering to the size of the moment giving rise to the scattering. (1.2) and (1.3) are useful to make contact with bulk measurements. They both require normalization of the scattered neutron intensity as described in Appendix A.

The magnetic neutron scattering cross section has an explicit temperature dependence given by

$$\langle n(\hbar\omega)+1\rangle = (1-\exp(-\beta\hbar\omega))^{-1} \tag{1.4}$$

where β is the inverse thermal energy. This is the so-called detailed-balance factor. It should be distinguished from the temperature dependence of the spin dynamics which is contained in $\chi_\varkappa(\omega)$. The detailed balance factor accounts for the relation between dissipation and fluctuations through the so-called fluctuation-dissipation theorem of which (1.1) essentially is an example.

For $|\hbar\omega| >> 1/\beta$ there are two limits of the detailed balance factor depending on the sign of the energy transfer:

$$\lim_{\beta\hbar\omega\to+\infty}\langle n(\hbar\omega)+1\rangle = 1$$

$$\lim_{\beta\hbar\omega\to-\infty}\langle n(\hbar\omega)+1\rangle = 0^{-}$$

for positive energy transfers much larger than the thermal energy the spectrum of the magnetic neutron scattering cross section is thus given directly by the imaginary part of the generalized susceptibility. For negative energy transfers much larger than the thermal energy the detailed balance factor and thus the magnetic neutron scattering cross section vanishes. Physically this is because negative energy transfer corresponds to the neutron receiving energy from the sample. Obviously only energy quanta up to roughly k_BT are available, so scattering with negative energy transfers significantly larger than k_BT does not occur. For $|\hbar\omega| \lesssim k_BT$ the temperature and energy dependence of the scattering cross section (1.1) is significantly influenced by the detailed

balance factor. The scattering is enhanced at energy transfers of the order k_BT and below. This may be thought of as due to the increasing population of excited states in this energy regime. In particular we have

$$\lim_{|\hbar\omega|\to 0}(n(\hbar\omega)+1)=\frac{k_BT}{\hbar\omega}$$

if $\mathrm{Im}\{\chi_\alpha(\omega)\}$ is non-divergent as $\omega \to 0$, the divergence at $\hbar\omega = 0$ is of course removed in the neutron scattering cross section (1.1), since in general $\mathrm{Im}\{\chi_\alpha(\omega)\} = -\mathrm{Im}\{\chi_\alpha(-\omega)\}$.

Finally we estimate the absolute size of the magnetic neutron scattering cross section (1.1). From (1.3) the integral of the two last terms in (1.1) arising from the scattering from the spin of an electron is $\pi\mu_B^2$. Inserting in (1.1) we find that the total scattering cross section associated with the spin of an electron is roughly $(\frac{1}{2}r_o)^2 = 7.3\cdot10^{-2}$ b. This is only about an order of magnitude less than that associated with nuclear scattering. Whether or not magnetic scattering is observable however depends on to what extent the magnetic fluctuations associated with spin and orbital moment are spatially and temporaly correlated. In normal metals where the energy scale of spin flip excitations may be taken as $\epsilon_f \sim 10$ eV thermal magnetic neutron scattering is infeasible. On the other hand in rare earth magnets where the energy scale of magnetic fluctuations is set by the RKKY interactions magnetic neutron scattering is readily observable. Heavy Fermion systems also in this aspect represents a borderline case which is an experimental challenge.

2. Antiferromagnetism and Superconductivity in UPt_3

Both experimental and theoretical work have shown that UPt_3 is close to an antiferromagnetic instability. Susceptibility measurements reveal a negative Curie Weiss temperature of -200K [74,75], and the susceptibility does indeed go through a maximum at around 20K but without a phase transition occurring. Inelastic neutron scattering showed that the bulk susceptibility maximum was associated with development of antiferromagnetic correlations in quasielastic magnetic fluctuations which extend beyond 10 meV [76]. Of theoretical work we mention band structure calculations by Norman et al. [77] which indicate that the ground state of UPt_3 is antiferromagnetic with an ordered moment of 0.8 μ_B.

The clearest manifestation of the proximity of UPt_3 to antiferromagnetism was found when doping the compound with Pd or Th. Such compounds were found to undergo a phase transition at $T_N \sim 6K$ [78,46,79] which by neutron scattering was shown to bring the compound into an antiferromagnetic state [47,58]. The ordered moment is about 0.6 μ_B for both dopants, close to that predicted by band structure calculations of pure UPt_3 [77]. Most remarkably, only doping of the order 5 atm% was needed to invoke this phase transition.

It was surprising that the antiferromagnetic order obtained in the doped compounds had an associated modulation in the basal plane of the hexagonal structure, whereas neutron scattering showed antiferromagnetic correlations of quasielastic scattering along the hexagonal c axis in the pure compound.

In the light of these experimental results we performed low energy elastic and inelastic magnetic neutron scattering experiments to study magnetic fluctuations of pure UPt_3 for modulations at which doped samples order. We found that even our pure high-quality single crystals of UPt_3 developed antiferromagnetic order below 5K though with an exceedingly small ordered moment of just (0.02 ± 0.01) μ_B.This was previously suggested by muon spin relaxation measurements [80].

We also found that the low-energy magnetic fluctuations were strongly enhanced at the corresponding antiferromagnetic zone centers, and that despite the absence of large anomalies in the heat capacity these fluctuations evolve around T_N reminiscent of critical scattering, albeit with an anomalous extended critical region. Some of these results have previously been published [81,82].

The superconductivity of UPt_3 has also been studied extensively and both experimental [83,84,85,86,87] and theoretical work [88,89,90,91,92] suggest that it is not of the conventional BCS singlet type. The proximity of antiferromagnetism has led to suggestions that magnetic fluctuations play a role in establishing an effective attractive electron-electron interaction, and that the distinct symmetry of such interactions as compared to that of phonon mediated interactions, leads to the anomalous superconducting ground state. Any relation between microscopic magnetic properties and superconductivity are thus highly interesting since they lend support to these ideas.

In a very careful polarized neutron scattering study by C. Stassis et al. [93] it was shown that the moment induced by an applied field is predominantly f like and does not change through the superconducting phase transition in the heavy Fermion superconductors UPt_3, UBe_{13} or $CeCu_2Si_2$. This is contrary to the case in V_3Si where the spin contribution from d bands to the susceptibility was found to vanish at T_c [94]. The null result in the heavy Fermion systems is surprising when considering that the entropy change at the superconducting phase transition is enhanced as is the electronic contribution to the specific heat, which is thought to arise from magnetic fluctuations of 5f electrons.

We have studied low energy magnetic fluctuations and the small ordered moment of pure UPt_3 through the superconducting phase transition, and found evidence of a relation between the antiferromagnetic and superconducting properties of this compound.

2.1. Sample and Experimental Technique

UPt_3 has the hexagonal Ni_3Sn structure (space group $P6_3/mmc$) with one non-symmetry given parameter which determines the position of the 6 Pt atoms in the unit cell [95] the lattice parameters are a = 5.753 Å and c = 4.890 Å at T = 4.2 K. We express momentum transfers in units of $a^* = 4\pi/a\sqrt{3} = 1.261$ Å^{-1} and $c^* = 2\pi/c = 1.285$ Å^{-1}. Experiments were carried out for momentum transfers in the (h0l) and (hk0) plane.

Four approximately cylindrical (d ~ 6 mm, *l* ~ 50 mm) ingots of UPt_3 were grown for us by E. Bucher et al. [96]. using the float-zone method. The crystals had their c axis along the cylinder axis.

In the light of the extreme sensitivity of UPt_3 to doping and impurities our samples were analyzed for chemical impurities by inductive coupled plasma mass spectrometry, which showed that the general impurity level is below 10 ppm. Specifically the weight percentages of various elements are: Pd < 1 ppm, Th < 1 ppm, Rh ~ 1 ppm, Al < 10 ppm, ^{211}Pb, ^{119}Sn < 10 ppm, V ~ 1 ppm. Most of the single crystalline material was however found to have stacking faults giving rise to substantial resolution-limited nuclear scattering from the forbidden (001) reciprocal lattice point. Streaks of nuclear scattering along a* demonstrated the disordered nature of these stacking faults.

The 4 ingots were parted into several pieces. In experiments where low mosaic distribution was important only one single crystal was in the neutron beam. For probing weak magnetic fluctuations and for accurate measurements of the temperature and field dependence of the ordered moment 4 - 5 single crystalline specimens were brought into the beam so as to increase the total scattering. The crystals were aligned so that their crystallographic axis coincided typically to within 0.5° in the scattering plane and within 2° perpendicular to the scattering plane.

In most of our experiments a significant contribution to the background was incoherent scattering. It was crucial to minimize the contribution to this type of scattering from the sample mount. This was done by keeping the sample mount well out of the beam and shielding it by neutron-absorbing cadmium. The samples were glued to the copper holder with low temperature varnish.

In experiments related to the superconducting phase transition, AC susceptibility was measured simultaneously with the neutron scattering experiment on a small UPt_3 single crystal similarly mounted but placed outside the neutron beam. The superconducting transition was in this way found to occur at T_c = 0.5 K. The AC susceptibility evolved within 0.05 K at T_N.

Measurements of magnetic fluctuations in the normal state were done in a standard pumped ^{3}He cryostat, while measurements in the superconducting phase were performed in an Oxford instrument ^{3}He-^{4}He dilution cryostat with a cooling power of 250 μW at 100 mK.

The neutron scattering experiments were performed at triple-axis spectrometers at the H_2 cold source of the DR3 reactor at Risø National Laboratory. PG (002) crystals were used as monochromators and analyzers. The monochromator was vertically focused, and the analyzer, in inelastic experiments horizontally focused, thus relaxing the momentum resolution while maintaining good energy resolution. The acceptance angle of our focusing analyzer was typically 5°.

Table 2.1. Experimental configurations used in experiments on UPt_3. The column denoted "crystal(s)" states which crystals were in the beam. Each crystal is identified with a letter.

Config.#	Reactor	Instrument	Crystal(s)	E_f [meV]	Collimation	Monoch	Analyzer	Filter	ΔE[meV]
1	Risø-DR 3	TAS 7	ABCDE	5.1	20'-open-open-open	PG(002)	PG(002) focused	Be	0.2
2	Risø-DR 3	TAS 7	ABCDE	3.74	20'-30'-open-open	PG(002)	PG(002) focused	Be + BeO	0.1
3	Risø-DR 3	TAS 6	D	4.47	60'-36'-52'-66'	PG(002)	PG(002)	Be + 2PG	0.15
4	Risø-DR 3	TAS 7	E	4.47	20'-open-53'-66'	PG(002)	PG(002)	Be + 2PG	0.15
5	Risø-DR 3	TAS 7	ABCD	5	20'-open-open-open	PG(002)	PG(002)	2Be	~0.2
6	Risø-DR 3	TAS 7	ABCD	5	20'-open-24'-open	PG(002)	PG(002)	2Be	~0.15

PG, Be and BeO filters were used to suppress higher order neutrons. We also used the Be and BeO powder filters to modify the shape of the incoherent energy resolution. When using a focused analyzer, the energy resolution of the analyzing system is somewhat coarser than that of the monochromator. In particular, the energy acceptance function can have non-gaussian tails. This makes the discrimination towards elastic scattering at small energy transfers worse than can be obtained with a conventional collimated crystal analyzer. By placing a powder filter in the scattered beam and choosing the fixed energy of the analyzer slightly above the cutoff of the filter, the energy acceptance of the analyzing system has an essentially infinitely sharp cutoff towards higher neutron energies. In this way the discrimination towards elastic scattering at small positive neutron energy transfers is given by the better energy resolution of the monochromator.

In the following chapter, the experimental configuration adopted for each set of data will be stated by reference to Table 2.1.

2.2. Experimental Results

Our experimental results are described in four sections dealing with the low temperature magnetic fluctuations, the weak antiferromagnetic order, the antiferromagnetic phase-transition, and finally the superconducting phase-transition. Discussion and analysis is concentrated in Chapter 2.3.

2.2.1. Low Temperature Magnetic Fluctuations

Figure 2.1 shows low-temperature constant q scans at q = (½01) and q = (001). (½01) is an antiferromagnetic Bragg point of the doped compounds. At (001) the scattering probes antiferromagnetic fluctuations of neighbouring hexagonal basal planes. A previous neutron scattering experiment found that fluctuations of this nature dominated at energy transfers of $\hbar\omega \sim 8$ meV [76]. The data of Figure 2.1 were taken with configuration # 1 of Table 2.1. The temperature dependence of the scattering (2.2.3) and the decrease of the scattering at higher momentum transfers leads us to conclude that we are probing magnetic fluctuations.

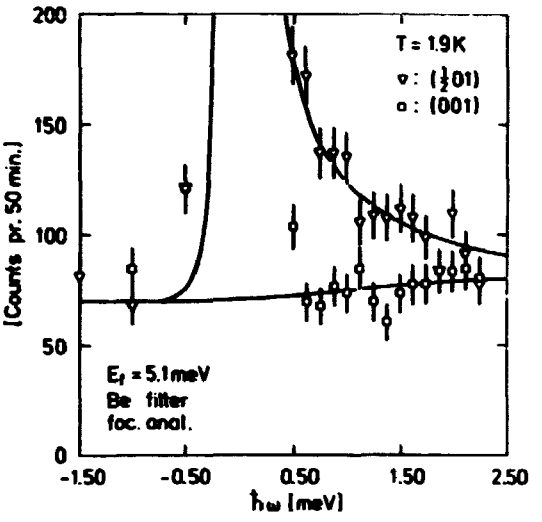

Figure 2.1. Constant q scans in UPt_3 at momentum transfers (½01) and (001) and T = 1.9 K. The solid lines are the result of a model of the generalized susceptibility of UPt_3 similar to that described in 3.3.1.

From the figure we find that there is an enhanced low-energy quasielastic response in pure UPt_3 at the antiferromagnetic zone centers of the doped systems. In particular, in the energy regime below $\hbar\omega = 2$ meV the quasielastic scattering at (½01) is much stronger than that at (001). As was shown in [76], at higher energies the picture is reversed.

The energy resolution of this experiment, $\Delta E \sim 0.2$ meV (FWHM), does not allow us to deduce a characteristic energy scale for the fluctuations at (½01), only to say that the associated relaxation energy $\hbar\Gamma \lesssim \Delta E = 0.2$ meV.

Similar low energy response was found at symmetrically equivalent reciprocal, lattice points and with associated integrated intensities in similar ratios as was found for the antiferromagnetic Bragg peaks of the doped compounds. In particular no low energy response was found at (½00) which is symmetrically equivalent to (½01). This shows that the fluctuations probed at (½01) are polarized along the direction in which the unit cell is doubled.

To study the detailed q dependence of the enhanced magnetic fluctuations close to (½01), we performed the constant energy scans shown in Figure 2.2. The enhanced low energy response

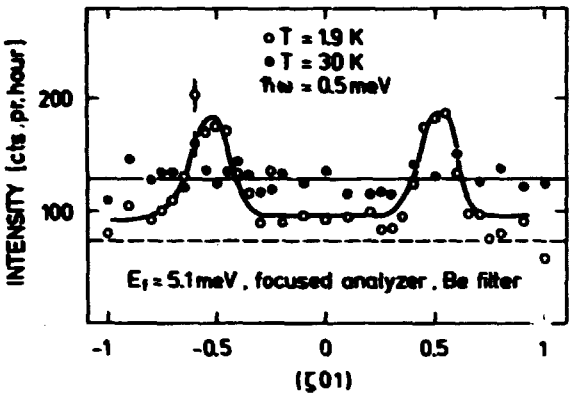

Figure 2.2. Constant energy scans in UPt_3 at $\hbar\omega$ = 0.5 meV and at temperatures T = 1.9 K and T = 30 K. The dashed line is the background level as measured for neutron energy gain.

shows up as peaks at reciprocal lattice points corresponding to doubling of the unit cell in the basal plane. The fact that this q dependent quasielastic scattering has the translational symmetry of the reciprocal lattice of UPt_3 shows that it indeed arises from the sample and not from a spurious process. From the width of the peaks in Figure 2.2 we deduce that the antiferromagnetic fluctuations in this low energy regime are correlated over roughly 5 unit cells. The figure also shows the same scan taken at T = 30 K. The correlations are found to vanish at higher temperatures and the overall level of scattering increase. We shall return to this point in 2.2.3.

We can calculate the amount of moment participating in these fluctuations by normalizing the magnetic scattering to that of longitudinal acoustic phonon scattering (Appendix A), and estimating the energy and momentum integrated intensity of the response at (½01). From Figures 2.1 and 2.2. We obtain $<m_q^2> \sim (0.1\mu_B/\text{U-atom})^2$. We cannot, however, from the data of Figure 2.3 get a reliable estimate of the real part of the staggered susceptibility at (102) since the insufficient energy resolution does not allow us to access the low-energy region with largest contributions to the Kramers-Krönig integral of formula 1.2.

To determine the energy scale associated with these fluctuations we increased the resolution of our spectrometer by reducing the energy to which the analyzer was tuned (configuration # 2 of Table 2.1). We also used a BeO filter to sharpen the energy cutoff of the analyzing system as described above.

Figure 2.3 shows the result of this measurement. The top frame shows raw data at two momentum transfers and temperatures. for $\hbar\omega >$ 0.15 meV the data at q = (0.301) is indistinguishable from the fast neutron background as measured with the analyzer turned away from reflection. There is thus no significant magnetic con-

Figure 2.3. Constant q scans in UPt_3 at (0.53 0 l), T = 0.5 K and T = 5 K, and (0.3 0 l) at T = 0.5 K

a) Shows the raw data. The elastic peak is nuclear incoherent scattering. The dotted line through this peak is a first principle calculation, based on Reference [150], of the asymmetric response of the specially filtered spectrometer configuration used (E_c(BeO) = 3.765 = E_f + 0.03 meV). The broken line is the analyzer turned background. The full lines are guides to the eye.

b) The inelastic magnetic scattering at (0.53 0 l) deduced by subtracting the background as measured at (0.3 0 l). The procedure is detailed in the text. The lines through these data are resolution corrected Lorentzian relaxation spectra with $\Gamma_{(0.53\ 0\ l)}$(0.5 K) = (0.31 ± 0.03) meV, $\Gamma_{(0.53\ 0\ l)}$ (5 K) = (0.43 ± 0.03) meV.

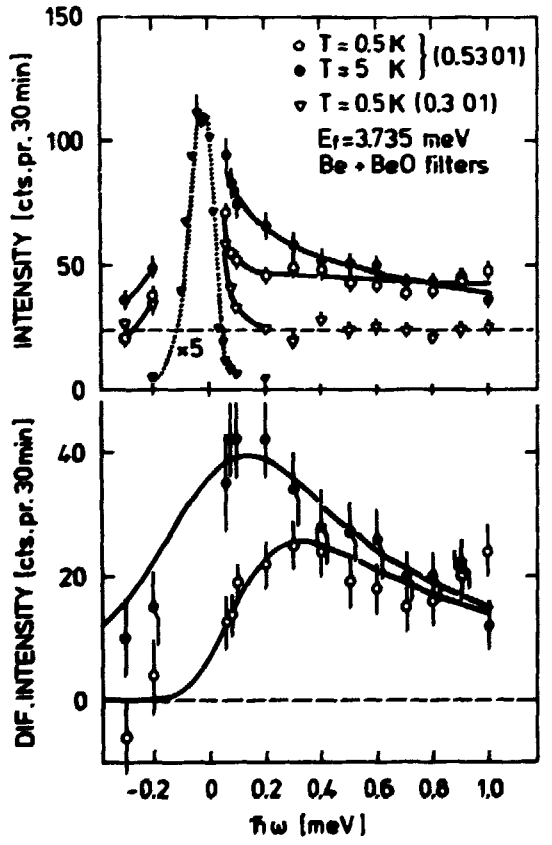

tribution to the count rate at this momentum transfer (compare Figure 2.2) and we may use this scan as a measure of the q-independent nuclear incoherent scattering which builds up below 0.15 meV. Contamination of the antiferromagnetic-zone-center energy scan from elastic magnetic Bragg scattering at (½01), to be discussed in 2.2.2, was avoided by displacing the momentum transfer to (0.53 0 1). The displacement is negligible as compared to the correlation length of the antiferromagnetic fluctuations, as may be seen from Figure 2.2.

Subtracting the data at q = (0.3 0 1) as the incoherent contribution below $\hbar\omega$ = 0.15 meV, and the fast neutron background of 48 counts/hour above $\hbar\omega$ = 0.15 meV from the data at q = (0.53 0 1), we can thus deduce the energy dependence of the magnetic part of the scattering at the antiferromagnetic zone center. This is shown in the bottom frame. Comparing this data to that of Figure 2.1 we thus find that the tighter energy resolution resolved a finite energy scale for the low energy magnetic fluctuations of $\hbar\omega \sim 0.3$ meV. We also note that the scattering decreases substantially between 5 K and 0.5 K. The decrease is essentially accounted for by the detailed balance factor $(1-e^{-\beta\hbar\omega})^{-1}$ which occurs as a factor to the imaginary part of the generalized susceptibility in the scattering cross section (see formula 1.1). The generalized susceptibility thus evolves very little between 5 K and 0.5 K. This will be further discussed in 2.2.3.

Since Bragg peaks strong enough to get an appreciable phonon intensity in this high resolution experiment cannot be reached we could not directly normalize these data so as to obtain an estimate of the staggered susceptibility. From the normalization of the coarser resolution data of Figure 2.1 to phonon scattering combined with the value of the relaxation energy determined from Figure 2.3 we can, however, determine $\mathrm{Re}\{\chi_{q=(½01)}(0)\} = (4\pm1)\cdot10^{-2}$ emu/mole-U.

2.2.2. Weak Antiferromagnetism With Finite Correlation Length

All our samples of nominally pure and superconducting UPt_3 had also elastic antiferromagnetic scattering at (½01) with typical widths in energy and momentum transfer only slightly larger than that of the nuclear Bragg peaks. This scattering developed rapidly below T_N = 5 K as will be discussed in 2.2.3. Furthermore, it decreased at larger momentum transfers similar to the uranium 5f formfactor observed in UO_2 [97], which leads us to conclude that the scattering is magnetic.

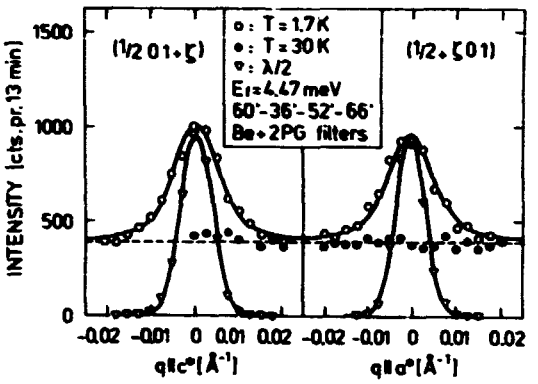

Figure 2.4. Elastic scans along the c and a* axis through the elastic antiferromagnetic peak at (½01) in pure UPt_3 at T = 1.7 K. The filled circles and dotted line indicate the incoherent elastic background measured at T = 30 K >> T_N = 5 K. The triangles are a measure of the instrumental resolution obtained by removing the filters, thus admitting nuclear Bragg scattering from (1 0 2).*

Figure 2.4 shows scans along crystallographic directions through the (½01) antiferromagnetic peak. The data was taken with configuration # 3 of Table 2.1. Similar peaks were found at symmetry related reciprocal lattice points and with integrated intensity ratios similar to those found in the antiferromagnetic thorium [47] and palladium [58] doped compounds.

The associated antiferromagnetic structure is shown in Figure 2.5.a. We can exclude domains of the type 2.5.b since no antiferromagnetic Bragg scattering was observed at (½00). (½01) and (½00) are symmetrically equivalent Bragg points, and only the polarization factor of magnetic neutron scattering [20] can thus explain that the scattering at (½00) vanishes. It vanishes because the scattering vector, $\varkappa$ is parallel to the antiferromagnetically ordered moment here, which shows that the ordered moment is parallel to the antiferromagnetic modulation of it (Figure 2.5.a).

The filled circles in Figure 2.4 are data taken at T = 30 K which shows that the antiferromagnetic scattering disappears upon heating, leaving the flat incoherent nuclear background. Also shown is the instrumental resolution as measured by removing the Be filter admitting scattering of second order neutrons from the (102) Bragg peak.

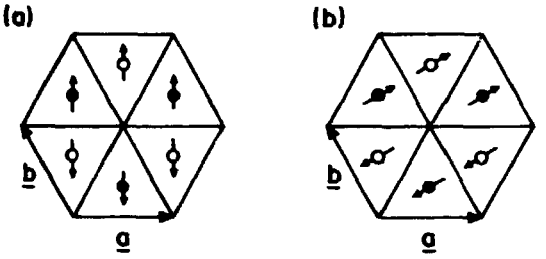

Figure 2.5. Schematic view of the hexagonal structure of UPt_3. ○ and ● denote uranium atoms in the basal plane, and displaced c/2 along the c axis. (a) shows the antiferromagnetically ordered structure of pure and doped UPt_3. (b) shows a related structure with the same isotropic bilinear Heisenberg exchange energy which is, however, not observed as magnetic order nor as short-range correlated magnetic fluctuations.

Only one single crystal was used in this experiment so as to be able to determine the correlation length associated with the antiferromagnetic order accurately. We immediately note that the antiferromagnetic scattering is slightly broader than the resolution in both crystallographic directions. Fitting the data to a Lorentzian, appropriately corrected for the finite instrumental resolution, yields inverse correlation lengths $\kappa_{c^*} = 3.2 \cdot 10^{-3}$ Å^{-1}, $\kappa_{a^*} = 3.8 \cdot 10^{-3}$ Å^{-1}.

Energy scans through this peak yielded widths below 100 μeV i.e. somewhat smaller than the incoherent scattering but not quite as small as observed in scans through nuclear Bragg peaks. The width in energy scans is however roughly consistent with finite spatial correlation length broadening the energy scan due to the correlation between energy and momentum resolution in a triple-axis spectrometer. We thus do not have evidence for a finite energy scale associated with this antiferromagnetic scattering.

The fact that the antiferromagnetic scattering is comparable in strength to the nuclear incoherent scattering shows that the ordered moment is indeed very small. We have normalized the antiferromagnetic scattering from our crystals originating from 4 different ingots. Table 2.2 summarizes the result. Within experimental accuracy all our nominally pure UPt_3 crystals had an antiferromagnetically ordered moment of $(0.02 \pm 0.005)\ \mu_B$.

We employed two different normalization procedures to access systematic errors:

Normalization to weak nuclear Bragg peaks not affected by extinction. The accuracy of this method depends on the knowledge of the structure factor associated with these, which is strongly dependent on the non-symmetry given positional parameter of the structure, and on the stochiometry of the sample. We attempted to reduce systematic errors by adding scattering and structure factors from several weak reflections.

Normalization to longitudinal acoustic phonon scattering on the other hand can be done close to strong nuclear Bragg peaks which measure the total scattering length of the unit cell. The accuracy of this method is limited by systematic errors in taking into account the different resolution effects on phonon scattering and Bragg scattering (see Appendix A).

As can be seen from Table 2.2 we obtained consistent results for the two methods which strengthens the belief in the absolute accuracy of the normalization procedures used.

Table 2.2. Comparison of weak antiferromagnetic order in single crystalline pure UPt_3 from 4 different ingots. The ordered moment has been normalized both to Bragg scattering from weak nuclear Bragg peaks and to phonon scattering from strong nuclear Bragg peaks. The column (001) indicates whether or not this forbidden Bragg peak was present due to defects.

Crystal	Ingot	(001)	Date	E/meV	Measured	T_N/K	Normalised	T/K	μ/μ_B
A	1	No	Mar-87	5	(½01)	5	(101) Bragg	1.8	0.02±0.01
B	2	No	Feb-87	4.47	(½01)	5	(101) Bragg	1.7	0.04±0.01
B	2	No	Feb-87	13.7	(½01);(½02);($^3/_2$01)	5	(101) Bragg	1.8	0.02±0.01
C	2	Yes	Jan-87	13.7	(½02)	5	(102) Bragg	1.6	0.01±0.01
All	1-4	Yes	Aug-87	13.7	(½01)	5	(002) phonon	2.2	0.03±0.01

2.2.3. The Antiferromagnetic Phase Transition

Figure 2.6.a shows the temperature dependence of the intensity of the antiferromagnetic peak at (½01). The data was collected with configuration # 4 of Table 2.1. The temperature-independent count rate at high temperatures arises from incoherent nuclear scattering. There is a clear break in the intensity as the temperature decreases below T_N = 5 K very much reminiscent of a phase transition although, as described in 2.2.2, the correlation length associated with the antiferromagnetic order does not diverge even as $T \rightarrow 0$. The temperature dependence of the peak intensity is certainly unusual. It continues increasing linearly with decreasing temperature down to $T \sim T_N/10$. The evolution below the superconducting transition at T_c = 0.5 K ~ T_N /10 is described separately in 2.2.4.

From Figure 2.3 we found that the low energy quasielastic magnetic scattering at (½01) decreases markedly between 5 K and 0.5 K. We have followed this temperature dependence more closely in Figure 2.6.b. It shows the temperature dependence of the quasielastic antiferromagnetic zone center response at an energy transfer of 85 μeV. The data was taken with the same configuration as that used for the high resolution energy scans in Figure 2.3 (configuration # 2 of Table 2.1). The momentum transfer was displaced slightly from (½01) to avoid contamination from the elastic scattering which grows rapidly below 5 K. The broken line in this figure indicates the incoherent nuclear scattering which dominates the background at this low energy transfer. It was measured at (0.301) see Figure 2.3.

Figure 2.6. Temperature dependence of (a) the elastic peak intensity at (½01) and of (b) the quasielastic magnetic scattering at (0.52,0,0.99) with an energy transfer of $\hbar\omega$ = 85 μeV.

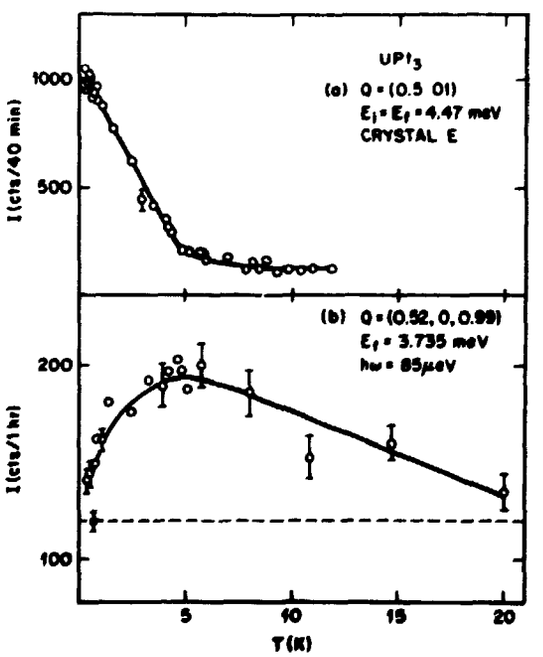

The scattering peaks at T_N = 5 K and decreases concomitantly with the increasing order parameter. Note however that, although one might associate this scattering with critical scattering, the decrease in intensity below T_N = 5 K is roughly accounted for by the detailed balance factor, which is proportional to T for $T > \hbar\omega/k_B$ ~ 1 K. This means that our data is consistent with a roughly temperature-independent generalized susceptibility below T_N = 5 K.

2.2.4. The Superconducting Phase Transition

We studied both the magnetic fluctuations and the elastic antiferromagnetic peak as a function of temperature through the superconducting transition at T_c = 0.5 K. The low energy magnetic fluctuation spectrum at antiferromagnetic zone centers is largely unaffected by the superconducting phase transition. Indeed in spite of intense efforts we have not been able to document any modification in the response at finite energy transfer down to about 0.1 meV at T_c.

The temperature dependence of the elastic antiferromagnetic peak, however, has an anomaly at T_c which is related to the onset of superconductivity. We measured the temperature dependence of the antiferromagnetic peak through T_c with an accuracy of a few %. The data was taken with configuration # 5 of Table 2.1. The possibility of applying a field was essential to identify anomalies at T_c as related to the superconducting transition. To pack the most possible of our cylindrical UPt_3 crystals into the center of a vertical field split coil magnet, the cylinder axis of the crystals was chosen vertical corresponding to scattering in the (*hk0*) plane. We studied the (1 ½ 0) reflection which is symmetrically equivalent to (½01), and has a similar cross-section. We obtained a count rate of antiferromagnetic elastic scattering of 80 counts/min on an incoherent nuclear background of 12 counts/min. To obtain the peak intensity to within a few % we thus

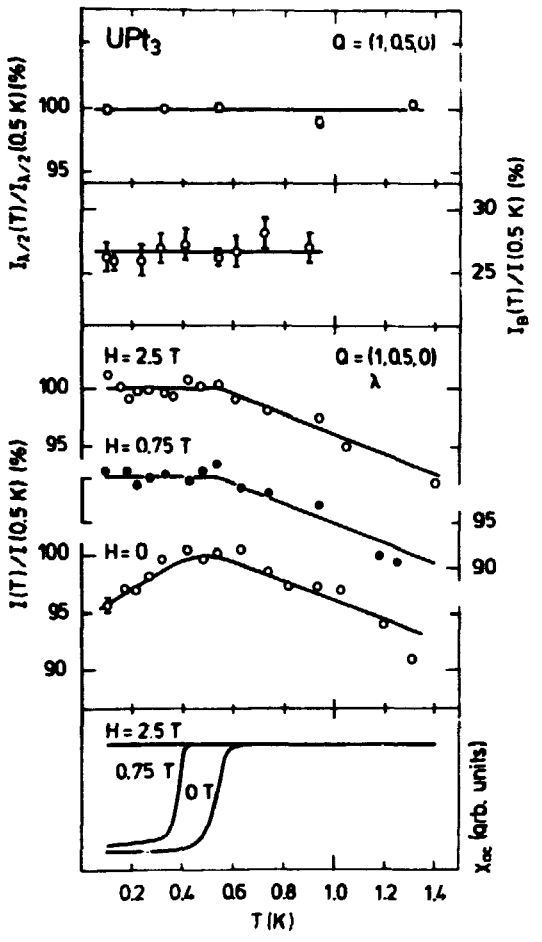

Figure 2.7. Measurements of the antiferromagnetic peak intensity of UPt_3 as a function of temperature and field around the superconducting phase transition. From top to bottom is shown:

Temperature (in) dependence of the λ/2 nuclear Bragg peak (210) and the nuclear incoherent background.

Temperature dependence of the antiferromagnetic Bragg peak through T_c at 3 different fields.

Temperature dependence of the AC susceptibility measured simultaneously at the same 3 fields.

typically counted for 5 hours at each temperature. Data in a field was obtained after cooling the sample through T_c in this field. The temperature scans were all done upon heating since this is quickest in a ^{3}He-^{4}He dilution cryostat. No hysteresis as a function of field or temperatures in the properties we studied were observed.

The temperature dependence of the (1½0) peak intensity through T_c in 3 different fields is shown in Figure 2.7. There is a maximum in the antiferromagnetic peak at T_c in zero field. Data previously published by us [82] are consistant with the present zero field data although the smaller dilution refrigerator used in that experiment did not allow us to reach temperatures low enough to discern the maximum clearly.

Data in a small applied field of 0.75 T is similar to that in a field of 2.5 T. It shows that the increase of the antiferromagnetic peak intensity ceases below T ~ 0.5 K, even when T_c is suppressed by the application of a field. The superconducting transition temperature in a field may be seen from the diamagnetic response in the AC susceptibility which was measured simultaneously at each field and is shown at the bottom of the figure. At the top of the figure is shown that the λ/2 scattering from the (210) nuclear Bragg peak, which was measured by removing the Be filters, is temperature independent. Also the incoherent nuclear background is shown to be temperature independent in this temperature regime. This proves that the changes in the intensity as a function of temperature at (1½0) indeed are due to variations in the antiferromagnetic scattering cross section. The second order nuclear scattering was however found to decrease about 5% when applying a field of 2.5 T. This is presumably because the large forces which the field exerted on the insert of our cryostat moved the sample slightly in the beam. For this reason we normalized our magnetic scattering data at different fields at $T = T_c$, although the intensity here only varied a few percent as a function of field.

As shown in 2.2.2 the correlation length associated with antiferromagnetic order is finite even at the lowest temparatures. It is therefore important to determine whether the decrease in the antiferromagnetic peak intensity below T_c is accompanied by a change in this correlation length. To investigate this we measured the ratio of elastic antiferromagnetic intensity in zero field above and below T_c at momentum transfers displaced from the (1½0) peak in the longitudinal direction. The data was taken with tight collimation after the sample (configuration # 6 of Table 2.1) to resolve the finite correlation length, and thus be sensitive to changes in it.

Figure 2.8 shows the result of this investigation. The resolution of the spectrometer was determined by removing the Be filters and thus measuring the nuclear λ/2 scattering from the (210) nuclear Bragg peak. This data is shown with filled circles. The open circles show the antiferromagnetic scattering which is clearly not resolution limited. The peak is even somewhat broader than those of Figure 2.4. This is due to the larger

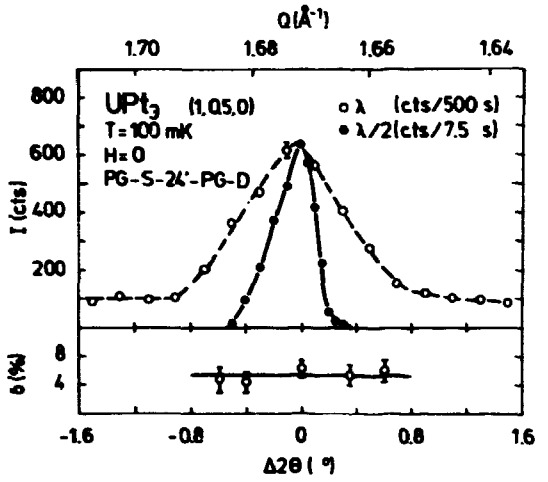

Figure 2.8. Top frame: θ-2θ scan through the antiferromagnetic Bragg peak at (1 ½ 0). The instrumental resolution as measured by second order nuclear Bragg scattering is also shown.

Bottom frame: The relative decrease in intensity at selected points of this scan between: T = 0.5 K and T ~ 0.1 K.

effective mosaic associated with the 4 approximately aligned single crystals used in the present experiment.

The ratio of background corrected antiferromagnetic scattering above and below T_c in zero field at various points through the longitudinal scan is shown in the bottom frame. The data shows that the shape of the antiferromagnetic peak is modified much less than is the overall scale factor by the superconducting phase transition. Our data are consistent with the line shape of the elastic antiferromagnetic peak being the same above and below T_c.

2.3. Discussion

The magnetic fluctuations of UPt_3 are overdamped below T_N = 5 K to the lowest energies of about $\hbar\omega$ = 0.2 meV which have been probed (Figures 2.1-2.3). The energy scans at (1/2 0 l) of Figures 2.1 and 2.3 are perfectly described as arising from magnetic fluctuations with an associated generalized susceptibility of the form

$$\chi_q(\omega) = \frac{\chi_o \Gamma}{\Gamma_q - i\omega} \qquad (2.1)$$

This was also the case for single crystal neutron scattering data at energies of order 10 meV. The absence of resonances in the excitations of the spin degree of freedom associated with the uranium 5f electrons suggests that these are in fact a part of the conduction electron system. They are not, as in conventional rare earth magnetism, placed several eV below the fermi level, and essentially decoupled from the conduction electron system.

Nonetheless, RKKY type interactions between spin and orbital moment density localized at uranium sites clearly is responsible for the enhancement of this Stoner type response at high symmetry points in reciprocal space. A simple model taking this into account along with the overdamped nature of the magnetic fluctuation is discussed in 3.3.1. Such a model can account for the low energy magnetic fluctuations in UPt_3. In fact, the lines through the data of Figure 2.1 are the result of such a model calculation. However, it cannot in its simplest form account for the cross-over between the two different types of antiferromagnetic correlations of the spin fluctuations at high and low energies.

As is shown in Appendix C the entropy associated with a generalized susceptibility of the form (2.1) is large and gives rise to a linear term in the specific heat $\gamma \propto 1/\Gamma$ of similar magnitude to that observed in UPt_3 and other heavy fermion systems. In particular the strong q-dependence of the relaxation energy Γ_q around antiferromagnetic Bragg points gives rise to low temperature deviations from the simple linear electronic contribution to the specific heat as has been shown by several authors [98,99,100], and which is observed experimentally [52].

The itinerant nature of the quasiparticles giving rise to the enhanced heat capacity was recently demonstrated most clearly by the observation of the de-Haas van-Alpen effect from quasiparticles with large effective masses in UPt_3 [101] and $CeCu_6$ [102].

The proximity of UPt_3 to antiferromagnetism doubling the unit cell in the basal plane, is evident from the low-energy magnetic fluctuation of this compound, Figures 2.1-2.3. The staggered susceptibility corresponding to these fluctuations is $Re\{\chi_{q=(½\ 0\ l)}(0)\} = (4 \pm 1)\cdot 10^{-2}$ emu/mole-U, enhanced by a factor of five over the q = 0 bulk susceptibility. It seems that the addition of palladium and thorium impurities disturbs a delicate balance which prevents the development of a large ordered moment in pure UPt_3.

It is remarkable that the low-energy magnetic fluctuations are polarized along the direction in which the unit cell is doubled as is the very small ordered moment in the antiferromagnetic state. Figure 2.5 illustrates spin configurations corresponding to two different orientations of spins with respect to the modulation direction associated with them. The fact that, even in the short-range correlated antiferromagnetic fluctuations, only the longitudinal fluctuations occur at low energies, suggests that the short-range interactions between the spin densities of uranium atoms are strongly anisotropic. Isotropic bilinear RKKY interactions do not distinguish the two configurations of Figure 2.5. It is interesting to note that anisotropic two ion interactions resolve the frustration associated with the antiferromagnetic interaction between moments in the hexagonal basal plane.

The extreme sensitivity of the antiferromagnetic properties of UPt_3 to doping poses the question whether the weak antiferromagnetism with a finite correlation length in nominally pure UPt_3 is an intrinsic effect. As stated in 2.1 our samples are chemically clean to the level of 10 ppm. Their major deficiency is the occurrence of stacking faults in some of the ingots giving rise to Bragg scattering at the forbidden (001) reflection and rod-like nuclear scattering along the a* axis. Although they were grown by the same technique it is suggestive for an intrinsic effect that 4 ingots have similar antiferromagnetic properties as may be seen from Table 2.2. In particular, similar antiferromagnetic properties were found in crystals with different defect structures as monitored by the presence or absence of the forbidden (001) Bragg peak. We also note that the Néel temperature of our superconducting samples, $T_N = 5$ K, is higher than that of the most lightly doped $U(Pt_{1-x}\ Pd_x)_3$ compound with $x = 2\%$ for which bulk measurements yield clear signatures of a magnetic phase transition at 3.5 K, and no superconducting phase transition. These experimental facts suggest that antiferromagnetic order is intrinsic to UPt_3 but obviously cannot be conclusive.

Footnotes and comments in various publications [103] have claimed that there exist nominally pure UPt_3 crystals which do not order antiferromagnetically. Actual data disproving antiferromagnetic order has, however, to our knowledge not been published and we caution that it is indeed not trivial to observe such a weak ordered moment by neutron scattering.

The antiferromagnetic phase transition at $T_N = 5$ K is marked by anomalies in other bulk properties. As shown in Figure 2.6, the low-energy antiferromagnetic zone center response has a maximum at T_N which corresponds to the imaginary part of the generalized susceptibility roughly ceasing to evolve below this temperature. We certainly believe this inelastic scattering to be an intrinsic bulk property of pure UPt_3 since it corresponds to so large a fluctuating moment. We also mention that both $\partial\rho/\partial T$ and $\partial\rho/\partial H$ have maxima at $T_N = 5$ K [104]. The result that the generalized susceptibility ceases to evolve below T_N is consistent with no big anomalies occurring in the heat capacity at T_N [105]. There is only a vanishing entropy change related to the phase transition.

Whether or not the antiferromagnetic order is an intrinsic property, our results concerning the temperature dependence of the antiferromagnetic order through the superconducting phase transition directly show that magnetic and superconducting properties of UPt_3 are indeed closely related.

Recently, measurements of the flux dynamics in UPt_3 with a high Q torsional oscillator indicated the existence of several phases with distinct flux lattice dynamics in the H-T plane [87]. Our data on the temperature- and field-dependence of the antiferromagnetic peak intensity of Figure 2.7, and also preliminary field scans at constant temperature in the superconducting phase, suggest that the antiferromagnetic peak intensity has a monotonic dependence on field and temperature. Below $T_c = 0.5$ K there is a local minimum for $H, T \to 0$ and a plateau for $H \gtrsim 0.75$ T, $T < 0.5$ K. The E-phase of reference [87] thus roughly coincides with the region of H, T space in which the antiferromagnetically ordered moment is reduced by about 5%. The low count rate associated with the antiferromagnetic scattering does however not permit us to identify phase boundaries clearly.

Two qualitatively different explanations of the different phases observed in the flux dynamics of the superconducting state were given in Reference [87]. They could be due to structural phase transitions in a flux lattice of anisotropic flux lines driven by the field dependent flux line density. They could however also involve a change in the microscopic nature of the superconducting state. In the former case we would expect the antiferromagnetic order parameter only to depend on the flux line density and not

on the detailed structure of the flux lattice. Our data in which the antiferromagnetic intensity at the lowest temperatures only evolves below 0.75 $T < H_{c2}$ clearly is not a simple function of the flux line density. We have two possible interpretations of our observations.

The applied field causes a transition between superconducting states with distinct microscopic properties which influence the antiferromagnetic order differently. These phases are then presumably related to those observed in Reference [87].

The field dependence observed could however also be related to the finite correlation length of the antiferromagnetic order. Assuming a triangular flux lattice the field at which the flux line separation equals the correlation length of the antiferromagnetic order is H = 0.5 T. Close to the field above which the antiferromagnetic intensity ceases to evolve at the lowest temperatures. The fact that the correlation length, as shown in Figure 2.8, does not evolve in the superconducting phase then suggests that this length scale is given by static disorder.

Further inelastic neutron scattering experiments studying the low energy magnetic fluctuations as a function of field and temperature in the superconducting state are hoped to clarify the documented relation between antiferromagnetism and superconductivity in UPt_3.

2.4. Summary

We have shown that pure UPt_3 has a strongly enhanced low-energy response at reciprocal lattice points corresponding to the antiferromagnetic order which is realized in lightly doped $U_{1-x}Th_xPt_3$ and $U(Pt_{1-x}Pd_x)_3$ compounds. The low-energy response is enhanced at different reciprocal lattice points than is that at energy transfers of order 10 meV but has a similar relaxational nature. It is polarized along the modulation direction which suggests that strongly anisotropic RKKY interactions are important.

All our chemically pure UPt_3 single crystals developed antiferromagnetic order below $T_N = 5$ K with an ordered moment of $(0.02 \pm 0.005)\mu_B$ and a roughly isotropic correlation length of 300 Å. The antiferromagnetic order is similar to that observed in doped compounds although $T_N = 5$ K is higher than that of the most lightly doped compounds. The ordered moment has an anomolous mean-field-like temperature dependence down to $T_N/10$. T_N is marked by a maximum in the quasielastic antiferromagnetic-zone-center neutron scattering below k_BT_N, and also by resistivity measurements. This suggest that, although the small ordered moment may not be an intrinsic property of UPt_3, it is a signature of a change in the electronic properties of UPt_3 at $T_N = 5$ K.

Our measurements of the antiferromagnetic order of nominally pure UPt_3 in the superconducting state provide proof of a close relation between antiferromagnetic and superconducting properties in UPt_3. They suggest that the application of a field in the superconducting state creates a transition between distinct superconducting states with different influence on the weak antiferromagnetic order.

3. Magnetic Fluctuations in a Heavy Fermion Antiferromagnet, U_2Zn_{17}

Large competing interactions are what characterize heavy Fermion antiferromagnetism. The heavy fermion antiferromagnets typically remain paramagnetic down to below 10% of the Curie-Weiss temperature (see Table 1.1) deviating from linearity of χ^{-1} versus T at temperatures around Θ_{cw} [34,106]. The ordered state is characterized by large bulk susceptibilities, showing that most of the unpaired spin density continues fluctuating in the antiferromagnetically ordered state. Neutron scattering is the ideal tool to elucidate the nature of the magnetic fluctuations which despite strong correlation only condense partially and at low temperatures, into long range static order.

This chapter describes such a neutron scattering study of the heavy Fermion antiferromagnet U_2Zn_{17}. The uranium intermetallic U_2Zn_{17} and its rhombohedral R3m structure has been known since the late fifties [107, 108,109]. Misiuk et al. [110] discovered that the susceptibility of the compound is of the Curie-Weiss form, with $\mu_{eff} \sim 3\mu_B$ and $\Theta_{CW} \sim$ -200 K, but it was Ott et al. [48] who discovered the antiferromagnetic phase transition at T_N = 9.7 K, the large electronic linear contribution to the heat capacity (γ = 540 mJ/mole-U K^2) and the anomalous low-temperature resistivity maximum at about 20 K, and thus put the compound into the context of heavy Fermion systems. The antiferromagnetic nature of the phase transition was subsequently confirmed, and its associated magnetic structure determined by neutron powder diffraction [111]. Polarized and unpolarized neutron scattering from polycrystalline material [112,113] has shown the existence of inelastic magnetic scattering with a formfactor similar to that of insulating UO_2 [97]. The associated state-density peaks at 10 meV $>> k_BT_N$ and is hardly affected by the phase transition. Magnetotransport measurements, however, have shown that the phase transition is marked by large anomalies in the hall coefficient and magnetoresistance [114].

We have performed single-crystal elastic, inelastic, polarized and unpolarized neutron scattering to elucidate the magnetic order and fluctuations in U_2Zn_{17}. Some of our work has previously been published [115].

The remainder of this chapter is organized as follows. After describing the experimental conditions we present the experimental results along with the first unbiased steps of analysis. Then we discuss the results and finally summarize and conclude.

3.1. Sample and Experimental Technique

Our U_2Zn_{17} single crystals were found in melts produced at 1050°C from the appropriate amounts of uranium and zinc. The measurements were performed in the (h01) plane of the rhombohedral (space group R3m [109]) crystal. We use hexagonal indices, with $a^* = 4\pi / \sqrt{3}a = 0.811$ Å^{-1} and $c^*2\pi/c = 0.479$ Å^{-1}, to label points in reciprocal space.

Table 3.1. List of spectrometers and configurations which were used for experiments on U_2Zn_{17}

Config #	Reactor	Instrument	E_f/meV	Collimation	Monoch	Analyzer	Filter	ΔE [meV]
1	Risø-DR 3	TAS 1	5	60'-33'-62'-67'	PG(002)	PG(002)	Be	0.2
2	Risø-DR 3	TAS 3	14.56	60'-40'-60'	PG(002)	÷	PG	÷
3	ILL	IN20	13.7	40'-60'-60'-60'	Heussler	Heussler	PG	1.0
4	Risø-DR 3	TAS 6	7.5	60'-36'-52'-104'	PG(002)	PG(002)	÷	0.4
5	BNL-HFBR	H 7	14.8	40'-40'-80'-80'	PG(002)	PG(002)	PG	1.5
6	BNL-HFBR	H 7	30	40'-40'-80'-80'	PG(002)	PG(002)	PG	4
7	Risø-DR 3	TAS 1	5	60'-33'-62'	PG(002)	÷	Be	÷
8	Risø-DR 3	TAS 1	5	60'-15'-28'	PG(002)	÷	Be	÷

Our samples display macroscopic sixfold symmetry, which implies that they consist of perfectly aligned twins related to each other by reflection through the (001) plane. A small single crystal ($2\times2\times2mm^3$) which we used in structural studies [116] furthermore had broad peaks corresponding to a hexagonal modification with $c_{hex} = \frac{2}{3} c_{Rhom}$. This structure is related to the rhombohedral structure by a different stacking sequence along the c axis [108]. This was however not the case for the big crystal ($5\times7\times8$ mm^3) which we used in inelastic scattering experiments.

The neutron scattering experiments were predominantly performed at cold-source three-axis spectrometers at Risø National Laboratory, but a polarized thermal neutron scattering experiment was carried out at IN20, Institut Max von Laue-Paul Langevin, Grenoble, France, and a thermal neutron scattering experiment was done at Brookhaven National Laboratory, Upton, New York. Standard triple-axis techniques [20,73] were employed, the details of which are listed in table 3.1. We shall refer to this table and explain our reasons for the choice of each configuration when describing our experimental results in the following chapter.

3.2. Experimental Results

The presentation of our experimental results is organized as follows. The first 3 chapters are devoted to low temperature (T ~ 2 K 9.7 K) properties, discussing the antiferromagnetic order, its associated magnetic fluctuations and their polarization. Then follow elastic and inelastic data which characterize the antiferromagnetic phase transition.

3.2.1. The Antiferromagnetic Order

The antiferromagnetic state is characterized by antiferromagnetic Bragg scattering at reciprocal lattice points in the (h0l) plane of the type (3p 0 3q) ± (101) and (3p 0 3q) ± (101) where p and q are integers [111]. The two sets of reflections with magnetic modulation vectors (i01) and (101) correspond to magnetic scattering from each of the two twins of the rhombohedral structure. The antiferromagnetic scattering from a given twin occurs at forbidden Bragg points of that twin which are however allowed Bragg points of its twin. The scattering from each twin was found to have equal strength for both the magnetic and nuclear scattering, indicating that the twins are of equal size.

The antiferromagnetic scattering was resolution limited. A typical rocking curve through the (102) reflection measured with configuration # 1 of Table [3.1] had a full width at half maximum of 0.007 Å^{-1} for both the magnetic and nuclear scattering.

The magnetic and nuclear unit cells are identical. Figure 3.1 shows the corresponding colinear structure. The structure corresponds to the spin densities of the two uranium atoms in a unit cell being opposed to each other. The magnetic structure factor of this structure assumes the same value for all allowed antiferromagnetic reflections, and the structure is unique in the sense that the whole twin contributes equally to each antiferromagnetic peak.

To within an experimental accuracy of about 10°, the magnetic moments lie in the basal plane, since the magnetic scattering in this unpolarized neutron scattering experiment was found to be roughly proportional to $P = \frac{1}{2}(1 + \sin^2\alpha)$, where α is the angle between the scattering vector $\varkappa$ and the c* axis.

Figure 3.2 shows the integrated intensity of a number of antiferromagnetic reflections in the (h0l) plane divided by the planar polarization factor, P. Our small single crystal of $(2\times2\times2)mm^3$ was used in this experiment to avoid extinction and multiple scattering. The data were taken with spectrometer configuration # 2 of Table 3.1 which has a large acceptance angle for the scattered neutrons. This makes the Lorentz

Figure 3.1. Antiferromagnetic structure of U_2Zn_{17}. One of the 3 domains which are related to each other by 120° rotation of the ordered moment in the basal plane is shown. The two structural twins correspond to reflection in a normal plane to the c axis.

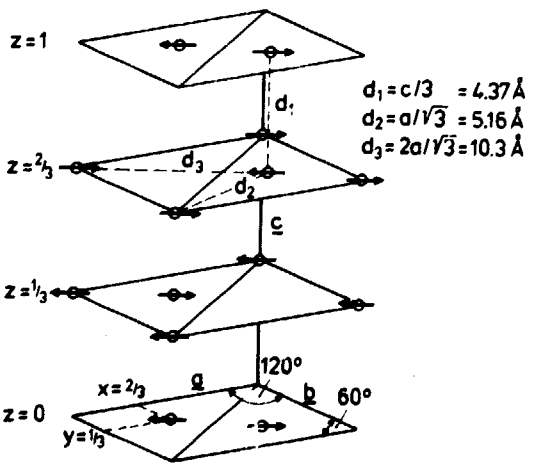

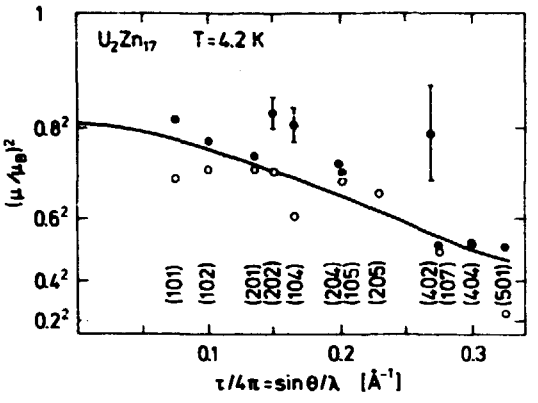

Figure 3.2. Form factor of the antiferromagnetically ordered moment in U_2Zn_{17} derived from ω integrated difference intensities in an unpolarized neutron scattering experiment. The filled and unfilled symbols correspond to data from each of the two structural twins.

factor 1/sin2θ, where 2θ is the scattering angle, a good approximation of the variation with 2θ of the sensitivity of the spectrometer to an ω scan through a Bragg peak. The data has thus been corrected by this factor and, furthermore normalized to the sum of 26 weak nuclear Bragg peaks. The structure factor sum was calculated on the basis of the positional parameters determined in a seperate structural study of the same crystal [116]. The structure factor sum is only weakly dependent on the positional parameters.

To within experimental accuracy the data lie on a smooth curve and thus confirm that the ordered structure indeed only has one non-zero value of the magnetic structure factor.

The steady decrease of the scattering at larger momentum transfer shows that the ordered moment has a finite spatial extent around the uranium atoms. The curve through the data is the squared formfactor measured for U^{4+} in UO_2 [97]. Since this curve roughly describes the observed variation of the antiferromagnetic scattering we conclude that the spatial extent of the spin density in the metallic magnet U_2Zn_{17} is similar to that in the insulator UO_2. The size of the ordered moment extrapolated to Q = 0 is (0.81 ± 0.05) μ_B in agreement with previous powder diffraction data [111].

Below T_N, in-plane anisotropies orient the ordered moment along the easy directions in the basal plane. Macroscopic three fold symmetry is obviously not broken at T_N. It is however broken microscopically in domains of the colinear antiferromagnetic order. By applying a field in the basal plane we can break macroscopic three fold symmetry and determine the moment orientation within the domains. This is most conveniently done in a polarized neutron scattering experiment.

We performed such an experiment at IN20 Institut Laue Langevin using configuration # 3 of Table 3.1. The measurements were done on our large single crystal in the (h0l) plane with a field applied in the vertical direction. This is a real space a direction. We measured the ratio of non-spin-flip and spin-flip magnetic Bragg peak intensity at (102) and (201) as a function of applied field. The nuclear scattering from the other twin at these reciprocal lattice points was subtracted by measuring difference intensities between T = 1.5 K T_N. The reflectivity of the magnetic and nuclear Bragg peaks are of the order 10^{-4} cm^{-1} at the wavelength of 2.4 Å used, so we may neglect secondary extinction [117]. We minimized the multiple scattering contribution to the two Bragg peaks in concern by choosing the neutron wavelength that gave the smallest peak intensities. The compensating vertical flipper current was optimized at each field and the flipping ratios as measured on the nuclear (003) peak were typically 20. The measured intensities were corrected for the finite flipping ratio. The result of the measurement is seen in Figure 3.3. Because field hysterisis can be expected in domain effects the crystal was cooled through T_N in each of the applied fields.

To interpret the data, note that in a vertical field the non-spin-flip scattering arises from spin components along the appied field, whereas spin flip scattering is from spin components within the scattering plane and perpendicular to the scattering vector. Table 3.2 expresses this quantitatively for the two reflections in question.

Figure 3.3 thus shows that the total amount of ordered moment along the applied field de-

Table 3.2. Contributions to the scattering in the non-spin flip and spin flip channels from spin components along various symmetry directions.

	(102)	(201)
non-spin flip	S_a^2	S_a^2
spin flip	$0.42\,S_c^2 + 0.58\,S_{a^*}^2$	$0.92\,S_c^2 + 0.08\,S_{a^*}^2$

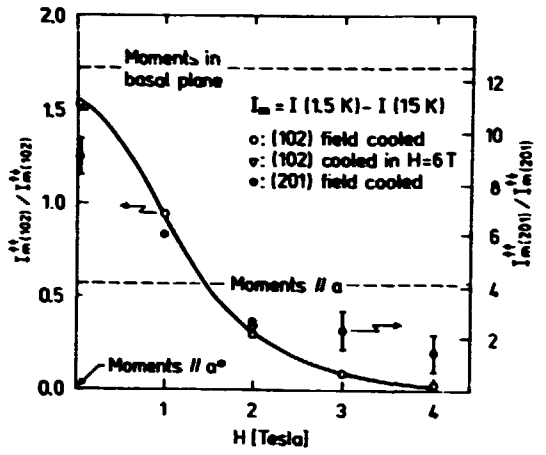

Figure 3.3. Flipping ratio of antiferromagnetic Bragg scattering in U_2Zn_{17} at two antiferromagnetic Bragg points as a function of the vertical field in which the sample was cooled through T_N. The sample was mounted in the (h0l) plane and the field was thus applied along an a-direction. The magnetic part of the intensity in each flipping channel was determined by subtracting the intensity measured at $T = 15\ K > T_N$ from that at $T = 1.5\ K$. The flipping ratios associated with various moment configurations in the basal plane are indicated in the figure.

creases as a function of the field. This is the behaviour expected for an antiferromagnet. As we shall see later the typical anisotropy energies within the basal plane are nearly 2 orders of magnitude larger than the energy associated with the applied field. We therefore interpret the decrease in the amount of ordered moment along the applied field as a domain effect in which the domains with the largest spin components along the applied field are disfavoured relative to those with larger components perpendicular to the field.

Because the nuclear scattering at (201) is nearly an order of magnitude larger than the magnetic scattering here, the procedure for determining the magnetic part of the scattering by subtracting intensities from below and above T_N is probably questionable for this reflection. In particular extinction release when lowering the microscopic symmetry can give a small temperature dependence even of the nuclear scattering. Nevertheless from the flipping ratio at (201) for H -> 0, where $S_a^2 = S_{a^*}^2$, and from Table 3.2, we get $S_a^2/S_c^2 \sim 40$ showing, in consistency with previous results, that within experimental accuracy the ordered moment lies in the basal plane.

On the figure are indicated the flipping ratios at (102) and (201) corresponding to macroscopic three fold symmetry, (i.e. the zero field state) and the high field state corresponding to antiferromagnetic moment orientation along the a and a* directions respectively. The flipping ratios measured at (102) are seen to be consistent with the high field state having moments along the a* direction perpendicular to the applied field. The fact that the magnetic flipping ratio at (201) does not become as small as would be expected is presumably due to a nuclear contribution to the temperature dependence of the non spin flip scattering as discussed earlier. In reference to our discussion of domain effects, we conjecture that the zero field state corresponds to an equal distribution of the three domain types with ordered moments along a*.

3.2.2. Magnetic Fluctuations in the Ordered State

The low temperature magnetic excitation spectra of U_2Zn_{17} are broad in energy, and extend to energies far beyond k_BT_N.

Figure 3.4 shows energy scans taken at the antiferromagnetic zone center (102) and at a high symmetry non-zone-center point (3/2 0 3/2) in the ordered phase. The scattering is magnetic as is shown later by our polarized neutron scatter-

Figure 3.4. Constant q scans at the antiferromagnetic zone center (102) (●) and at (3/2 0 3/2) (○), $T = 2$ K. The dashed line indicates the background measured for neutron energy gain. The full lines result from a model described in (3.3.1).

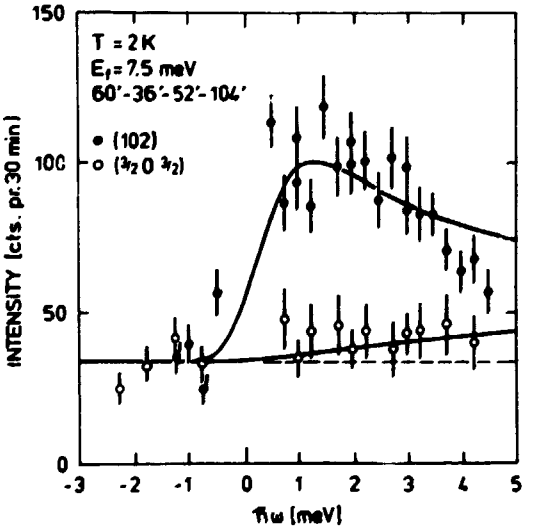

ing data (3.2.3). It is in fact also clear from the temperature dependence of the scattering at T_N that it arises from excitations of the spin and orbital moment of the unpaired 5f electrons (3.2.4).

Note that to within experimental accuracy there are no peaks in the scattering, which shows that the response function, surprisingly for a magnet in its ordered state, is non-divergent in the energy regime studied and in particular down to the limits of small momentum and energy transfer given by the resolution of the experimental setup; $\Delta E = 0.4$ meV $= k_B T_N/2$, $\Delta x = 0.10$ Å^{-1}. Both values are full-width at half-maximum. Δx is the resolution of momentum transfer perpendicular to the scattering plane which is the direction of coarsest momentum resolution.

As we shall see later, the integrated intensity of an energy scan such as that at (102) shown in Figure 3.4, is comparable to integrated intensities of resolution-limited spin waves in rare earth systems. So the intensity of inelastic magnetic scattering in an antiferromagnetic heavy Fermion system such as U_2Zn_{17} is the width of the spectrum over the energy resolution, i.e. typically more than an order of magnitude smaller than peak intensities of magnetic excitations known from rare earth magnetism. Furthermore, since the information on the spin dynamics of the heavy Fermion systems comprises peak widths and line shapes, heavy Fermion magnetism is a substantial experimental challenge for neutron scatterers and their instruments.

The data of Fig. 3.4 were for this reason taken with an unconventional experimental configuration namely configuration # 4 of Table 3.1. With this configuration we got reasonable count rates, while being able to follow the response to energies of the order $k_B T_N$. Since the neutron source was a H_2 moderator cooled to 25 K [118], we could neglect the flux of $\lambda/2$ neutrons reflected by the PG(002) monochromator in our inelastic experiments.

The magnetic scattering is clearly strongly enhanced at the antiferromagnetic zone center, (102) as compared to (3/2 0 3/2). Figure 3.5 illustrates this enhancement further. It shows constant energy scans at $\hbar\omega = 1$ meV and $\hbar\omega = 3$ meV through the antiferromagnetic zone center (102). The scans were taken along the (ζ 03-ζ) direction which is dominated by low-energy excitations from only one of the two twins, making the interpretation of the data somewhat simpler.

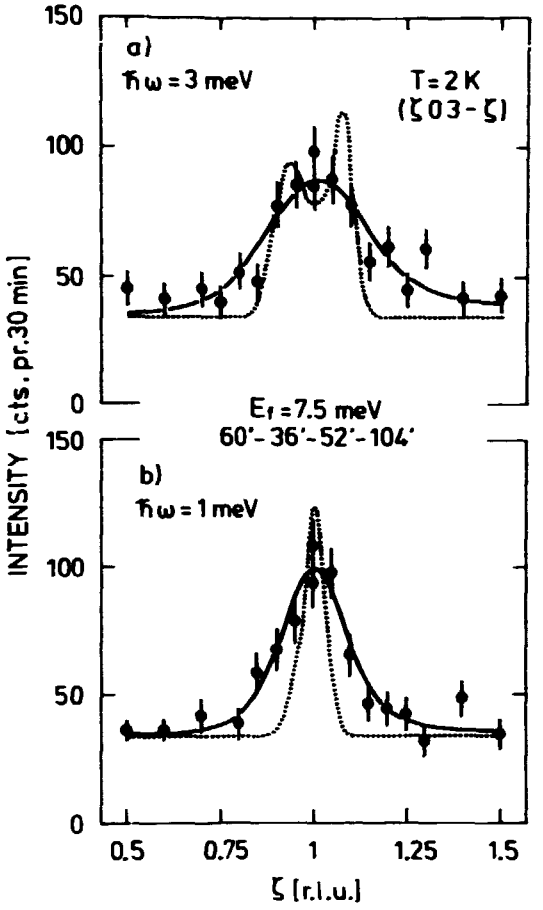

Figure 3.5. Constant energy scans through the antiferromagnetic zone center (102) at (a) $\hbar\omega = 3$ meV and (b) $\hbar\omega = 1$ meV. The data were taken at $T = 2$ K along the (ζ 03-ζ) direction. The broken line shows a resolution limited antiferromagnetic spin wave response with a velocity of 37 meV Å. The full line is the result of a model calculation described in 3.3.1.

Note first of all that the peak gets broader and weaker as the energy transfer is increased. The broken line is the intensity profiles which a conventional gapless linearly-dispersive antiferromagnetic spin-wave response would give rise to in the spectrometer configuration used for the present experiment. The spin wave velocity and the strength of such a response were fitted to give the best possible agreement with the data. This was obtained with a spin wave velocity of 37 meV Å. Clearly a resolution-limited spin wave response **cannot** account for the magnetic excitations in this region of energy and momentum transfers. The line which fits the data, better arises from a model calculation we will return to in 3.3.

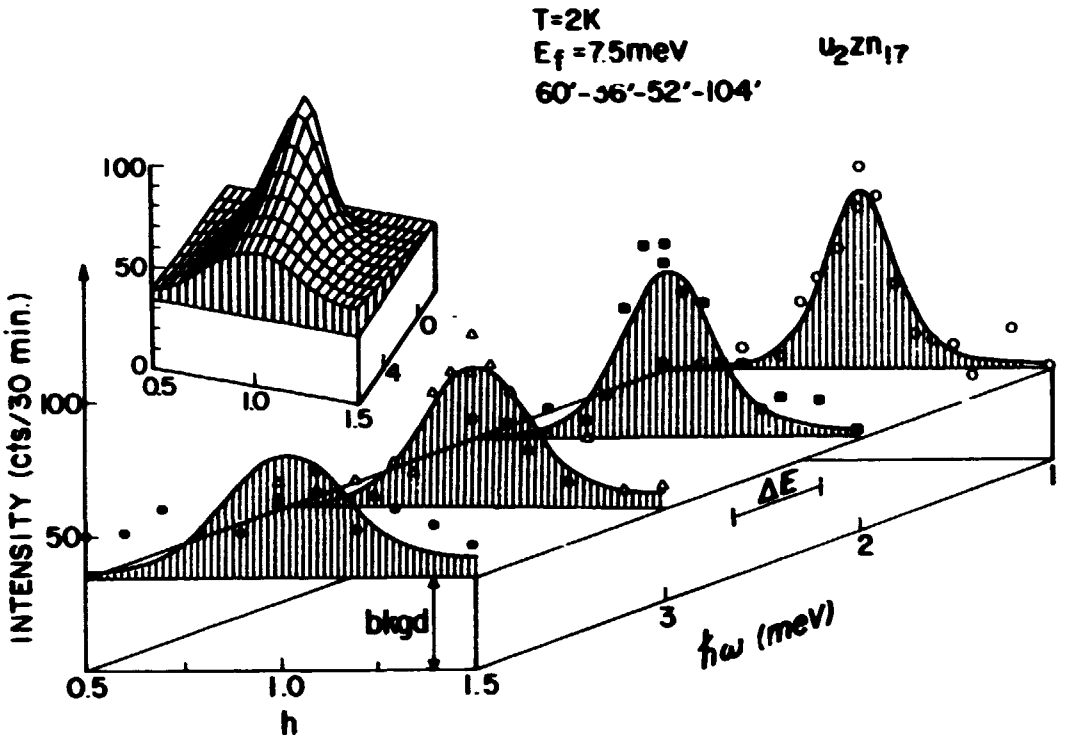

Figure 3.6. Constant energy scans along (h 03-h) in the ordered phase of U_2Zn_{17} at T = 2 K. The solid lines are the result of the three-parameter fit described in (3.3.1). Inset: The corresponding model scattering function in a perspective view.

Figure 3.6 summarizes the low-energy magnetic excitations in the ordered phase. It shows the scattered neutron intensity as a function of momentum and energy transfer in a 3d perspective. There is clearly appreciable scattering above background at $\hbar\omega$ = 4 meV. This part of the scattering was studied in a thermal neutron experiment at the triple axis spectrometer H7 of Brookhaven National Laboratory.

Figure 3.7 shows constant q-scans probing fluctuations with the same modulation as the ordered state, at (201) and probing the homogeneous magnetic fluctuations at (003). The data were taken with configuration # 5 of Table 3.1. The dashed line indicates the background as measured by turning the PG(002) analyzer crystal out of its reflection. There is some contribution to the scattered intensity by phonons, but since the momentum transfer is small and the resolution volume is large the scattering is dominated by diffuse magnetic scattering. This was confirmed, e.g. for the (003) scan, by the scattering at $\hbar\omega$ = 8 meV decreasing as a function of momentum transfer along c*, then remaining roughly constant between (003) and (006). Presumably multiphonon scattering becomes comparable to the magnetic scattering for larger momentum transfers.

Figure 3.7. Constant q scans at (201) and (003) in the ordered single domain state of U_2Zn_{17} at T = 2 K and H_v = 2 T. The broken line is the background as measured with the analyzer turned away from reflection. The dotted line is the calculated contribution to the intensity from inelastic scattering of the λ/2 neutrons of the unfiltered incident beam down to E_f = 14.8 meV. The full lines are guides to the eye.

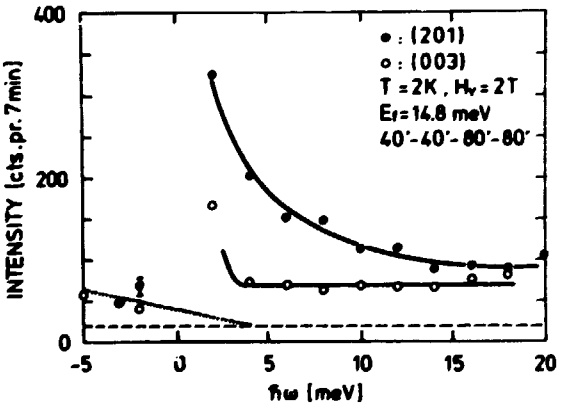

Due to the thermal population factor in the neutron scattering cross section neutron energy gain processes with energy transfers significantly larger than k_BT = 0.17 meV are not possible. The fact that the count rates on the neutron energy gain side are in fact well above the analyzer turned background is due to high-energy scattering of the $\lambda/2$ neutrons reflected by the monochromator. The dotted line is the calculated contribution to the intensity arising from such processes.

Another effect one should be aware of when studying this data is that the incident beam through the scan contains a varying amount of first and second order neutrons, which both contribute to the count rate of the incident beam fission monitor. At thermal sources using PG(002) monochromators, the correction factor varies from about 2 at an incident energy of 13 meV to close to 1 for incident energies above 30 meV [119]. Correcting the data of Figure 3.7 for this effect thus enhances the scattering below energy transfers of $\hbar\omega$ = 5 meV.

The data were taken at T = 2K and in a vertical field, H_v = 2T, which is enough to create essentially a single domain state as can be seen from Figure 3.3. By the procedure described in Appendix A we have normalized the data to acoustic phonons around the strong (006) nuclear reflection. Calculating the bulk susceptibility from the Kramers-Krönig relation (1.2), we obtain for the bulk susceptibility χ_{bulk} = 0.5 emu/mole-U in reasonable agreement with the value 0.75 emu/mole-U for the susceptibility found in bulk measurements on U_2Zn_{17} [49].

At the high energy end of these scans the features characteristic of the antiferromagnetically ordered state can no longer be discerned. To follow this incoherent high energy magnetic scattering we choose configuration # 6 of Table 3.1 whose energy resolution of about 4 meV is better suited in this energy regime. Figure 3.8 shows the extension of the energy scans probing antiferromagnetic and ferromagnetic fluctuations to 40 meV. Constant energy scans in the regions of momentum transfer studied were flat but increased sharply at momentum transfers of 6 × a* = 4.9 Å^{-1}. This shows that there is probably a significant contribution of multiphonon scattering in the energy scans of Figure 3.8. Nevertheless, the energy dependence of the scattering is dominated by magnetic scattering and the data thus gives a rough estimate of the fall off to high

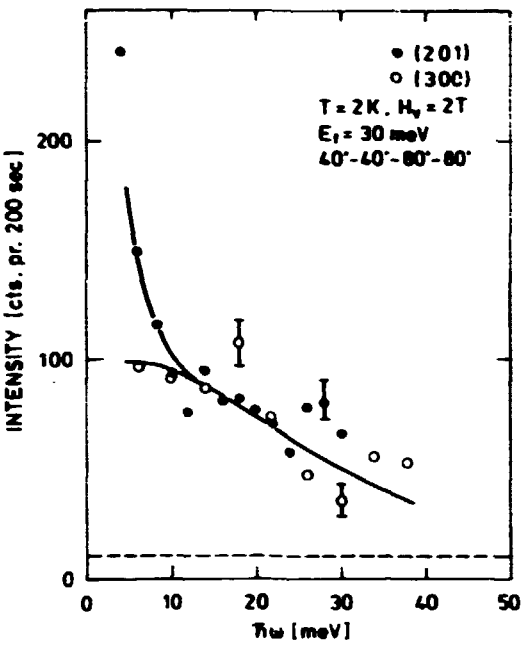

Figure 3.8. High energy scans at an antiferromagnetic zone center, (201), and at a zone boundary, (300), of U_2Zn_{17} in its single domain antiferromagnetically ordered state T = 2 K, H_v = 2 T. The broken line is the background as measured with the analyzer turned away from reflection. The full lines are guides to the eye.

energies of the fast uncorrelated magnetic fluctuations. Converting the energy scan at (300) to absolute units and calculating from the imaginary susceptibility the bulk susceptibility, yields χ_{bulk} = 0.6 emu/mole-U, close to the bulk susceptibility of 0.75 emu/mole-U.

3.2.3. Polarization of the spin fluctuations

The polarization of the magnetic excitations relative to the symmetry directions of the ordered state were studied in an inelastic polarized neutron scattering experiment [73] on the triple axis spectrometer IN20 at a thermal neutron beam at the institute Laue Langevin Grenoble, France.

Figure 3.9 shows constant energy scans at $\hbar\omega$ = 2 meV through the antiferromagnetic Bragg point (201). The data were taken with configuration # 3 of Table 3.1 at T ~ 2 K well below T_N. Spin flip and non-spin flip are measured relative to the neutron spin quantization axis defined by a small horizontal guide field oriented along the scattering vector throughout the scan. All magnetic scattering is therefore in the spin flip channel along with 2/3 of the nuclear spin incoherent scattering and the unpolarized background, whereas nuclear coherent, isotope incoherent and 1/3 of the nuclear spin incoherent scattering is in the non-spin flip channel [73]. The enhanced antiferromagnetic zone-center response occurs only in the spin flip channel which proves that it is indeed magnetic scattering.

Having shown this, we turn to the vertical field configuration in which the magnetic scattering is separated into the part polarized along the field, which scatters neutrons while conserving their spin, and the part polarized in the scattering plane which flips the neutron spin in the process of scattering. Figure 3.10 shows constant energy scans through the antiferromagnetic Bragg point (201) and (102) for both spin flip and non-spin flip scattering. The data was taken in the single domain state at T = 2K, H_v = 2T.

Figure 3.9. Polarization resolved constant energy scan at $\hbar\omega$ = 2 meV through (201) in a horizontal field.

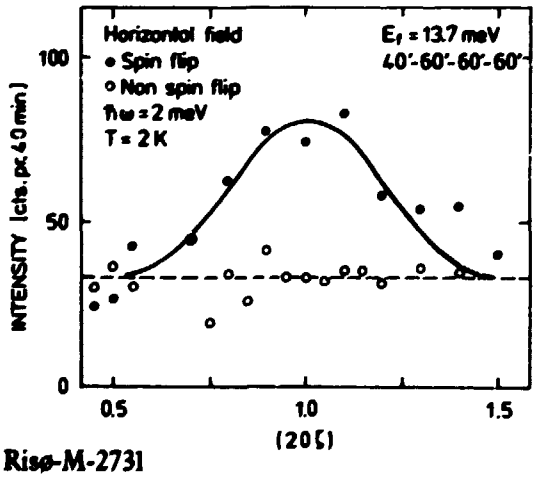

Note first of all that within the limits set by statistics and resolution the polarization resolved scans are similar to the unpolarized showing enhanced non-resonant low energy response at the antiferromagnetic zone centers. There is, however, a different amount of scattering in each channel. Table 3.3 shows the polarization components which contribute to the vertical-field spin flip and non-spin flip channels at various symmetrically equivalent antiferromagnetic Bragg points in the (h0l) plane:

As discussed in 3.2.1 the vertical field of 2T essentially selects a single domain with moment oriented along the a* direction. Referring to the hexagonal basal plane and the ordered moment along a* we may thus term χ''_{a^*}, χ''_{c^*} and χ''_a as longitudinal, out-of-plane transverse, and in-plane transverse susceptibilities, respectively. In other words, Table 3.3 shows that the non-spin flip channel measures transverse inplane magnetic excitations, while the spin flip channel measures a combination of longitudinal and transverse out-of-plane scattering. This combination depends on the orientation of the scattering vector x relative to a* and c*, such that the spin flip channel measures predominantly transverse out of plane scattering at (201) and longitudinal scattering at (105). Equal contributions of these two kinds occur in the spin flip channel at (102).

Returning to Figure 3.10 we conclude that the transverse inplane scattering is stronger than the transverse out-of-plane scattering at $\hbar\omega$ = 2 meV. As stated in Table 3.3 the magnetic non-spin-flip scattering is identical at (201) and (102),

Table 3.3. Magnetic form factor [10] and the contribution to spin flip and non-spin-flip scattering, in a field perpendicular to the a-c* plane, of each generalized susceptibility component. With χ''_v we mean the imaginary part of the generalized susceptibility along the direction* v. *Recall that* a* ⊥ a *and that* a *thus is parallel to the applied field.*

(hkl)	Q [Å^{-1}]	$\lvert F_m(Q)\rvert^2$	spin flip	non-spin flip
(102)	1.26	0.95	$0.58\,\chi''_{a^*}+0.42\,\chi''_{c^*}$	χ''_a
(201)	1.69	0.86	$0.08\,\chi''_{a^*}+0.92\,\chi''_{c^*}$	χ''_a
(105)	2.53	0.71	$0.90\,\chi''_{a^*}+0.10\,\chi''_{c^*}$	χ''_a

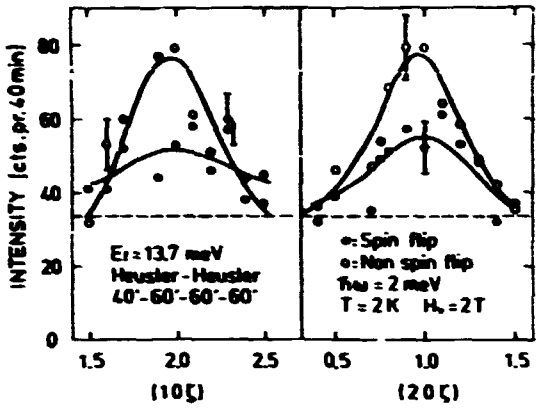

Figure 3.10. Polarization resolved constant energy scans through two antiferromagnetic zone centers of U_2Zn_{17} in its single domain antiferromagnetically ordered state at T = 2 K and in a vertical field of H_v = 2 T. The broken line is the horizontal field non-spin flip scattering, which is a measure of the non-magnetic background. The full lines are guides to the eye.

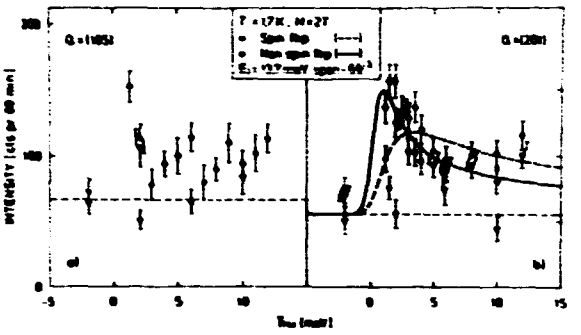

Figure 3.11. Vertical field polarization resolved constant q scans in the single domain antiferromagnetically ordered state of U_2Zn_{17}; T = 2 K, H_v = 2 T. The thin broken line is the analyzer turned background. The lines through the data at q = (201) are Lorentzian relaxation responses, appropriately corrected for background, finite energy resolution and the varying contribution of λ neutrons to the monitor count rate.

apart from the magnetic form factor which decreases by only 10% from (102) to (201). This similarity is reflected in the experiment.

Comparing the spin flip scattering at (201) and (102) the transverse out-of-plane scattering at (201) is clearly peaked at the antiferromagnetic zone center, but at (102), where it is 'diluted' by some longitudinal response. the resultant spin flip scattering is almost q independent. This suggests that the longitudinal scattering is much less q dependent at these energies.

The distinct nature of the longitudinal scattering is further elucidated by the data of Figure 3.11. It shows that the longitudinal spin flip scattering at (105) is not enhanced at the antiferromagnetic zone center at low energies but to within our experimental uncertainty is independent of energy below ħω = 15 meV. The enhanced antiferromagnetic zone center response is clearly only present in the transverse response which is dominating at (201). From the energy scan at (201) we furthermore conclude that the energy scale associated with out of plane transverse scattering (spin flip scattering at (201)) is significantly larger than that of the inplane transverse response.

Normalizing and integrating the spectra of Figure 3.11 is associated with some uncertainty because the background is comparable to the signal. We note, however, that the amount of moment participating in the two types of transverse response is similar, whereas the real part of the staggered susceptibility at (201) is about 30% larger for transverse inplane than the transverse out-of-plane component.

3.2.4. The Antiferromagnetic Phase Transition

Figure 3.12 shows the temperature dependence of the integrated intensity of the antiferromagnetic Bragg peak (102) through the antiferromagnetic phase transition at T_N = 9.7 K. The data was taken with a fixed energy of 5 meV in configuration # 7 of Table 3.1. There was no hysteresis at T_N and the curve resembles that of a mean field model with s = 1/2 except, as could be expected, for the critical region.

This was investigated further with configuration # 8 of Table 3.1 in which a good momentum resolution was obtained to distinguish the static long-range ordered component from critical fluctuations. The insert of Figure 3.9 shows the normalized intensity versus reduced temperature at temperatures close to T_N in a double logarithmic plot. From the slope we derive the critical exponent of the order parameter $\beta = 0.36 \pm 0.02$.

To establish the relation of the magnetic fluctuations reported in 3.2.2 to the antiferromagnetic phase transition, we followed the antiferromagnetic zone center scattering at energy transfers of order $k_B T_N$ as a function of temperature through T_N. This was measured with configuration # 4 of Table 3.1 and is shown in Figure 3.12.b. The data should be compared to the low

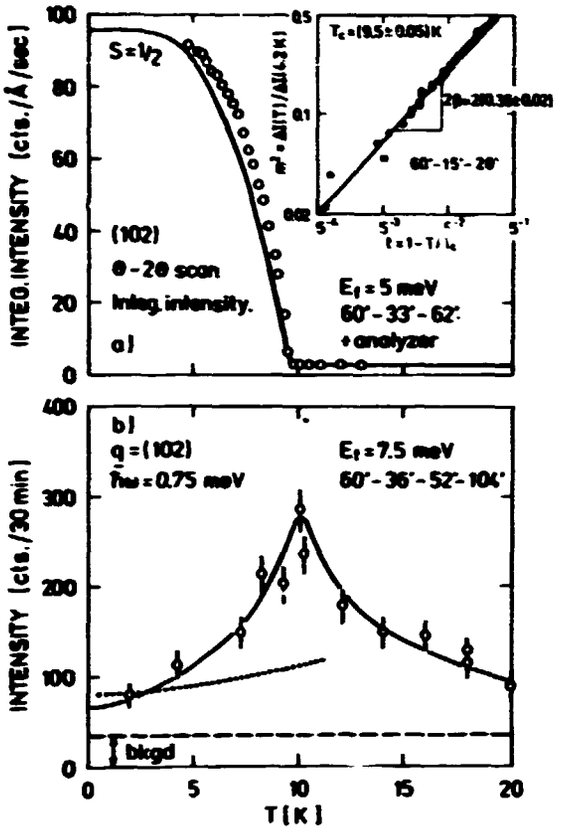

Figure 3.12. Elastic and inelastic data characterizing the antiferromagnetic phase transition at T_N = 9.7 K. The top frame shows the development of the order parameter at (102) compared to an s = 1/2 mean field calculation. The inset shows a double logarithmic plot of normalized squared magnetization versus normalized temperature in the critical region. The bottom frame shows the temperature dependence of the antiferromagnetic zone center, (102), quasielastic magnetic scattering at an energy transfer of ħω = 0.75 meV.

temperature magnetic excitation spectrum of Figures 3.4, 3.5 and 3.6 which was taken in the same configuration. The low-temperature, low-energy scattering is strongly enhanced at T_N and in particular much more than is accounted for by the thermal factor $(1-e^{-\beta\hbar\omega})^{-1}$ (indicated in the figure with a dotted line). This term enters the magnetic scattering cross section as a factor to the imaginary part of the generalized susceptibility (see formula (1.1)). The excitation spectrum is thus modified at these energies by the development of the order parameter as one would expect.

This development was followed in more detail by measuring the low-energy response, such as shown in Figures 3.4 and 3.5, at a selection of temperatures around T_N. Figure 3.13 shows a representative set of constant-E and constant-q scans at 3 different temperatures. The data show that the peak in Figure 3.12.b arises as the spectrum which is rather broad above and below T_N concentrates at low energies for T close to T_N. The correlation length of these antiferromagnetic fluctuations, which one may deduce from the constant energy scans, on the other hand continuously increases as the temperature is lowered.

Figure 3.13. Constant ħω = 2 meV and constant q = (102) scans at temperatures above and below T_N. The solid lines result from the model calculations described in 3.3.1.

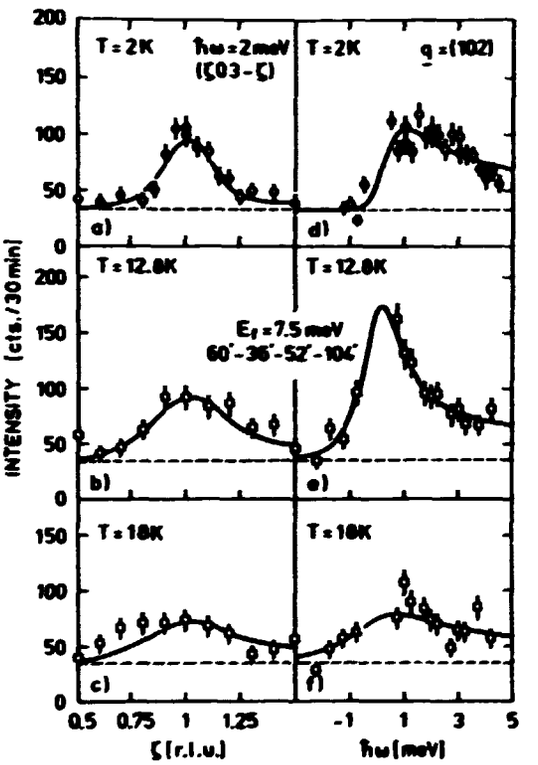

3.3. Analysis and Discussion

The most striking feature of the magnetic fluctuations in U_2Zn_{17} is the absence of propagating spin wave modes in the ordered state at energies of the order k_BT_N. Clearly the spin density which develops static long-range order below T_N is a part of the continuous conduction-electron state density since even low-energy dipolar excitations decay into the electron hole pair continuum.

From magnetic form-factor measurements of the ordered moment (Figure 3.2) and the magnetic fluctuations [112] it is, however, clear that the spin density is essentially localized about the uranium atoms as if it arises from atomic 5f electrons. It is important to keep this experimental fact in mind, but also to realize that obviously the (time averaged) spin density is largely unaffected by even qualitative changes in the dynamics of the electrons giving rise to it, essentially because it is not a phase-sensitive property. Inelastic magnetic neutron scattering is, however, sensitive to spatial and temporal phase coherence, and tells us that even low-energy and long-wavelength magnetic fluctuations have only short-range phase correlations.

In weak itinerant ferromagnetism it is generally found both experimentally [120] and theoretically [19] that there exists a low energy and long wavelength limit in which spin waves can propagate essentially without damping. This is, in its most fundamental explanation, because the ferromagnetic order parameter commutes with the Hamiltonian. Returning to the present level of abstraction, we can also say that in the itinerant ferromagnet up and down spin bands are shifted equally but in opposite directions by the exchange field, leaving a gap in which spin excitations have no continuous set of states to which they can decay, and thus they propagate with long-range coherence.

Antiferromagnetism on the other hand is a much more complicated ground state whose correct theoretical description has still not been found [121]. In particular since the staggered magnetization does not commute with the Hamiltonian, no true singularities occur in the magnetic response function of metallic antiferromagnets [21]. This can be stated in simpler terms in that the staggered exchange field does not necessarily produce a gap in the metallic spin flip excitation spectrum [21]. This situation should be contrasted to that of antiferromagnetism arising from nesting of the Fermi surface associated with several bands as in chromium. In this case well-defined spin waves with velocities of the order v_F the Fermi velocity, generally result [122].

Itinerant antiferromagnetic order in a metal can, but need not necessarily, produce a gap in the continuous electron hole pair excitation spectrum. From Figure 3.4 - 3.6 it would seem that this is indeed not the case for U_2Zn_{17}.

The ordered magnetic structure of U_2Zn_{17} is simple (see Figure 3.1) and is obtained when the spin density of each uranium atom prefers to be antiferromagnetically aligned to its nearest neighbour along the c axis, and its three nearest neighbours in the basal plane. This is in contrast to an itinerant antiferromagnet like chromium where the wave vector of the incommensurate spin density wave is determined by distances between specific parts of the Fermi surface.

The q-dependence of the magnetic fluctuations in U_2Zn_{17} is also strictly commensurate being enhanced at the antiferromagnetic zone centers (Figure 3.4). It seems then that short-range interactions dominate spin correlations in U_2Zn_{17}. Auerbach et al. [123] have found that these antiferromagnetic correlations can be described by the Anderson lattice model, and that 'three dimensionality and umklapp processes »hide« the effect of the Fermi vector'. One may also describe the antiferromagnetic correlations as due to short-range RKKY interactions. Although there are no simple 5f electrons, the localized nature of the spin density, which is found experimentally, justifies the concept of a conduction-electron mediated interaction between such neighbouring spin densities.

The energy spectrum of magnetic fluctuations, at least to within the accuracy to which it is measured, is simple and within scale factors similar at different momentum transfers. Quite simple functional forms can thus model the generalized susceptibility. We have written down such a model, which provides us with a convenient parameterization of our data.

3.3.1. Model of the Generalized Susceptibility of U_2Zn_{17}

Our model is stated within the RPA where the effect of interactions between entities with separate degrees of freedom on the susceptibility of the full system, $\chi_q(\omega)$, is given by

$$\chi_q^{-1}(\omega) = \chi_o^{-1}(\omega) - J_q \qquad (3.1)$$

$\chi_o(\omega)$ represents the frequency-dependent susceptibility of the spin and orbital moment-density associated with a single uranium atom, neglecting the interaction of this with neighbouring uranium sites. We neglect any q-dependence to this term and choose the form

$$\chi_o(\omega) = \frac{\chi_o \Gamma}{\Gamma - i\omega} \qquad (3.2)$$

which is a simple non-resonant response function with only one energy scale, Γ. It has been found to provide a good description of excitation spectra in Kondo and mixed valence systems [124] as well as in heavy fermion systems [125]. χ_o is the real part of the susceptibility and the energy scale $\hbar\Gamma$ is inversely proportional to the state density $n(\varepsilon_f)$ associated with the spin fluctuations described by (3.2) (see also Appendix C).

The intra-site interaction is represented by the fourier-transformed RKKY bilinear exchange constant J_q. Inserting (3.2) in (3.1) we obtain:

$$\chi_q(\omega) = \frac{\chi_o \Gamma}{\Gamma_q - i\omega} \qquad (3.3)$$

where

$$\Gamma_q = \Gamma(\Gamma - \chi_o J_q) \qquad (3.4)$$

as observed experimentally the spectral form of $\chi_q(\omega)$ is the same as that of $\chi_o(\omega)$, but the relaxation frequency now depends on J_q such that it becomes small whenever the modulation of the fluctuation is favoured by the exchange interaction. The model has an instability towards antiferromagnetic order with an associated modulation q_o when $\Gamma_{q_o} \rightarrow 0$ [126]. In the case of a non-Bravais lattice the algebra becomes somewhat more complicated since there are more than one atom in a unit cell. (3.1) thus becomes a matrix equation and generates both optical and acoustic modes (see Appendix B).

We have applied this model to the magnetic excitations in U_2Zn_{17}. We approximated the exchange interactions as ranging only to the 4 nearest neighbours (see Figure 3.1) and being identical for these, given by J_o'. We averaged contributions from each of the two twins of our crystal, although the low energy response was dominated by scattering from the one of the two twins to which the antiferromagnetic Bragg point we were near corresponded.

All our data at T = 2K were fitted simultaneously to the model by varying its three parameters χ_o, Γ and J_o'. The lines through the data of Figures 3.4 3.5 and 3.6 are calculated from such a fitted model function with the optimal set of parameters χ_o = 0.6 μ_B^2/meV, J_o' = 0.4 meV/μ_B^2 and Γ = 23 meV. Note that $\chi_o J_o'$ = 0.24 is determined directly by the fits whereas the absolute scale of each was determined from bulk susceptibility data. The model gives an excellent description of our data with a minimum of adjustable parameters. It is interesting that $\hbar\Gamma \sim k_B\Theta_{cw} >> k_BT_N$ whereas $\hbar\Gamma_{q_o} \sim k_BT_N$ which may be seen in the figures of 3.2.2.

The model, as fitted to the data, thus reveals the typical characteristics of a system with strong competing interactions. The single site relaxation rate, $\hbar\Gamma$ and the exchange coupling J_o are large competing energy scales that result in a significantly smaller energy scale $\hbar\Gamma_{q_o}$.

3.3.2. Temperature Dependence of Model Parameters

Encouraged by the good description of the low temperature data, which our model offered, we analyzed similar sets of data taken at temperatures varying from well above T_N (25K) and into the ordered phase, in an attempt to elucidate what is driving the phase transition. At each temperature we measured constant q scans at (102) and (3/2 0 3/2) and 3 constant energy scans at 1 meV, 2 meV and 3 meV. Typical data are shown in Figure 3.13.

We required our model to reproduce the temperature-dependence of the bulk susceptibility as measured in Reference [48]. This is related to the parameters of our model by

$$Re\{\chi_{q=o}(0)\} = \chi_o \cdot \frac{2}{1 + 4\chi_o |J_o'|} \qquad (3.5)$$

fixing a scale factor at T = 2K we thus reduced the number of temperature-dependent parameters to 2.

The result of this analysis is shown in Figure 3.14. The temperature dependence of χ_o, shown in the top frame, is essentially that of $\chi'_{q=0}(0) = \chi_{bulk}$ [48] since the denominator of (3.5) varies very little in the temperature range studied.

As shown in Appendix C we expect that $\Gamma \propto 1/\gamma$, where γ is the coefficient of the linear term in the specific heat. And indeed the increase of Γ at T_N by roughly a factor of 2.5 corresponds to the reduction of γ at T_N by a factor of 2.7 [48].

The most interesting result is that the RKKY exchange parameter J_o' in the whole temperature interval studied increases as T is decreased. Since χ_o remains constant from 15K to 10K, it actually seems as if it is the increasing effective RKKY coupling J_o' which drives Γ_{q_o} to zero at T_N making the system unstable towards antiferromagnetic order with a modulation given by q_o.

It is interesting to compare our results to recent theoretical work on the two impurity Kondo problem [30]. It is found that antiferromagnetic correlations between two RKKY coupled local moments persist even when these are fully screened by the conduction electron band in which they are embedded. This may be interpreted as the effective RKKY coupling scaling to larger values along with the energy scale associated with local moment screening.

Figure 3.14. Temperature dependence of the model parameters obtained from fits described in the text. Different symbols correspond to different experimental runs. Where no error bars are shown, the errors are comparable to, or smaller, than the symbols. The solid lines are guides to the eye.

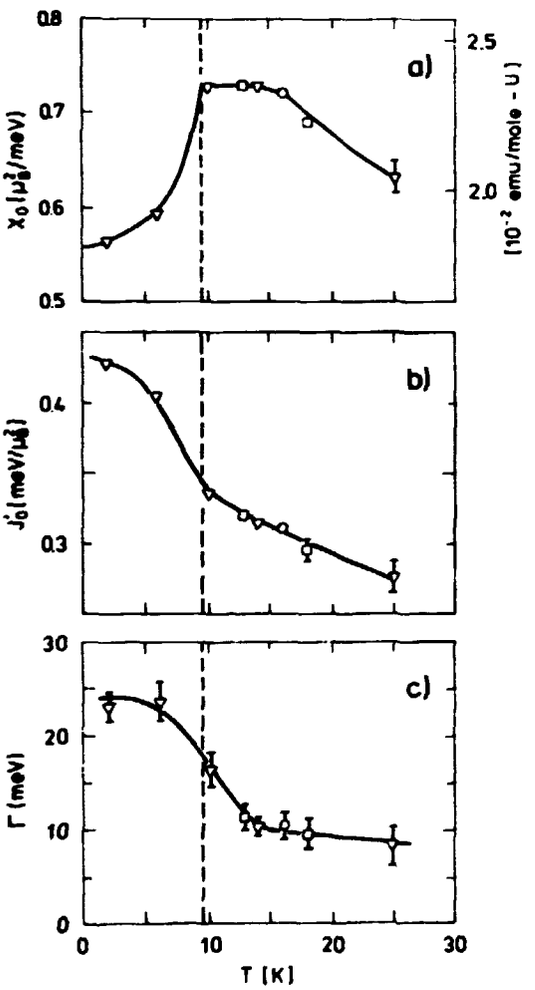

3.3.3. Polarization of the magnetic fluctuations

Although we believe that the above simple model contains many of the qualitative properties of magnetic fluctuations in heavy fermion systems, our polarized-neutron scattering experiment made it clear that in fact the dynamics is more complicated than previously anticipated.

First of all, in the light of the ordered moment being strongly reduced as compared to the fluctuating moment, it is surprising that transverse fluctuations dominate at low energies. This is in contrast to URu_2Si_2 (4.2.2) where the magnetic excitations below 30 meV are purely longitudinal. Figure 3.11 shows that the longitudinal response in the ordereed phase of U_2Zn_{17} is featureless below 15 meV. In this aspect the fluctuations are thus similar to those of Heisenberg antiferromagnets where the longitudinal response vanishes at T = 0K. The results suggest that the energy scale associated with the reduced moment is much larger than k_BT_N and the phase transition involves only this smaller effective moment.

From Figures 3.7 and 3.8 we find that indeed there is a significant amount of the magnetic fluctuations that are largely independent of q. Above 15 meV our single-crystalline energy scans show that the magnetic fluctuations are uncorrelated and that the spin density of the magnetic sites thus fluctuate independently.

Returning to the transverse response Figure 3.11b shows that what we were previously analyzing as arising from isotropic fluctuations is really composed of in-plane and out-of-plane components with different energy scales. Crystalline anisotropies previously largely neglected when discussing magnetic fluctuations of heavy fer-

mion systems, thus apparently are comparable in strength to the RKKY interactions in U_2Zn_{17}.

There are obvious extensions of our model which could take this planar anisotropy into account. The data which are presently available, however, do not allow for a meaningful introduction of more assumptions and parameters. We are in need of a more rigorous theory from a fundamental starting point.

3.3.4. Critical properties at T_N

The critical exponent of the order parameter $\beta = 0.36 \pm 0.02$ is close to the value expected for three-dimensional short-range coupled x-y magnets. This is consistent with our knowledge of the magnetic fluctuations of U_2Zn_{17}; the system has planar anisotropy with a characteristic energy for out-of-plane fluctuations of 3 meV $\sim 3\ k_BT_N$ (Figure 3.11.b). Furthermore, the magnetic structure arises from antiferromagnetic coupling between nearest neighbours as do the antiferromagnetic correlations of the magnetic fluctuations which have the same symmetry in reciprocal space. These observations are consistent with short-range interactions being dominating.

Our investigation of the temperature dependence of the magnetic fluctuations through T_N shows that as expected in a second-order transition the fluctuations are strongly enhanced at low energies close to q_o at T_N. It is interesting that the temperature scale over which this critical scattering evolves (Figure 3.12) is of order T_N. In the Heisenberg antiferromagnet critical scattering typically evolves within a fraction of T_N [127]. The extended range of criticality is typical for systems with competing interactions, which order at temperatures low compared to energy scales characterizing their dynamics. This is, for example, the case in singlet-ground-state systems where the critical temperature depends on the ratio of the exchange coupling to the crystal field splitting (see 4.3.2).

3.4. Summary

We have shown that the magnetic fluctuations of the heavy fermion antiferromagnet U_2Zn_{17} are coupled to the electron hole pair continuum at energies of order $T_N = 9.5$K.

In the ordered state the overdamped transverse response is enhanced in the neighbourhood of the commensurate antiferromagnetic zone center, q_o. There is a planar anisotropy with a characteristic energy for out-of-plane antiferromagnetic fluctuations of order 3 meV. The anisotropy does not give rise to resonances in the fluctuations.

The longitudinal response is not enhanced at q_o but featureless below 15 meV. Above 20 meV the magnetic fluctuations are independent of q and they extend to about 40 meV. The antiferromangetic phase transition proceeds as a conventional soft mode transition, but it is the temperature dependence of the RKKY exchange rather than that of the single-site dynamics which drives the system critical.

The temperature range over which the system is close to criticality is of order T_N, which along with the large energy range of spin fluctuations suggests that competing interactions are responsible for reducing T_N and μ_{ord} substantially as compared to Θ_{cw} and μ_{eff}. In the physical picture provided by the two impurity Kondo problem we think of this competition as being between the screening and the RKKY exchange which conduction electrons hybridized with a lattice of 5f electrons give rise to.

4. Weak Antiferromagnetism with Strong, Coexisting Propagating and Overdamped Excitations in URu_2Si_2

URu_2Si_2 constitutes an example of the cross-over between a low-energy regime of conserved local moments, and a high-energy regime of itinerant magnetic fluctuations, which lends itself to a detailed study by cold- and thermal-neutron scattering. This chapter describes such a study, which we find interesting because it provides information that helps us to understand heavy Fermion magnetism in the broader context of metallic magnetism.

URu_2Si_2 is usually called a heavy Fermion system although many of its bulk properties [55,128,129,130,131,132,133] are markedly different from most other heavy Fermion systems (Table 1.1). It has a large electronic heat capacity, which is approximately linear in T just above T_N = 17.5 K, and corresponds to γ = 180 mJ/mole K^2 [55]. A little further above T_N, at T ~ 30 K, there is, however, a maximum in the electronic specific heat [129], which is very much reminiscent of a Schottky anomaly, a signature of conserved local moments in an anisotropic environment, well known from rare earth magnetism [1,2].

Below T_N the heat capacity, apart from an exponential term which shows the presence of a gapped spectrum, has a linear term in the specific heat, γ ~ 50 mJ/mole K^2 [55]. This is certainly much larger than that of a normal metal, but nearly an order of magnitude smaller than electronic specific heat terms in other heavy Fermion antiferromagnets (see Table 1.1).

Also the bulk susceptibility of URu_2Si_2 [55,129,128] shows both features of crystal field magnetism, a Schottky anomaly at T ~ 50 K and large axial anisotropy, and features of heavy Fermion systems, a large value of χ as T -> 0.

The temperature dependence of the resistivity of URu_2Si_2 is qualitatively similar to other heavy Fermion systems, increasing below room temperature until a low temperature maximum, followed by a decrease by more than an order of magnitude [134,128,129]. The maximum in the resistivity, however, occurs at T ~ 70 K, higher in temperature by nearly an order of magnitude compared to other heavy Fermion systems, and furthermore the resistivity is strongly anisotropic, and largest in the normal plane to the easy magnetic axis.

The inelastic magnetic neutron scattering from a powder sample by Walter et al. [135] showed that the phase transition at T_N = 17.5 K was accompanied by the development of a gap in the magnetic excitation spectrum, another feature which distinguishes this compound from other heavy Fermion systems.

The main interest in URu_2Si_2 has, however, not so much been the magnetic properties as the fact that the compound, despite these, undergoes a phase transition to a strongly anisotropic superconducting state below T_c = 1 K [55,128,129]. It seems that the magnetic and superconducting properties are closely related in this compound [136,132].

We are primarily concerned with the magnetic properties of URu_2Si_2 in their own right. We present a complete exposition of our single crystalline elastic and inelastic neutron scattering data, parts of which have already been published [137]. Our investigations focus on the phase transition at T_N = 17.5 K and on the nature of the low-temperature magnetic fluctuations in URu_2Si_2.

The chapter is organized in 3 main parts: Sample and experimental technique, the obtained experimental results and finally analysis and discussion.

4.1. Sample and Experimental Technique

The measurements were performed on a 5 cm long cylindrical single crystal with a diameter of 0.5 cm, grown by a specially adopted Czochralski method [138]. The as-grown crystal was annealed for 7 days at 1000°C. URu_2Si_2 has the body-centered tetragonal $ThCr_2Si_2$ structure with lattice parameters a = 4.124 Å, c = 9.582 Å at 4.2 K. Our crystal had an a axis along the cylinder axis, and the measurements were performed with momentum transfers in the (*h0l*) and (*hk0*) planes.

Our crystal was found to have a substantial amount of stacking faults mainly along the tetragonal c* axis, giving rise to weak temperature-independent nuclear rod-like scattering along this axis. Similar effects, which may even be of interest in their own right [139], were found in another cylindrical single crystal grown along the c* axis.

The neutron-scattering experiments were performed at the cold-neutron source at the DR 3 reactor of Risø National Laboratory and at the thermal-neutron source at the NRU reactor of Chalk River Nuclear Laboratories.

We have employed standard triple-axis neutron scattering techniques, with choices of experimental configurations to suit our purposes. In general, the cold source experiments were performed varying the incident neutron energy with a vertically focussed PG(002) monochromator and using a PG or Be filter in the scattered beam to reduce the energy window of the detection system to the lowest order (002) reflection of a PG analyzer.

In the thermal beam experiments we used a flat Si(111) monochromator and a PG analyzer. In this configuration, since (222) is a forbidden reflection of silicon, there was a negligible flux of $\lambda/2$ neutrons after the monochromator. Also the $\lambda/3$ contents of the incident beam could be neglected due to the high energy cut-off of the thermal source. We could thus operate without a filter, or with a sapphire filter before the monochromator to reduce the fast neutron flux, which mainly creates background.

In Table 4.1 the details of each experimental configuration is summarized. We will refer to this table when necessary by the number in the first column.

4.2. Experimental Results

This chapter is a hopefully unbiased description of the actually obtained experimental results along with the parts of the data-analysis which may be done with a minimum of assumptions.

We describe the magnetic ground-state properties and the low-temperature excitations from it, the development of short range antiferromagnetic correlations in the high-energy overdamped response, and finally the antiferromagnetic phase transition at $T_N = 17.5$ K.

4.2.1. Antiferromagnetic order

Figure 4.1 shows elastic scans along the a* and c* directions through the forbidden nuclear (100) and (102) Bragg peaks. The data were taken with spectrometer configuration # 1 of Table 4.1. The main criteria for the choice were a good energy resolution and a minimal $\lambda/2$ contamination of the beam. The dashed line in Fig. 4.1.a,b indicates the nuclear incoherent background measured at T = 60 K, well above the phase transition at $T_N = 17.5$ K. As discussed more thoroughly in 4.2.5 the scattering develops rapidly at T_N. We have found similar scattering at reflections $(h0l)$, where $h+l = 2n+1, h = 0$. The scattering decreases at high momentum transfers. These observations are consistent with an approximately static and long range (although not infinite, see later) antiferromagnetic correlation of the c axis components of the magnetic moment density located at the uranium sites. The correlations are such that the moment density associated with each U site is opposed to its 4 U neighbours displaced above and below it along the c axis (see the inset of Figure 4.11).

Table 4.1. List of spectrometers and configurations which were used in experiments on URu_2Si_2.

Config. #	Reactor	Instrument	E_f/meV	Collimation	Monochromator	Analyzer	Filter	ΔE/meV
1	Risø-DR3	TAS 6	4.47	60'-49'-52'-66'	PG(002)	PG(002)	Be + PG	0.15
2	Risø-DR3	TAS 6	14.6	60'-36'-52'-66'	PG(002)	PG(002)	PG	1.0
3	AECL-NRU	N 5	12.4	40'-60'-60'-80'	Si(111)	PG(002)	+	1.0
4	AECL-NRU	N 5	21	40'-60'-60'-80'	Si(111)	PG(002)	+	1.9
5	Risø-DR3	TAS 7	4.47	20'-open-53'-60'	PG(002)	PG(002)	Be + Pg	0.19
6	Risø-DR3	TAS 7	5	20'-open-open-open	PG(002)	PG(002) focused	Be	0.26
7	Risø-DR3	TAS 7	5	20'-open-53'-60'	PG(002)	PG(002)	Be	0.19

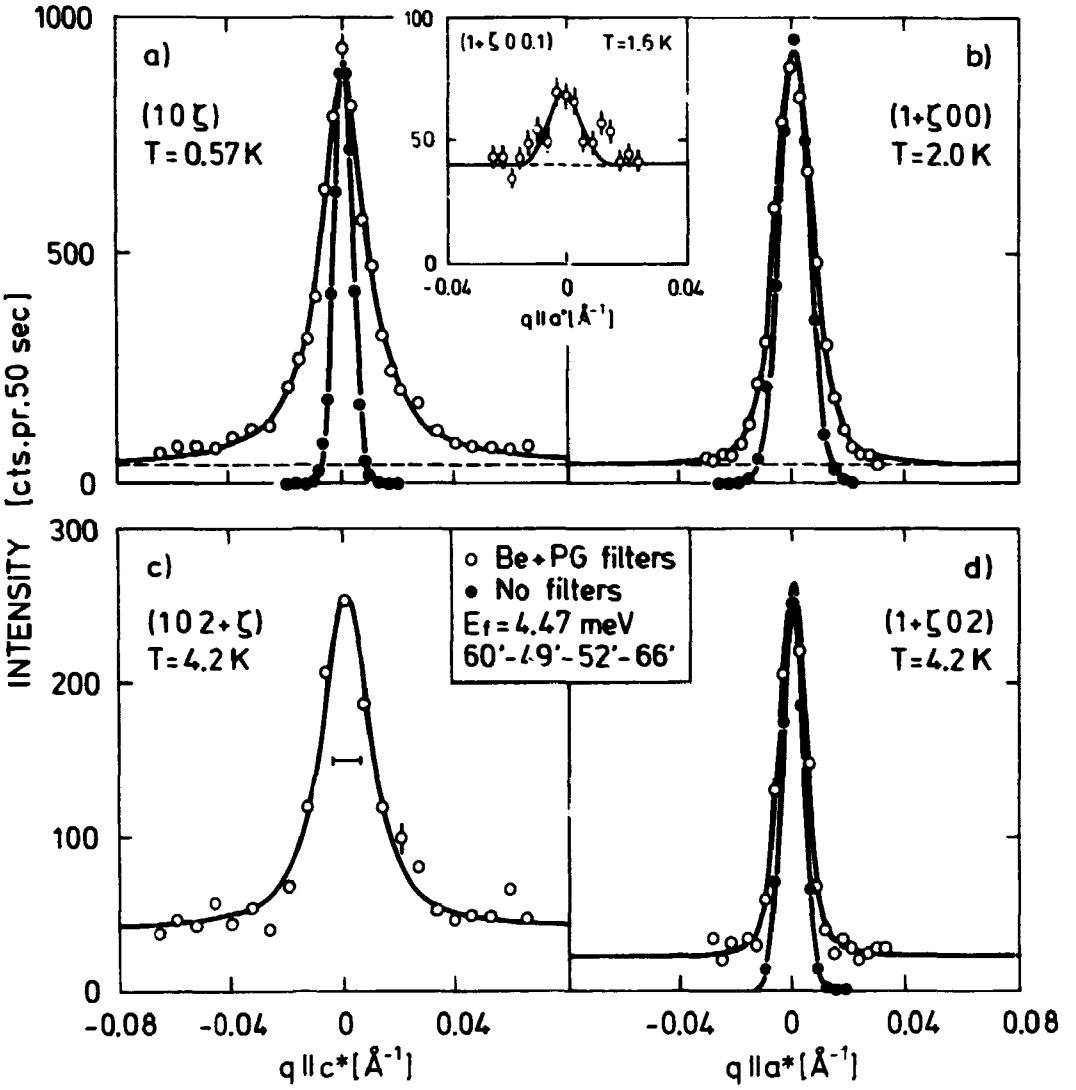

Figure 4.1. Elastic scans along the c and a* axis through the antiferromagnetic peaks at (100) and (102). The closed circles are taken without filters as a measure of the instrumental resolution. The top insert is a scan across the tails of scattering of (a).*

Figure 4.2 shows the integrated magnetic intensity of a selection of these antiferromagnetic peaks in the (*h0l*) plane, divided by their associated polarization factor. (The magnetic part of the scattering was found by subtracting the T = 30 K incoherent and higher order nuclear scattering from the low temperature data.) The polarization factor associated with spins polarized along the c axis is the squared basal-plane component of the unit vector parallel to the scattering vector. These data are a measure of the form factor, i.e. the squared fourier transformed of the magnetic moment density associated with the antiferromagnetic peaks. The form factor is found to decrease as a function of momentum transfer with a characteristic half width comparable to that found in UO_2 [97].

To characterize in more detail the nature of the antiferromagnetic correlations we return to Fig. 4.1. First of all we note that the scans are taken at various temperatures below 5 K. As we shall see later the evolution of this antiferromagnetic scattering has however essentially ceased at these temperatures which are all well below T_N = 17.5 K. We may thus regard the data of Fig. 4.1 as a measure of essentially ground-state properties.

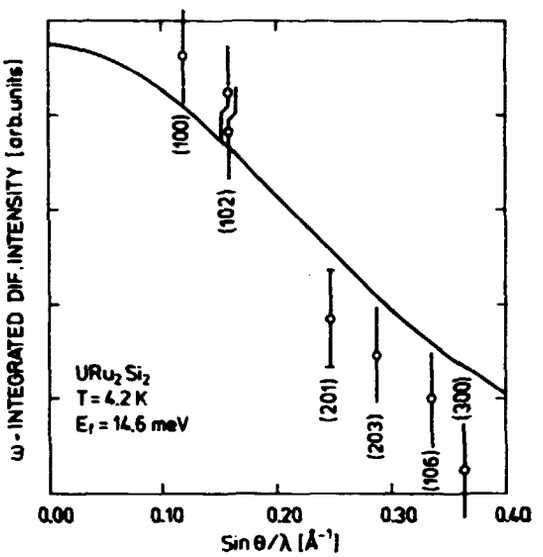

Figure 4.2. ω integrated difference of elastic scattering at T = 5 K and T = 30 K at forbidden nuclear reflections (h0l), h + l = 2n + 1, h = 0. The difference intensity has been divided by a c axis dipolar polarization factor as discussed in the text. θ is the half scattering angle and λ is the neutron wavelength.*

The resolution of the spectrometer for elastic scattering at (100) and (102) has been measured by performing similar scans with an unfiltered neutron beam containing a significant amount of λ/2 contamination. The scattering in these scans, also shown in Fig. 4.1, is resolution-limited Bragg scattering of λ/2 neutrons from the (200) and (204) nuclear reflection respectively. Comparing the line shapes observed with the filtered beam to these data we conclude that the antiferromagnetic peak is almost resolution limited in the basal plane, whereas the scans along the c* axis clearly have a non-gaussian line shape.

Caution is necessary when interpreting these experimental facts. The approximate symmetry of the spectrometer about a vertical plane containing the scattering vector in an elastic scattering process, implies that the principal axes of the resolution function in momentum space are parallel and perpendicular to the scattering vector. Furthermore, the momentum transfer perpendicular to the scattering vector is most strongly correlated with the energy transfer. This means that a low-energy isotropic response, due to the finite energy resolution, will appear broadened along the perpendicular direction to the scattering vector.

In Figure 4.1, we have, however, observed similar lineshape anisotropies around two different antiferromagnetic peaks namely (100) (a),(b), and (102) (c),(d). It is thus clear that the anisotropy is related to the crystalline directions and not to the transverse and longitudinal direction relative to the scattering vector.

The inset at the top of the figure further elucidates the rod-like nature of the scattering. It is a scan in the perpendicular direction, (1 + ξ00.1), across the tails of the peak in Fig. 4.1 (a). The solid line through the points has the resolution width. It is clear that the tails of the peak along c* have a rod-like character, remaining almost resolution-limited along in-plane directions.

To quantify correlation lengths and the size of the ordered moment, we assume an exponential decay of correlations along the c* axis:

$$\langle S^z_R S^z_{R+\tau} \rangle = \exp(-\kappa_z \tau_z)$$

The corresponding Fourier-transformed correlation function is [149].

$$\langle S^z_q S^z_{-q} \rangle = \langle S^z \rangle^2 \frac{\sinh(\kappa_z c)}{\cosh(\kappa_z c) - \cos q_z c}$$

To compare with the measured neutron intensities we folded the corresponding cross section with the measured experimental resolution. Furthermore, we added the independently measured flat nuclear incoherent background and a resolution-limited gaussian describing the weak λ/2 nuclear Bragg scattering. The lines through the data of Fig. 4.1 are the results of least squares fits of this model to the data. The correlation lengths deduced from scans around (100) and (102) are within the experimental accuracy identical; $\kappa_c(100) = (9.8 \pm 0.4) \cdot 10^{-3}$ Å^{-1} κ_c (102) = $(8 \pm 1) \cdot 10^{-3}$ Å^{-1}.

Applying the same formalism to the scan along the a* direction we deduce inverse correlation lengths of κ_a (100) = $(3.2 \pm 0.2) \cdot 10^{-3}$ Å^{-1}, κ_a (102) = $(1.7 \pm 0.3) \cdot 10^{-3}$ Å^{-1}. The correlation anisotropy is thus about a factor of 4. From looking at the data it is however clear that since the antiferromagnetic scattering along a* is just barely broader than the resolution widths, the determination of the inplanar correlation length is somewhat uncertain.

The size of the moment involved in these correlations was obtained by normalization of the magnetically scattered neutron intensity to the intensity associated with the known cross section of the nuclear (101) Bragg peak. The fact that $|(100)| \sim |(101)|$ allowed us to neglect the variation of the spectrometer-resolution function in this comparison. We found from Fig. (4.1).a

$$<S^z> = (0.04 \pm 0.01)\mu_B.$$

To access the energy scale associated with the antiferromagnetic scattering, we performed energy scans at various momentum transfers displaced along the c* axis from (102) at T = 4.2 K. All these scans had an energy width below 100μeV which is close to that of a Bragg peak. Any finite energy scale related to this antiferromagnetic scattering is thus more than an order of magnitude less than that of the zone center spin-wave gap (see 4.2.2).

4.2.2. Low Energy Propagating Excitations

Focusing now our attention on magnetic excitation in the energy range 1 - 10 meV these were studied with triple-axis neutron spectroscopy using configurations 2, 6 and 7 of Table 4.1. Configuration # 2, in which E_f = 14.6 meV, gave count rates of the order 50 cpm in the most intense magnetic excitations. To study lifetimes of the excitations the better energy resolution of configurations 6 and 7 were however needed reducing the typical count-rates by roughly a factor of 10.

Figure 4.3 shows typical constant Q scans at 6 different momentum transfers. First of all we note that, in contrast to the spin fluctuations of UPt_3 and U_2Zn_{17}, the present excitations are underdamped or resonant since, by inspection of Fig. 4.3, clearly $<\omega>^2/<\omega^2> << 1$. The peaks are in fact close to resolution limited.

Figure 4.3. Energy scans through low energy propagating magnetic excitations. The 3 scans to the left illustrate the formfactor of the response since the reciprocal lattice points are symmetrically equivalent. The scans to the right at 3 antiferromagnetic zone centers illustrate the axial polarization factor.

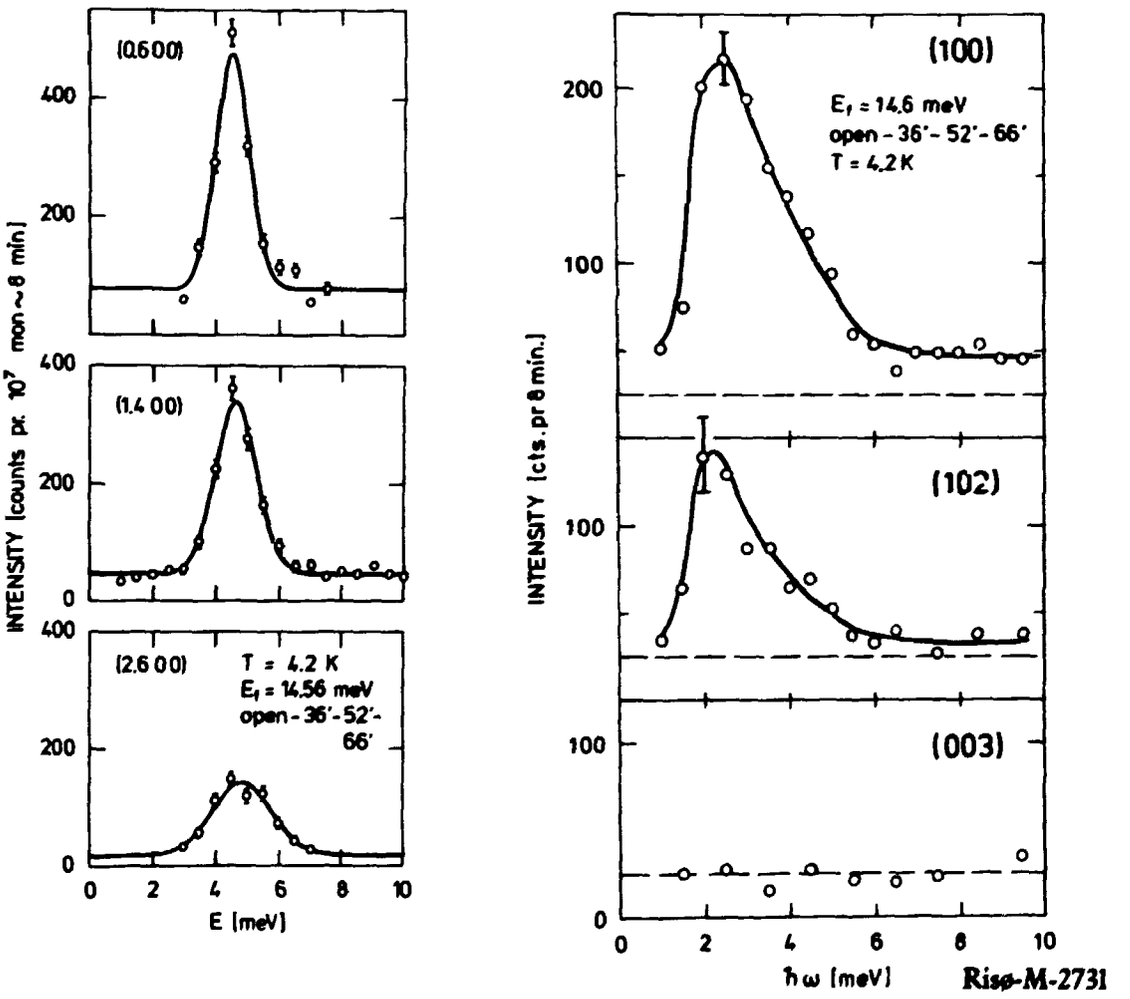

The left and right panels correspond to reduced momentum transfer q = (0.600) and q = (100) respectively. We see immediately that the response at the antiferromagnetic zone-center, q = (100) peaks at roughly half the energy of that of the response at q = (0.600). The resonance energy thus depends on the associated modulation symmetry; the fluctuations are dispersive. The dispersion along with the finite q resolution of the spectrometer is responsible for the assymetric broadning of the peaks at the antiferromagnetic zone center to higher energies. This is a purely experimental artifact.

The reduction of the intensity when increasing the total momentum transfer in the left part of the figure is consistent with the inelastic scattering being of magnetic origin. Phonon scattering on the other hand would increase in intensity with increasing momentum transfer. The rate of decrease versus Q is found to be roughly consistent with the variation of the squared U form-factor in the insulating oxide UO_2 found in Ref. [97]. Note that in the left series of scans the orientation of the scattering vector remains along the a* direction.

In the right side of the figure, however, the component of the scattering vector along c* is increased between the symmetrical equivalent antiferromagnetic zone centers (100), (102) and (003) We find that the intensity decreases and finally vanishes when the scattering vector is oriented along c*. Since the scattering at (003) arises from basal plane magnetic fluctuations, we conclude that there are indeed no such in this energy window. We may thus characterize the excitations as longitudinal with respect to the ordered moment.

The dispersion relation has been measured along high symmetry directions in the *(h0l)* plane [141] and is shown in Figure 4.4. Our energy scans were very complicated close to (200) which has the full nuclear structure factor 38.8 b. Our data indicate the existence of some hybridized exciton-phonon modes here. To distinguish clearly between phonon and exciton scattering we however lack a polarized neutron scattering experiment.

The integrated intensity did not vary in a simple way (eg. $1/\hbar\omega_q$, see A.3.2) along the dispersion branches. In particular the inelastic scattering completely disappeared for momentum transfers

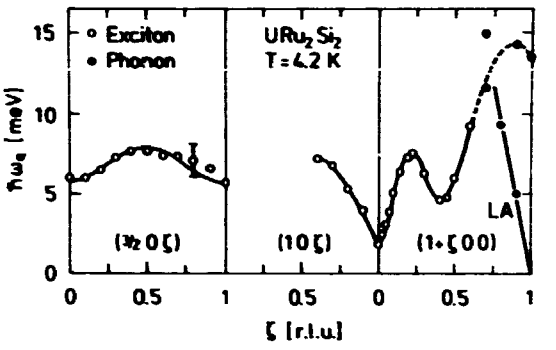

Figure 4.4. Dispersion of magnetic (filled circles) and phonon (open circles) excitations along (3/20ζ), (10ζ) and (1+ζ00) at T = 4.2 K. Half-filled circles denote a hybridized exciton-phonon mode. The lines are guides to the eye.

increasingly displaced from the antiferromagnetic Bragg point along the c* axis as shown in Figure 4.5. The inset shows the integrated intensity and excitation energy versus momentum transfer along c*.

4.2.3. Overdamped response

We now turn to the low-temperature magnetic excitations at energies well above the propagating excitations just described. Figure 4.6 shows constant q scans at four different reciprocal lattice points. The data were taken with the experimental configuration #3 of Table 4.1. With this configuration we could resolve the cross section associated with the propagating response and still obtain an appreciable count rate from the high-

Figure 4.5. Energy scans at T = 4.2 K in URu_2Si_2 for momentum transfers displaced along the c axis from the antiferromagnetic zone center (10ζ). The inset shows the excitation energy and integrated intensity of these scans versus ζ. The lines in this figure are guides to the eye.*

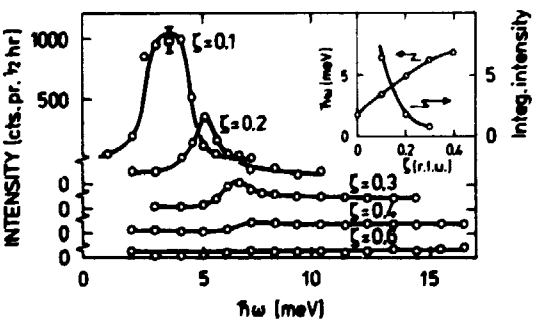

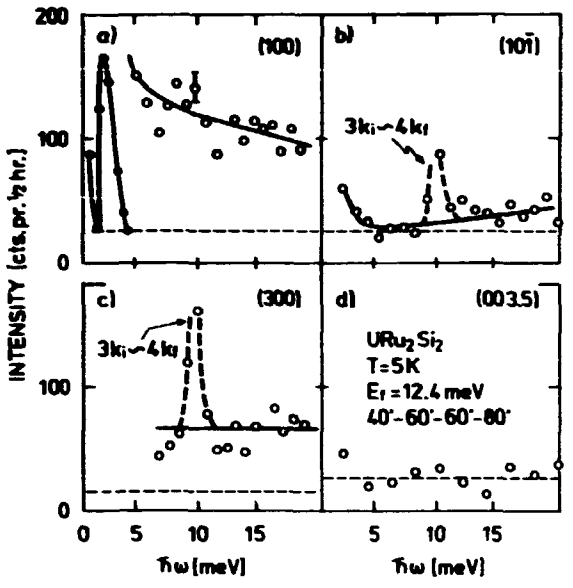

Figure 4.6. Low temperature energy scans at 4 different reciprocal lattice points. The lines through the data are guides to the eye. The broken line is the background as measured with the analyzer turned away from reflection. The peaks in (b) and (c) arise from a spurious process presumably involving third order neutrons.

energy continuum response to which this chapter addresses itself. The fast neutron background, as measured with the analyzer turned away from reflection, is indicated with a broken line in the figures.

Figure 4.6.a shows a constant q scan at the antiferromagnetic zone centre q = (100). Apart from the low-energy zone centre excitation, discussed in the previous chapter, the count rate from 5-20 meV is clearly well above background. To investigate the origin of this scattering we performed a similar scan, Fig. 4.6.c, at (300). The translational symmetry of the uranium lattice ensures that the magnetic scattering has the same spectrum here. Apart from a spurious process involving higher order neutrons, the level of scattering at (300) has decreased significantly as compared to that at (100). This observation is consistent with the scattering at (100) being primarily of magnetic origin. The decrease in the scattering at larger momentum transfer is then caused by the finite spatial extent of the magnetic moment density, through the magnetic form factor. Phonon scattering, on the other hand, is proportional to the squared momentum transfer and thus increases with increasing momentum transfer.

In Fig. 4.6.d we show an energy scan at q = (003.5). Due to the dipolar nature of the magnetic neutron scattering the only contribution to the magnetic scattering at this momentum transfer arises from the spin components in the basal plane of the tetragonal structure. We conclude that to within experimental accuracy there is no magnetic scattering from basal-plane spin components in the investigated energy region. With respect to the tetragonal uranium lattice q = (003.5) is symmetrically equivalent to q = (100.5). As we shall see later the scattering at (100) decreases by a factor of 2 when moving to (100.5). Had the scattering therefore been isotropic one would expect the q = (003.5) scan to be similar to the (100) scan, albeit reduced by a factor of 2. The complete absence of scattering at q = (003.5) therefore shows that there is a strong anisotropy of the high-energy response, similar to that of the low energy exciton response, i.e. the scattering arises from magnetic fluctuations oriented along the c axis and the ordered moment. It is termed longitudinal with respect to the ordered moment.

Turning now to the dependence of the high energy response on the location of the reduced momentum transfer in the Brillouin zone, Fig. 4.6.b shows an energy scan at q = (101). Since this is an allowed nuclear Bragg peak of the body-centered tetragonal structure, the magnetic scattering here arises from in-phase fluctuations of the magnetic moment densities associated with each uranium atom. Apart from the higher-order spurious process at an energy transfer of around 10 meV, there is very little magnetic scattering in the window from 5-20 meV. The spectrum of Fig. 4.6.a is thus specific for fluctuations of the same symmetry as the static antiferromagnetic order described in 4.2.1.

Figure 4.7 shows a constant energy scan at an energy transfer of $\hbar\omega$ = 17 meV. Momentum transfer is varied along the (10ξ) direction through the antiferromagnetic zone centre (100). Since these data were taken in an energy regime with no sharp features in the response we relaxed the energy resolution of our instrument by using configuration #4 of Table 4.1. The scan connects the previously discussed energy scans at the top of Fig. 4.6. The high energy response decreases monotonically when varying momentum transfer from probing antiferromagnetic, (100), to ferromagnetic, (10 ± 1), fluctuations. From the width of the peak in this scan we conclude that the correlation length associated with the magnetic

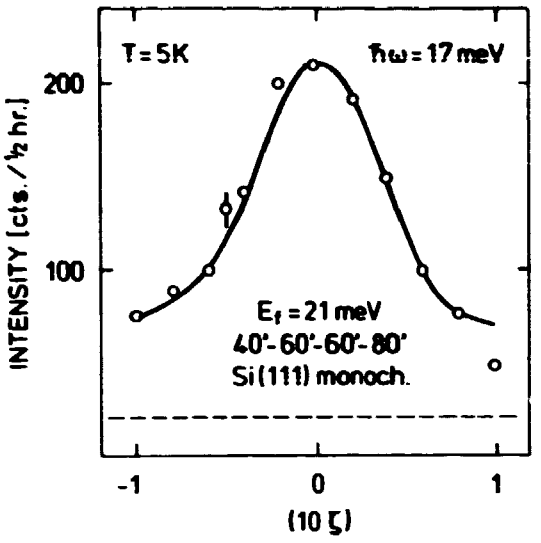

Figure 4.7. Constant $\hbar\omega$ = 17 meV scan in the ordered phase of URu_2Si_2 through the antiferromagnetic zone center at (100).

fluctuations probed in Fig. 4.6.a is only about one lattice unit.

To illustrate the cross over from the low-energy propagating response to the high-energy overdamped response, Fig. 4.8 shows data from both regions of energy and momentum transfer taken with configuration #3 of Table 4.1. The data are displayed in a 3d perspective as a function of energy transfer, and momentum transfer along the (10ζ) direction. The data should be studied with reference to the dispersion relation of the propagating excitation shown in Fig. 4.4. The peak at $\hbar\omega \sim 2$ meV corresponds to the divergent response at the minimum zone centre energy. At slightly higher energies ($\hbar\omega \sim 4$ meV) a double peak structure emerges, corresponding to the two equivalent directions of propagation (10ζ) and (10ζ). The asymmetry in the data at $\hbar\omega = 4$ meV is due to a resolution effect. Finally, above 5 meV the continuous spectrum of antiferromagnetically correlated spin fluctuations emerges. The data of Fig. 4.8, in which both a divergent and a continuous part of the spectrum is resolved, proves that the broad part of the response does not arise from unresolved sharp features such as fast spin waves.

Finally, we note that similar high-energy features have been observed at other high-symmetry points in the (h0l) plane, but are currently not as well documented as the scattering described in this chapter.

Figure 4.8. Perspective view of the scattered neutron intensity versus energy transfer and momentum transfer along (10ξ). The data are taken in the ordered phase of T = 5 K. The asymmetry in the double peak structure is due to a resolution effect. The solid lines are guides to the eye.

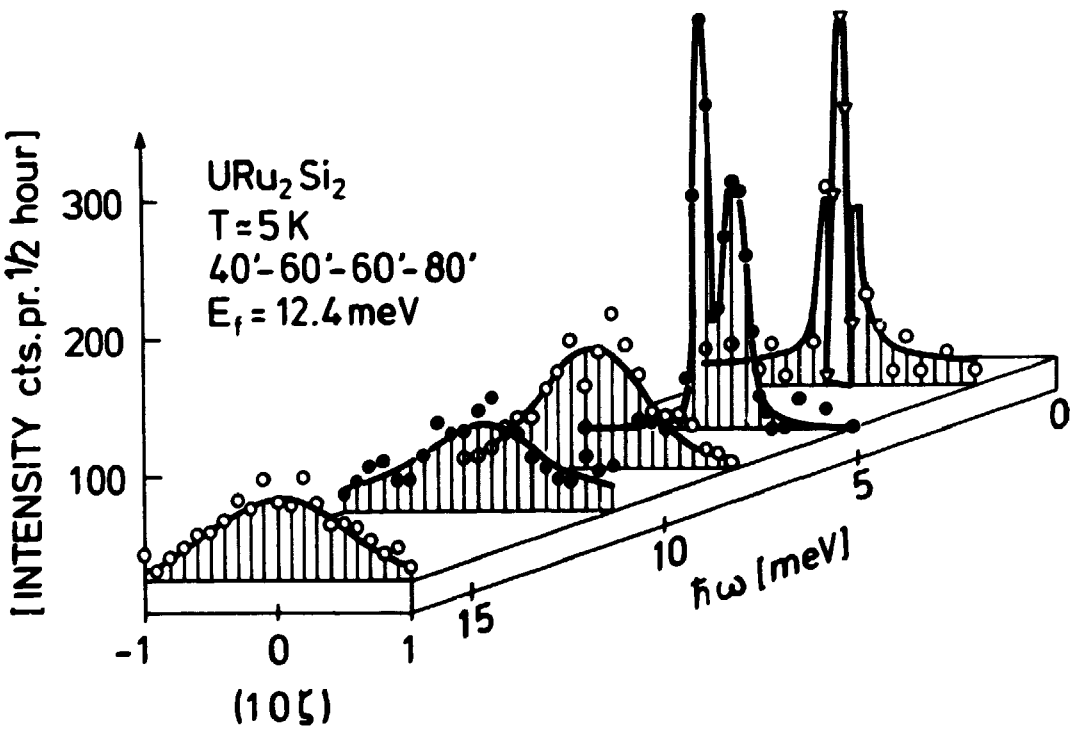

4.2.4. Development of Antiferromagnetic Correlations below T ~ 100 K

We turn now to the temperature dependence of this high-energy antiferromagnetic response. As mentioned in the introduction, 4.1, URu_2Si_2 has an anomalous resistivity maximum at T ~ 70 K. In the Kondo lattice picture of heavy Fermion systems, such a resistivity maximum is usually associated with the onset of correlations in scattering of conduction electrons from magnetic fluctuations. One might expect there to be a relation between such correlations and correlations in the magnetic fluctuations due to the active role of the conduction electrons in establishing RKKY interactions. To study such effects we measured the antiferromagnetically correlated overdamped magnetic fluctuations as a function of temperature above and below T ~ 100 K.

Figure 4.9. Energy scans at the antiferromagnetic zone center at 3 different temperatures. The broken line is the background as measured with the analyzer turned away from reflection. The full lines are guides to the eye.

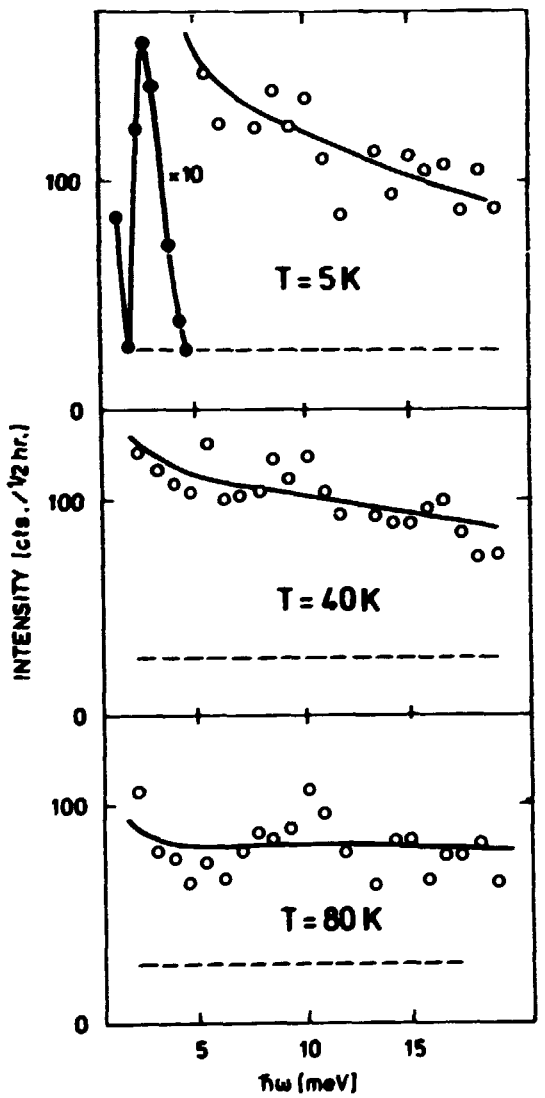

Figure 4.9 shows the energy scan at (100) taken at 3 different temperatures. As discussed in detail in 4.2.5 the low-energy propagating response becomes heavily damped when heating above the phase transition at T_N = 17.5 K. From Fig. 4.9.b it is, however, evident that the high-energy response remains almost unaffected by this transition to temperatures as high as 40 K. We may note that this fact rules out the interpretation of the continuous high-energy response as arising from two-magnon scattering. Had this been the case one would expect the high-energy scattering to be qualitatively changed at the 17.5 K phase transition.

At T = 80 K there is some decrease of the scattering below 10 meV. We note that the tendency of decreasing low-energy scattering with temperature, in fact indicates that the imaginary part of the generalized susceptibility in this energy regime decreases more rapidly than 1/T. This is because the detailed balance factor, which occurs as a factor to the imaginary part of the generalized susceptibility in the neutron scattering cross section (1.1), is proportional to the temperature T, for energy transfers much smaller than the thermal energy.

To determine the qualitative behaviour of the antiferromagnetic correlations discussed in 4.2.3 versus temperature we have measured 2 characteristic points in q, $\hbar\omega$ space as a function of temperature. The result is shown in Fig. 4.10. This figure shows the scattered neutron intensity at an energy transfer of 8 mev and at q = (101) and q = (100). The two q points, as discussed in 4.2.3, correspond to fluctuations of ferromagnetic and antiferromagnetic symmetries, respectively.

From the figure it is clear that, whereas the fluctuations at q = (101) with decreasing temperature decrease in approximate correspondence with the detailed balance factor, $(1 - \exp(-\beta\hbar\omega))^{-1}$, the scattering at q = (100) is slightly enhanced at temperatures below ~ 100 K. This was also noted in the context of Fig. 4.9. we summarize that the antiferromagnetic correlations discussed in 4.2.3 develop at temperatures of the order 100 K, $\sim 5 \times T_N$.

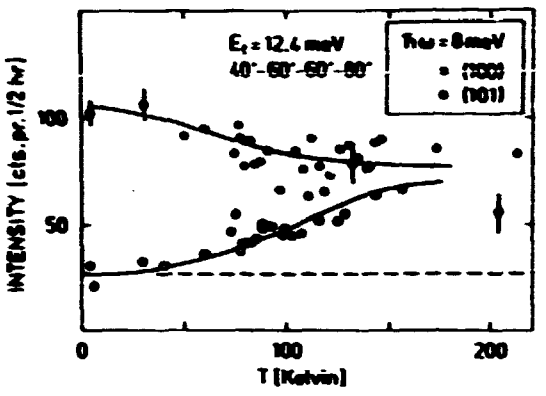

Figure 4.10. Scattered neutron intensity versus temperature at an energy transfer of 8 meV and momentum transfer (100) (●) and (101) (○). The broken line is the analyzer-turned background. The full lines are guides to the eye.

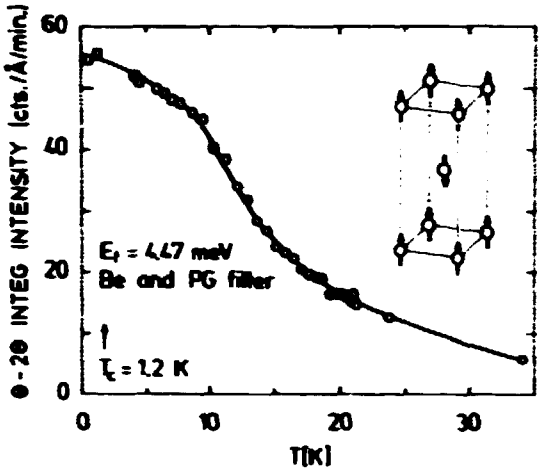

Figure 4.11. Integrated elastic magnetic scattering at (100) as a function of temperature. The c axis was perpendicular to the scattering plane in this experiment. the inset shows the corresponding antiferromagnetic structure.*

4.2.5. The Antiferromagnetic Phase Transition

The weak elastic antiferromagnetic peaks which were shown in 4.2.1 appear at temperatures below the phase transition at T_N = 17.5 [55]. Figure 4.11 shows the temperature dependence of the integrated intensity of θ-2θ scans through the antiferromagnetic peak at (100) The data were taken with configuration # 5 of Table 4.1. This experimental setup provides first of all a minimal content of λ/2 neutrons, which give rise to nuclear Bragg scattering from (200). Furthermore, the energy resolution of 0.2 meV provides an effective discrimination against the large inelastic cross section studied in 4.2.2. As we shall see later in this chapter, above T_N, this inelastic magnetic scattering is heavily damped and extends all the way to $\hbar\omega = 0$. Within the resolution volume of this experiment the inelastic scattering extrapolated to $\hbar\omega = 0$ throughout the temperature region studied, however, only contributes a count rate corresponding to less than 5% of the low temperature antiferromagnetic peak intensity. The temperature-dependent scattering studied here is a distinct, approximately elastic component of the antiferromagnetic zone center scattering even in the immediate vicinity of T_N.

The integrated intensity of Figure 4.11 developes continuously in the whole temperature region, and in particular does not vanish until well above T_N, the temperature at which there is an abrupt anomaly in the specific heat.

As shown in Figure 4.1 the correlation length of the antiferromagnetic order along the tetragonal c-axis remains finite to the lowest temperatures. The data of Figure 4.11 were taken with this axis normal to the scattering plane, which is the direction of coarsest momentum resolution. The momentum resolution was thus 0.1 $Å^{-1}$ full-width- at-half-maximum along the direction of finite correlations. Despite this, it is clear from Figure 4.1 that the integration of the elastic scattering along c* is incomplete, and an evolution of the correlation length along this axis also affects the integrated intensities of Figure 4.11.

To separate the temperature dependence of the correlation length and the size of the ordered moment we performed scans through the antiferromagnetic peak, along the direction of finite correlations, c*, in the temperature range 0.57 K-60 K. These data were collected with the c* axis in the scattering plane and with the same configuration (# 1) as used for Figure 4.1. Also this configuration is only sensitive to the central elastic component of the magnetic scattering, due to the energy resolution of 0.2 meV. We deduced the ordered moment and the inverse correlation length as a function of temperature from these scans with the formalism discussed in 4.2.1.

The result of the measurement and subsequent analysis is shown in Figure 4.12. The inset of the lower frame shows a scan at T = 60 K, constituting the incoherent nuclear background of the

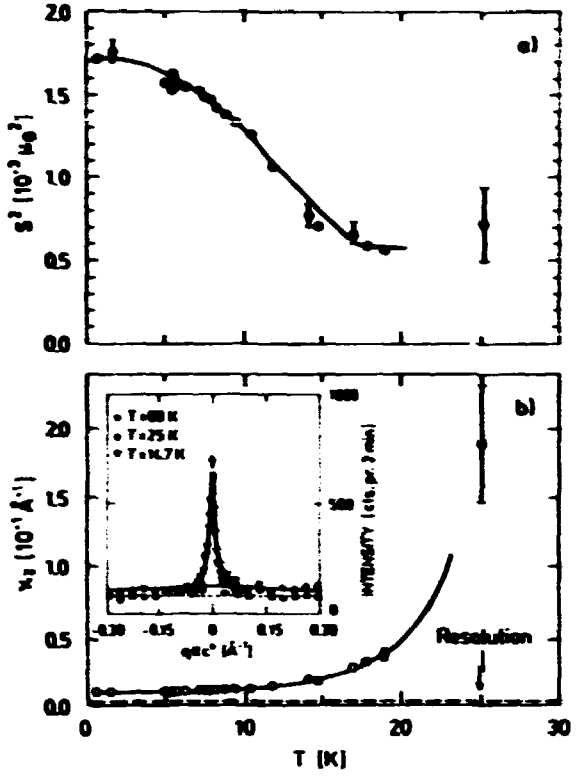

Figure 4.12. Temperature dependence of the antiferromagnetically ordered moment and its associated correlation length along c through the antiferromagnetic phase transition at T_N = 17.5 K. The data has been deduced from transverse scans through (100) of which a representative selection is shown in the inset.*

measurement, a scan at T = 25 K, well above the phase transition, and a scan at T = 14.7 K, below the phase transition. The inverse correlation length evolves continuously in the whole temperature range, and in particular remains finite even well above T_N. The ordered moment, on the other hand, is temperature independent from 25 K to T_N and then increases rapidly below T_N.

The finite value of S^2 even well above T_N. can be seen directly in the inset of the bottom frame. It shows that there is temperature dependent scattering above the T = 60 K nuclear incoherent background, and that at 25 K this scattering is independent of momentum transfer along c*.

The fact that the correlation length of this elastic, antiferromagnetic scattering does not diverge at T_N, suggests that it is not responsible for the anomaly in the specific heat [55] which is clear evidence of a real phase transition.

The heat capacity anomaly is, however, accompanied by the abrupt development of the low-energy propagating excitations. This is illustrated by Figure 4.13. The data of Figure 4.13.a were taken with a focusing analyzer (configuration 6 of Table 4.1) which ensured a good energy-resolution along with a course q-resolution. In Figure 4.13.b,c the analyzer was flat (configuration 7 of Table 1). The data taken at different configurations have been normalized as described in the figure caption. All the energy scans are taken at q = (1 0.4 0) where the intensity of the magnetic excitation is largest above T_N.

Figure 4.13 shows that the excitation develops from a broad hump of antiferromagnetically correlated heavily damped scattering in the paramagnetic phase to an almost resolution limited peak which is largely unaffected by the superconducting phase transition at T = 1.2 K.

Figure 4.13. Constant-q scans at q = (1.0,4.0) in (a) the paramagnetic, (b) the antiferromagnetic, and in (c) the superconduction phase. The fixed final energy was 5 meV. (a) was measured with a horizontally focusing analyser. In (b) and (c) the collimation was 60'-60'-53'-66'. The data taken with different analyser configurations have been normalized, and plotted so equivalent cross sections correspond to the same height over the background. The solid lines in (a) - (c) are fits as described in the text, and (d) - (f) show the temperature dependence of the three parameters obtained from fits to data similar to (a). The lines through these points are guides to the eye.

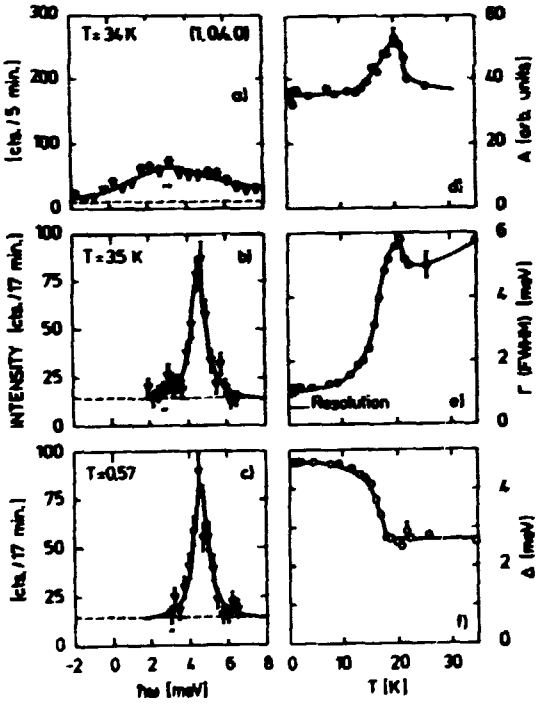

We have summarized a series of scans similar to Fig. 4.13.a as a function of temperature in the right side of the figure. Here we show the temperature dependence of the amplitude, A, dumping Γ (FWHM), and first moment, Δ, of a resolution- and background-corrected Lorentzian response which describes our data well. The abrupt temperature dependence of Γ and Δ at T_N accounts for the anomaly in the heat capacity at this temperature, but is surprising in light of the small ordered moment associated with the phase transition (Figure 4.12).

4.2.6. The antiferromagnetic Order in the Superconducting Phase

As is evident from Figure 4.12 there is no big effect on the antiferromagnetic order when entering the superconducting state. Figure 4.14 shows the (10ξ) scans giving rise to the two low temperature points in Figure 4.12. At the bottom of the figure is shown the difference in intensity through the scan in the superconducting phase ($T = 0.57 \sim T_c/2$) and in the normal phase ($T = 1.6$ K $\sim 1.6\ T_c$). From this data we may place an upper bound of 10% on the change of intensity in any point of the scan upon entering the superconducting phase.

Figure 4.14. Elastic scan along the c axis through the antiferromagnetic peak a (100) below and above the superconducting phase transition. The bottom frame shows the difference between the two scans.*

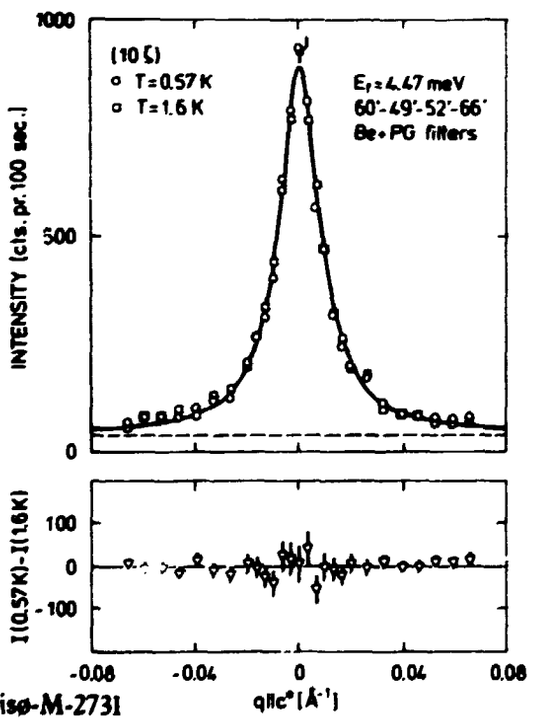

We have also studied the low energy propagating excitations through T_c both at q = (100) and q = (10.40), the two minima in the basal plane dispersion relation (Figure 4.4). The data for q = (10.40) is shown in Figure 4.13.b,c. To within the experimental accuracy of ~ 15%, there is no change in the energy, width or intensity of these excitations upon entering the superconducting phase.

4.3. Analysis and Discussion

It is clear from 4.2.2 that the low energy magnetic excitation spectra in URu_2Si_2 at low temperatures bear striking similarities to those of conventional rare earth systems. The analysis of such systems has come very far treating the 4f electrons as essentially perfectly localized and subject to interatomic correlations constricting their motion to the Hund's rule ground-state multiplet [142]. Also many of the bulk properties of URu_2Si_2 seem to be governed by the same underlying physics as is known from rare earth magnetism [143]. We mention briefly the strongly anisotropic susceptibility and its Schottky like anomaly at T ~ 70 K [55], and the high field magnetization data which show step like magnetization increases in fields around 35 T [131].

There are however, as shown in 4.2.3, features in the high energy magnetic response which certainly cannot be contained within conventional spin wave/crystal field theories, nor have they to date been observed in the excitation spectra of systems we think of as conserved local moment magnets (1.1). Features in the bulk properties such as the heavy Fermion linear specific heat term (γ = 180 mJ/mol K^2 [55]) and the increasing resistivity with temperature decreasing from room temperature, also suggest that we cannot accomodate the properties of this compound within this tractable physical model. We however believe that despite these important discrepancies we can use the conserved local moment model as a mean of parameterizing dispersion relations and gap energies and conveniently relating these to some key bulk properties [143,144]. To some extent this can even be done without relying on assumptions known to be doubtful.

Subsequently we will discuss the points in which this model definitely falls short and with these the high energy magnetic response and its relation to the anomalous bulk properties of the compound. Finally we will discuss the magnetic

fluctuations in URu_2Si_2 in the light of the introduction to this thesis.

4.3.1. Applying Crystal Field theory to URu_2Si_2

One can argue that the resonant low-energy spin response shows that there exists dipolar moments whose size is an approximately conserved quantity in the motion of the unpaired 5f electrons. The moments, however, have a high energy channel of decay (Figure 4.8).

There is a large transition matrix element associated with the low energy resonant response. From an energy scan at (100), the antiferromagnetic zone center, we deduce (see Appendix A.3.2)

$$g\,\mu_B\,|<0|J^z|1>| = (3 \pm 1)\,\mu_B$$

If we must reconcile this value with an ordered moment almost 2 orders of magnitude smaller, the ground state must be a singlet. This then immediately means that an even number of electrons must be accomodated in 5f states of the U atom. An uneven number would give rise to a Kramers-doublet ground-state with a sizeable moment. Of the two ionization levels in which U most frequently occurs, U^{4+}, U^{3+}, we must therefore choose the U^{4+} which has a $5f^2$ configuration. The Hund's rule ground state is $^3H_4$. From group theory we get the level scheme and associated possible dipolar transitions in tetragonal symmmetry: the $2J + 1 = 2 \cdot 4 + 1 = 9$ levels split into 5 singlets A_1, $2 \times A_2$, B_1, B_2 and two doublets $2 \times E$ with the above allowed transitions.

Table 4.2. Allowed transitions between the crystal field states of a J = 4 multiplet in tetragonal point group symmetry. The states are labelled by their associated irreducible representations. O_2^2 denotes the quadropolar operator.

	A_1	$2A_2$	B_1	B_2	$2E$
A_1		J^z	O_2^2		J^{+-}
A_2	J^z			O_2^2	J^{+-}
B_1	O_2^2			J^z	J^{+-}
B_2		O_2^2	J^z		J^{+-}
E	J^{+-}	J^{+-}	J^{+-}	J^{+-}	J^z, O_2^2

To elucidate the symmetry of the excited state we note that it is connected to the ground state by a longitudinal, or J^z, transition (see Figure 4.3). From Table 3.2 we see that it must then also be a singlet, since the doublet, E, is only connected to the singlets by transverse, J^{+-}, transitions. On the other hand from the absence of transverse magnetic response, as is evident from the neutron scattering data (Figures 4.3 and 4.6) and the bulk susceptibility [55], which is temperature independent along the a axis, we conclude that the two doublets, E, must both be at energies well above 30 meV. From our knowledge of the high energy response, we would not expect the transverse response to be resonant, but rather spread out over a large energy range, and thus difficult to observe by thermal neutron scattering.

From the combination of experimental and group theoretical results we may now set up a model of the generalized susceptibility. First we write down the "bare" or single site susceptibility of one uranium ion. The Lehman representation of the response function is [145]

$$\chi^{\alpha\beta}(\omega) = (g\mu_B)^2 \lim_{\varepsilon \to 0^+} \sum_{pr} \frac{\langle p \mid J^\alpha \mid r\rangle\langle r \mid J^\beta \mid p\rangle}{E_p - E_r + \hbar\omega + i\varepsilon}(n_r - n_p)$$

where p and r index eigenstates of the system E_p,E_r are the associated energies and $g = 4/5$ is the Landé factor of the $^3H_4$ multiplet. (For ease of notation, whenever an expression contains $\hbar\omega$ the limit of it with $\hbar\omega$ substituted by $\hbar\omega + i\varepsilon$ for $\varepsilon \to 0^+$ is understood).

In a low energy and temperature regime we may restrict ourselves to contributions to the longitudinal susceptibility from transitions from the ground state. Denoting by Δ the energy of the first excited singlet we obtain

$$\chi^{zz}(\omega) = \alpha^2 \tanh\frac{\beta\Delta}{2}\left(\frac{1}{\hbar\omega + \Delta} - \frac{1}{\hbar\omega - \Delta}\right) = \frac{2\Delta\alpha^2 \tanh\frac{\beta\Delta}{2}}{\Delta^2 - (\hbar\omega)^2}$$

where

$$\alpha^2 = (g\mu_B)^2 \mid \langle 0 \mid J^z \mid 1\rangle \mid^2 .$$

The response function has poles at $\hbar\omega = \pm \Delta$.

From Figures 4.3 and 4.4 it is clear that there is a significant dispersion of this transition below T_N, so we introduce an RKKY interaction parametrized by the Fourier transformed exchange integrals: J_q for intersublattic coupling and J'_q for intrasublattice couplings.

In the RPA the resultant interacting susceptibility is given by

$$\chi_q^{zz}(\omega) = \frac{2\Delta\alpha^2 \tanh \frac{\beta\Delta}{2}}{\Delta_q^2 - (\hbar\omega)^2} \qquad (4.1)$$

where

$$\Delta_q^2 = \Delta(\Delta - 2\alpha^2 \tanh \frac{\beta\Delta}{2}(J_q + J'_q))$$

gives the associated poles, or the dispersion relation, of the propagating singlet-singlet transition.

We have used the fact that the site symmetry of the longitudinal response upon entry to the antiferromagnetically ordered state is not broken as it is for the transverse response. (i.e. $\chi_1^{zz}(\omega) = \chi_2^{zz}(\omega)$ where 1 and 2 label the 2 sublattices of the antiferromagnetically ordered state). And that the surroundings of the uranium site have inversion symmetry (i.e. J'_q is real). The longitudinal response in an inversion-symmetric antiferromagnet thus has the fascinating feature that the symmetry of the response in reciprocal space is unchanged at the phase transition. This is in contrast to the transverse antiferromagnetic response eg. of MnF_2 [146]. This basic symmetry is carried through in the experimental dispersion relation, Figure 4.4, supporting the interpretation of the response as longitudinal.

Since Δ^2_q is a Fourier series with the translational symmetry of the lattice it can be brought to fit the measured dispersion relation by including interactions of sufficiently long range. We can estimate the range of interactions directly by studying Figure 4.4 and the body-centered tetragonal structure shown in the inset of Figure 4.11.

Along the (3/2 0 ζ) direction the interactions between body-centered atoms and atoms in the basal planes displaced c/2 above and below cancel for symmetry reasons. Only interactions between atoms displaced immediately above and below each other by the distance c contribute. Since the dominant modulation in the dispersion relation along this direction from Figure 4.4 is found to have a period of 1 r.l.u, we conclude that the interaction between neighbours separated 2·c along the c axis is negligible compared to the interaction between neighbours displaced by the distance c. The experimental result that the excitation energy is larger at (3/2 0 1/2) than (3/2 0 0) shows that this interaction is ferromagnetic. The modulation of about 2 meV along (3/2 0 ζ) is a measure of the strength of this interaction.

The dispersion along the (1 0 ζ) branch is larger than that along (3/2 0 ζ). This shows that the interactions between nearest neighbour atoms in basal planes separated by c/2 is antiferromagnetic.

Finally, the dispersion relation in the basal plane (1+ζ 0 0) shows that there are competing long range interactions between atoms displaced along a. In particular, the interaction among nearest neighbours in the basal plane is antiferromagnetic since there is an overall increase in the excitation energy between (100) and (200). The local maximum in the dispersion relation for $\zeta \sim$ 1/4 r.l.u. shows that the interactions between neighbours displaced 2a along the a-axis are antiferromagnetic and comparable in strength to the nearest neighbour interaction. The local minimum in the dispersion relation at a low symmetry point in the basal plane, (1.4 0 0), is a result of the competition between these two interactions. H. Lin et al. [147], have obtained reasonable fits to the dispersion relation including 7 nearest neighbour exchange constants.

The two level model predicts the energy-integrated scattered intensity to vary as $1/\Delta_q$ (this is seen by taking the imaginary part of $\chi_q(\omega)$ as is done in Apendix A.3.2). From Figure 4.5 it is however clear that the integrated intensity falls off much more rapidly than does the inverse of the peak position in energy scans at momentum transfer (10ξ).

Also the bulk susceptibility shows that a two-level model is oversimplified even at temperatures below 100 K. The bulk susceptibility in the paramagnetic region is a monotonically decreasing function of temperature, through its dependence on the population difference of the 2 levels. In a 2-level system the susceptibility reaches its maximum at T_N or just above. A crystal field system with 2 excited states which are connected by a dipolar operator, however, displays a susceptibility maximum when the population difference between these two states is maximal. The peak at $T \sim 50$ K $\sim 3 \times T_N$ in the bulk susceptibility of URu_2Si_2 [55] thus indicates that at least 3 dipolar-active singlet states govern the magnetic properties below $T \sim 150$ K. We may in fact

estimate the third singlet state to be close to 150 K, where the inverse susceptibility starts to deviate markedly from the Curie Weiss law [55]. From Table 4.2 a possible low energy crystal field scheme is A_2 - (J^z) - A_1 - (J^z) - A_2, with no allowed dipolar transition between the ground-state singlet and the highest lying singlet state. The highest lying singlet can thus only be observed by neutron scattering as transitions from the excited state A_1, which must furthermore have an appreciable population. The cross section corresponding to the transition between the two excited states thus would only be appreciable in a temperature interval from about 50 -150 K. We have not made an exhaustive search for a cross section of this nature.

4.3.2. The Phase Transition at T_N = 17.5 K

When we turn to the phase transition whose manifestation by neutron scattering is shown in 4.2.1 and 4.2.5, we encounter further complications, whose explanations however do not necessarily preclude description within the crystal field picture. The large change in the energies of the lowest lying excitations, best illustrated by Figure 4.13.f, must clearly be responsible for the λ-like anomaly in the heat capacity at T = 17.5 K [55]. Indeed the low entropy change of 0.2 R ln2, deduced from the heat capacity data, agrees well with the phase transition being related to the shifting of an excited singlet state beyond reach of thermal population. Clearly, however the small ordered moment of ~ 0.04 μ_B cannot give rise to so large a shift, since it enters the mean-field Hamiltonial as an off-diagonal term and thus is a second order effect. These remarks may be put on firmer footing within the 2 level scheme. From (4.1) we see that the static susceptibility diverges giving rise to a finite expectation value, $<S_q>$ at $q = q_0$ when

$$\Delta_{q_0} = 0 \quad \Leftrightarrow$$

$$\Delta = 2\alpha^2 \tanh\frac{\beta\Delta}{2}(J_{q_0} + J'_{q_0})$$

in the limit $\beta\Delta >> 1$ we get the RPA criterion for ordering in a 2 level system:

$$\eta = \frac{2\alpha^2(J_{q_0} + J'_{q_0})}{\Delta} \geq 1$$

the critical temperature is then given by

$$\tanh\frac{\Delta}{2k_BT_N} = \eta^{-1} \qquad (4.2)$$

the ordered moment at T = 0 is easily calculated by diagonalizing the 2 × 2 matrix of the mean-field Hamiltonian in the basis of the eigenstates in the paramagnetic phase:

$$m_{q_0} = \alpha\sqrt{1-\eta^{-2}} \quad \Leftrightarrow$$

$$\eta = \frac{1}{\sqrt{1-\left(\frac{m_{q_0}}{\alpha}\right)^2}}$$

putting this back in (4.2) we obtain

$$\Delta = 2k_BT_N \cdot \mathrm{A}\tanh\sqrt{1-\left(\frac{m_{q_0}}{\alpha}\right)^2}$$

putting in the experimentally determined values $m_{q0} \sim (0.04 \pm 0.01)\mu_B$, $\alpha = (3 \pm 1)\mu_B$ (Appendix A.5), T_N = 17.5 K, we obtain

$$\Delta = (15 \pm 1)\ \mathrm{meV}$$

a value about 5 times larger than the estimate of the singlet-singlet splitting in the paramagnetic phase of about 3 meV one may deduce from Figure 4.13.f.

In summary we cannot get a consistent description of the size of the ordered moment, the transition matrix element, the critical temperature and the paramagnetic transition energy within a simple 2 level model. Crystal field dynamics, despite of its conceptual simplicity, can however be extremely intricate in its experimental manifistations, and resonant levels can be unobservable by neutron scattering due to selection rules or vanishing population differences. There might therefore very well be room for a consistent description of the phase transition at 17.5 K within crystal field theory. For example we mention that sharp λ like anomalies of the order $5\cdot10^{-6}$ in the thermal expansion coefficients are observed at T_N [130]. This is indeed quite understandable since, as can be seen from Table 4.2, the singlet levels are coupled by the quadropolar operator O_2^2. The phase transition could therefore be an induced Jahn-Teller quadropolar transition of which 2 were found in the intermetallic UPd_3 at 5 K and 7 K [67,68]. In this compound the anomalies in the thermal expansion were an order of magnitude bigger than those

observed in URu_2Si_2 . One could however imagine that modulated quadropolar effects have varying influences on the thermal expansion which is a homogeneous, or q = 0, probe. We have no diffraction evidence for lattice rearrangements at T_N but can certainly not rule out that there is such an order parameter. The small antiferromagnetic moment would then be a side effect of this main order parameter.

The elastic antiferromagnetic scattering shown in 4.2.1 and 4.2.5 is indeed very puzzling. First of all the fact that the correlation length associated with the antiferromagnetic scattering remains finite to the lowest temperatures (Figure 4.1) is at odds with an interpretation of it as the order parameter of a phase transition.

Secondly, the temperature dependence of both the ordered moment and its associated correlation length is anomalous. Even well above T_N there is a small amount of elastic scattering along the c* axis which decreases between 25 K and 60 K. This corresponds to a small ordered moment in the basal planes which is however uncorrelated with neighbouring planes displaced along the c-axis. Between 25 K and T_N, there is a rapid, but continuous increase of the intraplane correlations. The phase transition is marked by the onset of a mean-field-like increase of the size of the finite range correlated antiferromagnetic moments.

These features bear some similarities to the so-called central peaks of rare earth magnetism. These are low-frequency long-wavelength fluctuations which appear at phase transitions in singlet ground state systems [148,142]. Such low frequency modes are known to be sensitive to crystalline imperfections. Our crystal did, as previously mentioned, have stacking faults along the c* axis giving rise to weak temperature independent rod-like scattering along this axis. We observed quantitatively similar antiferromagnetic peaks in two URu_2Si_2 single crystals, grown along and a an a c axis respectively. We cannot, however, rule out that the elastic antiferromagnetic scattering is dependent on stacking faults and impurities.

4.3.3. The High Energy Response

Whereas a large part of the low temperature susceptibility arises from the big dipolar matrix element between the ground state and the excited singlet states, the low temperature linear specific heat term of γ = 50 mJ/mol K^2 [55] is a signature of a continuous density of states which cannot be reconciled with the resonant responses characteristic of crystal field systems in their ground state. These give rise to exponential terms in the specific heat which are in fact also observed [138] in URu_2Si_2. As shown in 4.2.3 there are overdamped excitations above the crystal field excitations, which presumably are responsible for the linear specific heat term in URu_2Si_2. The characteristic energies of this response, Γ, is roughly an order of magnitude above that of the overdamped response of eg. U_2Zn_{17} (3.2.2). The specific heat γ of URu_2Si_2 is about an order of magnitude lower than that of U_2Zn_{17} . Γ^{-1} and γ thus roughly scale for these compounds, as predicted for example by the simple calculation of Appendix C.

The high energy response in URu_2Si_2 corresponds to a large susceptibility. As shown in Appendix A.5 $Im(\chi_{(100)}(10meV)) \sim 3 \cdot 10^{-2}$ emu/mole-unit cells. Converting to a fluctuating moment by integration of the spectrum we estimate the amount of moment participating in these fluctuations to be 0.6 μ_B/unit cell. So the overdamped response has an associated fluctuating moment comparable to that of the low-energy resonant response at (100). Also it has the same axial anisotropy as the low energy response.

In the lack of a rigorous theoretical framework in which to discuss the response we speculate that it is the signature of the hybridization of the f electrons with conduction electrons at the Fermi level. This speculation is based on the responses seemingly inheriting the anisotropy and form factor characteristics of the f electrons, but the continuous spectrum characteristic of conduction electrons in a metal.

The resistivity data further supports this idea [134]. It is largest and most strongly temperature dependent in the basal plane of the tetragonal structure, i.e. in the normal plane to the tetragonal c axis along which the dominant part of the low energy magnetic fluctuations are oriented. Also it is interesting to note that the antiferromagnetic correlations build up just above the temperature at which the basal plane resistivity passes through a maximum followed by a low temperature decrease by over an order of magnitude.

4.4. Summary

Our work on URu_2Si_2 leaves the impression of a compound which constitutes a mixture of many interesting physical properties, superconductivity, crystal field effects and strong conduction electron-f electron hybridization. It seems to be a borderline case between localized and itinerant magnetism which was also the conclusion of Palstra [136].

We have hardly discussed the superconducting properties of the compound which are highly interesting [55]; for example there is a large anisotropy of the upper critical field Hc_2. It is largest and has an unusual concave behaviour for fields in the hard magnetic tetragonal ab plane. Also the change in entropy at the superconducting phase transition is large and of the order of the entropy associated with the large linear term in the specific heat. There are thus strong indications that the superconducting properties are related to the anomalous magnetic properties of the compound. We have, however, to within experimental accuracies of typically 10%, found no effect on the static or dynamic magnetic properties when entering the superconducting phase.

The magnetic properties are strongly influenced by crystal-field-like effects on f electrons with strong spin-orbit coupling. The very small ordered moment of $(0.04 \pm 0.01)\mu_B$ which develops at $T_N = 17.5$ K, but does not attain infinite range correlations even in the superconducting phase, could be a side effect of an induced quadrupolar transition between singlet levels unobservable by neutron scattering.

In our opinion the most interesting result of this work is the discovery of a high energy overdamped response in a metallic magnet with a low energy regime of approximately conserved local moments. This response has the form factor, anisotropy and antiferromagnetic correlations of the low-energy crystal-field-like response, but the continuous density of states characteristic of a conduction electron band. This is the magnetic response which relates URu_2Si_2 to the other heavy fermion compounds.

It is fascinating that a low energy regime of conserved local moment dynamics can coexist with magnetic fluctuations which show that the same 5f electrons acquire some itinerant properties, most notably a finite bandwidth. We speculate that the extent of participation of the 5f electrons in metallic properties is strongly dependent on the degeneracy of the crystal field ground state of their lowest lying valence level. To be specific, singlet states presumably "survive" the conduction electron hybridization and virtual interconfigurantional fluctuation of the uranium atoms due to their inert magnetic properties and give rise to the low energy propagating excitations of URu_2Si_2. Whether or not the phase transition at $T_N = 17.5$ K is directly related to these considerations, or can be described within crystal field theory for the low-energy conserved- local-moment regime remains an open question.

5. Conclusion

We have studied three heavy Fermion systems experimentally by a variety of neutron scattering techniques. The specific results for these systems were summarized in 2.4 (UPt_3), 3.4 (U_2Zn_{17}) and 4.4 (URu_2Si_2). Here we shall sum up results of a qualitative nature which may have a more general validity in the physics of heavy Fermion systems.

The magnetic fluctuations of uranium-based heavy Fermion systems can be characterized as exchange-enhanced relaxational fluctuations. The 5f electrons loose their characteristic free-ion singular dipolar excitation spectra due to the interconfigurational fluctuations induced by the metallic environment. We have argued that the continuous low-energy magnetic fluctuation spectra give rise to the characteristically large linear specific heat terms in heavy Fermion systems. The localization of 5f electron density around uranium atoms and the associated atomic correlation of these electrons causes some characteristic features of conserved local moment systems to survive. For example, the spatial correlation of both magnetic fluctuations and magnetic order in heavy Fermion systems can be derived from RKKY exchange interactions between spin and orbital moment localized at uranium sites. We have put forth a simple phenomenological model which relies on this analogy of the magnetic fluctuations in these itinerant f electron systems, and those in conserved local moment systems.

Crystalline anisotropy has also been found to play a similar role on the relaxational magnetic fluctuations of heavy Fermion systems, as it is known to do on the singular magnetic response of conserved local moment magnets. In U_2Zn_{17} we have explicitly shown that different relaxation energies are related to the two transverse modes of the ordered state. A related, important result on this system was the observation that longitudinal magnetic fluctuations in the ordered state were not exchange enhanced.

Crystalline anisotropy might very well be an important factor in determining the occurance of heavy Fermion behaviour. URu_2Si_2 was thus found to have a high-energy relaxational magnetic excitation spectrum similar to that of other heavy Fermion systems, but a crossover to a regime of propagating singlet-singlet excitations at lower energies. The fact that these inert magnetic singlet states "survive" the strong conduction-electron hybridization makes some of the bulk properties of this system bear similarities to conserved local moment systems.

The heavy Fermion systems are close to an antiferromagnetic instability. Despite large values of the Curie Weiss temperature, Θ_{cw}, many heavy Fermion systems do not order antiferromagnetically, and those that do generally have Néel temperatures an order of magnitude below Θ_{cw}. Our experiments show heavy Fermion systems with an anomalously large temperature range, of order T_N, in which the systems are close to criticality. Furthermore, the q averaged energy associated with the relaxational magnetic fluctuations is of the same order as $k_B\Theta_{cw}$. Our inelastic neutron scattering data from U_2Zn_{17} at temperatures around T_N may be interpreted as the RKKY exchange driving the system critical rather than the increasing "bare" single site susceptibility as is the case in conventional antiferromagnets.

Two of the systems we have studied were shown to develop anomalously small antiferromagnetically ordered moments at low temperatures. (UPt_3 : $\mu = (0.02 \pm 0.005)\ \mu_B$, $T_N = 5$ K; URu_2Si_2: $\mu = (0.04 \pm 0.01)\ \mu_B$, $T_N = 17.5$ K) In URu_2Si_2, the phase transition also involves the abrupt development of the singular magnetic excitation spectrum of this compound. The antiferromagnetic phase transition in UPt_3 is associated with a broad peak in the temperature dependence of the antiferromagnetic zone-center inelastic magnetic neutron scattering at energy transfers below k_BT_N. In both systems the correlation length associated with the antiferromagnetic order remained finite to the lowest temperatures. Furthermore, the antiferromagnetic order had an anomalous mean-field-like temperature dependence until well below T_N. These minute ordered moments may be dependent on impurities and defects, but then the absence of a larger ordered moment, despite the documented proximity to criticality, is the important question that these experiments pose.

Superconductivity is another ground state frequently adopted by the heavy Fermion systems. Our experiments have provided proof of a direct relationship between antiferromagnetic and su-

perconducting properties in UPt_3. This supports the many suggestions for purely electronic superconductivity in these systems.

The experimental and theoretical work on heavy Fermion systems has shown that we are indeed far from a complete understanding of metallic magnetism. With the experience gained from investigations of heavy Fermion systems, experiments on systems closer to the limits we believe to understand could be the next step towards a first principles description of metallic magnetism.

Acknowledgements

It is a pleasure to take this opportunity to thank colleagues and friends who have been inspiring, supportive, helpful and insistant throughout my time as a PhD student.

I am first of all grateful to my primary supervisor Jørgen Kjems who has inspired and guided me throughout and most kindly and competently arranged these first important years of my career.

My sincere thanks goes to Gabriel Aeppli and W.J.L. Buyers for sharing with me their deep and different physical insight as well as experimental skill.

I am grateful to my second supervisor A.R. Mackintosh for his interest in my work and for arranging the formalities related to my PhD study.

I thank all my other collaborators without whom this work would not have been possible: J. Bauman, E. Bucher, Z. Fisk, P.H. Frings, J. Hufnagel, H. Lin, T. Mason, P. Matthews, A.A. Menovsky, J.A. Mydosh, H.R. Ott, T.T.M. Palstra, S.M. Shapiro, G. Shirane, K. Siemensmeyer, J.L. Smith and N. Stucker.

For his competent comments and explanations of theoretical issues I am very grateful to P.A. Lindgård. I am also thankful for the interest and help from all my scientific colleagues in the Physics Department at Risø.

The expert assistance of secretaries and technicians in this department is greatfully acknowledged. In particular I wish to thank Allan Thuesen, Mouritz Lund and Finn Dahlsøe for mounting samples, cooling cryostats and doing odd jobs, and Jens Linderholm, Keld Theodor and the Risø Workshop for making various tail pieces for dilution cryostats in record time.

I am grateful to The Angelo foundation for a grant and to the Danish Research Academy for financial support in connection with my visit to AT and T Bell Laboratories and Brookhaven National Laboratory during this thesis work. I also thank these two institutions and their staff for their hospitality. In particular I am grateful to Gabriel Aeppli who was my supervisor at Bell Laboratories, and Torsten Freltoft who was very kind and helpful during my stay at Brookhaven.

For their skilled assistance in preparing the figures and text of this thesis I am very grateful to Anna Taboryska, Tora Skov, Karna Hansen and Agnete Gjerløv

Finally I thank friends and family for their support and acceptance of my long working hours. In particular I thank my wife Monica and future child for accompanying me on several late nights in the final stages of the preparation of this thesis.

References

[1] K.A. Gschneidner, Jr. and Le Roy Eyring, Eds. Handbook on the Physics and Chemistry of Rare Earths. Vols. 1, 2. North Holland Amsterdam (1979).

[2] R.J. Elliott (ed.). Magnetic properties of rare earth metals. Plenum, London (1972).

[3] A.R. Mackintosh and H. Bjerrum Møller in R.J. Elliott (ed.). Magnetic properties of rare earth metals. Plenum, London (1972).

[4] M.T. Hutchings. Solid State Phys. **16**, 227. Seitz and Turnbull (eds.) Academic Press (1964).

[5] P. Fulde in Handbook on the Physics and Chemistry of Rare Earths. Vol. 2, eds. K.A. Gschneidner, Jr., Le Roy Eyring. North-Holland, Amsterdam (1979).

[6] P. Fulde. In Spin Waves and Magnetic Excitations. Vol. 22.1. Eds. A.S. Borovik-Romanov and S.K. Sinha, North Holland, Amsterdam (1988).

[7] M.A. Ruderman, C. Kittel. Phys. Rev. **96**, 99 (1954).

[8] B. Hälg and A. Furrer. Phys. Rev. **B34**, 6258 (1986).

[9] A.S. Borovik-Romanov and S.K. Sinha (eds.). Spin Waves and Magnetic Excitations. North Holland, Amsterdam (1988).

[10] P.A. Lindgård. Spin Excitations. Monography to be published (1989).

[11] B.T. Matthias, M. Peter, H.J. Williams, A.M. Clogston, E. Corenzweit and R.C. Sherwood. Phys. Rev. Lett. 5, 542 (1960).

[12] A. Blandin and J. Friedel. J. Phys. Radium **19**, 573 (1958).

[13] P.W. Anderson. Phys. Rev. **124**, 41 (1961).

[14] C.M. Varma in Moment Formation in Solids. Ed. W.J.L. Buyers. Plenum (1984).

[15] C.M. Varma. Comments Solid State Phys. **11**, 221 (1985).

[16] G.G. Lonzarich. J. Magn. Mat. **45**, 43 (1984).

[17] L. Taillefer. Spin Fluctuations in itinerant electron ferromagnets. Phd Thesis. Cavendish Laboratory, Cambridge (1986).

[18] J. Hubbard. Proc R. Soc. **A276**, 238 (1963). For a good introduction, see Chapter 9.3 of S.W. Lovesey. Theory of Neutron Scattering from Condensed Matter. Vol. 2. Clarendon Press, Oxford (1984).

[19] Toru Moriya. Spin Fluctuations in Itinerant Electron Magnetism. Springer Verlag Berlin, Heidelberg (1985).

[20] S.W. Lovesey. Theory of neutron scattering from condensed matter. Vols. 1 and 2. Clarendon Press, Oxford (1984).

[21] K. Ueda. J. Phys. Soc. Jpn. **44**, 1533 (1978).

[22] W.M. Loomer. Proc. Phys. Soc. London **86**, 489 (1962)

[23] A.M. Overhauser. Phys. Rev. **128**, 1437 (1962).

[24] For the experimental aspects of chromium, see B.H. Grier, G. Shirane and S.A. Werner. Phys. Rev. **B31**, 2892 (1985) and references therein.

[25] G.G. Lonzarich and L. Taillefer. J. Phys. **C18**, 4339 (1985).

[26] R.D. Parks. Valence instabilities and related narrow band phenomena. Plenum Press, New York (1977).

[27] J.K. Boucherle, J. Floquet, C. Lacroix, J. Rossat Mignod (eds.). Proceedings of the International Conference on Anomalous Rare Earths and Actinides. J. Magn. Magn. Mat. **63** and **64** (1987).

[28] J.R. Schrieffer and P.A. Wolff. Phys. Rev. **149**, 491 (1966).

[29] K.G. Wilson. Rev. Mod. Phys. **47**, 773 (1975).

[30] B.A. Jones, C.M. Varma, J.W. Wilkins. Phys. Rev. Lett. **61**, 125 (1988) and references therein.

[31] P. Coleman and N. Andrei. Article presented at the International Conference on Crystal Field Effects and Heavy-Fermion Physics. Frankfurt, July (1988).

[32] L.D. Landau and E.M. Lifshitz. Statistical Physics. Pergamon Press, Oxford (1970).

[33] P. Nozieres. J. of Low Temp. Phys. **17**, 31 (1974).

[34] G.R. Stewart. Rev. Mod. Phys. **56**, 755 (1984).

[35] K. Andres, J.E. Graebner and H.R. Ott, Phys. Rev. Lett. **35**, 1779 (1975).

[36] K.H. Mader and W.M. Swift. J. Phys. Chem. Solids **29**, 1759 (1968).

[37] T. Fujita, K. Satoh, Y. Onuki and T. Komatsubaru. J. Magn. Magn. Mater. **47** and **48**, 66 (1985).

[38] G.R. Stewart, Z. Fisk and M.S. Wire. Phys. Rev. B30, 482 (1984).
[39] R.J. Trainer, M.B. Brodsky and H.V. Culbert. Phys. Rev. Lett. 34, 1019 (1975).
[40] M.B. Brodsky. J. Phys. Colloq. 40 (C4), 147 (1979).
[41] H.R. Ott, H. Rudigier, E. Felder, Z. Fisk, J.D. Thompson. Phys. Rev. B35, 1452 (1987).
[42] Z. Fisk, G.R. Stewart, J.O. Willis, H.R. Ott and F. Hulliger. Phys. Rev. B30, 6360 (1984).
[43] H.R. Ott, H. Rudigier, E. Felder, Z. Fisk and B. Batlogg. Phys. Rev. Lett. 55, 1595 (1985).
[44] H.J. van Daal, K.H.J. Buschow, P.B. van Aken and M.H. van Maaren. Phys. Rev. Lett. 34, 1457 (1975).
[45] M. van Sprang, A. de Visser, J.J.M. Franse, A. Menovsky and A.J. Dirkmaat. J. Magn. Magn. Mat. 63 and 64, 393 (1987).
[46] A.P. Ramirez, B. Batlogg, E. Bucher, and A.S. Cooper. Phys. Rev. Lett. 57, 1072 (1986).
[47] A.I. Goldman, G. Shirane, G. Aeppli, B. Batlogg and E. Bucher. Phys. Rev. B34, 6564 (1986).
[48] H.R. Ott, H. Rudigier, P. Delsing, and Z. Fisk. Phys. Rev. Lett. 52, 1551 (1984).
[49] H.R. Ott and Z. Fisk. In: Handbook on the Physics and Chemistry of the Actinides. Edited by A.J. Freeman and G.H. Lander. Elsevier Science Publishers, B.V. (1987).
[50] F. Steglich, J. Aarts, C.D. Bredl, W. Lieke, D. Meschede, W. Franz and J. Schäfer. Phys. Rev. Lett. 43, 1892 (1979).
[51] B. Batlogg, J.P. Remeika, A.S. Cooper and Z. Fisk. J. Appl. Phys. 55, 2001 (1984).
[52] G.R. Stewart, Z. Fisk, J.O. Willis and J.L. Smith. Phys. Rev. Lett. 52, 679 (1984).
[53] P.H. Frings. Thesis. University of Amsterdam. Unpublished (1984), and P.H. Frings, J.J.M. Franse, F.R. de Boer and A. Menovsky. J. Magn. Magn. Mater. 31-34, 240 (1983).
[54] G. Aeppli, E. Bucher, C. Broholm, J.K. Kjems, J. Baumann and J. Hufnagl. Phys. Rev. Lett. 60, 615 (1988).
[55] T.T.M. Palstra, A.A. Menovsky, J. van den Berg, A.J. Dirkmaat, P.H. Kes, G.J. Nieuwenhuys, and J.A. Mydosh. Phys. Rev. Lett. 55, 2727(1985).
[56] H.R. Ott, H. Rudigier, E. Felder, Z. Fisk and J.L. Smith. Phys. Rev. B33, 126 (1986).
[57] A. Murasik, S. Ligenza and A. Zygmunt. Phys. Stat. Sol. (a) 23, K. 163 (1974).
[58] P.H. Frings, B. Renker and C. Vettier. J. Magn. Magn. Mater. 63-64, 202 (1987).
[59] D.L. Martin. Phys. Rev. 124, 438 (1961).
[60] D.F. Dubois. Ann. Phys. (NY) 7, 174 (1959) and Ann. Phys. (NY) 8, 24 (1959).
[61] K.A. Gschneidner, Jr. In: Valence Instabilities and Related Narrow Band Phenomena. R.D. Parks (ed.). Plenum Press, New York (1977) and references therein.
[62] K. Winzer. Solid State Commun. 16, 521 (1975).
[63] A.J. Freeman and G.H. Lander (eds.). Handbook on the Physics and Chemistry of the Actinides. Elsevier Science Publishers, B.V. (1985).
[64] F. Gerken and J. Schmidt-May. J. Phys. F. 13, 1571 (1983).
[65] H.H. Hill. P. 2 in Plutonium 1970 and Other Actinides, edited by W.H. Miner. AIME, New York (1970).
[66] W.J.L. Buyers and T.M. Holden. In: Handbook on the Physics and Chemistry of the Actinides. Elsevier Science Publishers, B.V. (1985).
[67] H.R. Ott, K. Andres and P.H. Schmidt. Physica 102B + C (1980) 148.
[68] W.J.L. Buyers, A.F. Murray, T.M. Holden, E.C. Svensson, P. de V. Du Plessis, G.H. Lander, and O. Vogt. Physica 102 B + C, 291 (1980).
[69] P.A. Lee, T.M. Rice, J.W. Serene, L.J. Sham and J.W. Wilkins. Comments Cond. Mat. Phys. 12, 99 (1986) and references therein.
[70] A concise introduction to neutron scattering is G.L. Squires, Introduction to the Theory of Thermal Neutron Scattering. Cambridge University Press. Cambridge (1978).
[71] The form factor can be more complicated than this with its maximum occurring at finite $\varkappa$ due to cancellation of spin and orbital moment. M. Wulff, G.H. Lander, J. Rebizant, J.C. Spirlet, B. Lebech, C. Broholm, P.J. Brown. Phys. Rev. B37, 5577 (1988), and M. Wulff, G.H. Lander, B. Lebech and A. Delapalme (1988) to be published.

[72] Appendix B of S.W. Lovesey. Theory of Neutron Scattering from Condensed Matter. Clarendon Press, Oxford (1984) gives an excellent introduction to generalized susceptibility and response functions.
[73] R.M. Moon, T. Riste and W.C. Koehler. Phys. Rev. 181, 920.
[74] J.J.M. Franse. J. Magn. Magn. Mater. 31-34, 819 (1983).
[75] P.H. Frings, J.J.M. Franse, F.R. de Boer, and A. Menovsky. J. Magn. Magn. Mater. 31-34, 240 (1983).
[76] A.I. Goldman, G. Shirane, G. Aeppli, E. Bucher, and J. Hufnagl. Phys. Rev. B36, 8523 (1987).
[77] M.R. Norman, T. Oguchi and A.J. Freeman. Preprint (1988).
[78] A. de Visser, J.C.P. Klaase, M. van Sprang, J.J.M. Franse, A. Menovsky, and T.T.M. Palstra. J. Magn. Magn. Mater. 54-57, 375 (1986).
[79] G.R. Stewart, A.L. Giorgi, J.O. Willis, and J. O'Rourke. Phys. Rev. B34, 4629 (1986).
[80] R. Heffner. In: Proceedings of the Fifth International Conference on Valence Fluctuations. Bangalore, India 1987. Edited by S. Malik and K. Gupta.
[81] C. Broholm, J.K. Kjems, G. Aeppli, E. Bucher and W.J.L. Buyers. In: Proceedings of the International Workshop on Magnetic Excitations and Fluctuations II. Springer Verlag Berlin (1987).
[82] G. Aeppli, E. Bucher, C. Broholm, J.K. Kjems, J. Baumann and J. Hufnagl. Phys. Rev. Lett. 60, 615 (1988).
[83] D.J. Bishop, C.M. Varma, B. Batlogg, E. Bücher, Z. Fisk and J.L. Smith. Phys. Rev. Lett. 53, 1009 (1984).
[84] Z. Fisk, H.R. Ott, T.M. Rice and J.L. Smith. Nature 320, 124 (1986).
[85] V. Müller, Ch. Roth, D. Maurer, E.W. Scheidt, K. lüders, E. Bücher and H.E. Bömmel. Phys. Rev. Lett. 58, 1224 (1987).
[86] B.S. Shivram, T.F. Rosenbaum and D.G. Hinks. Phys. Rev. Lett. 57, 1259 (1986).
[87] R.N. Kleinman, P.L. Gammel, E. Bucher and D.J. Bishop. Preprint (1988).
[88] C.M. Varma. Bull. Am. Phys. Soc. 29, 404 (1984).
[89] P.W. Anderson. Phys. Rev. B30, 1549 (1984).
[90] K. Miyake, S. Schmitt-Rink and C.M. Varma. Phys. Rev. B34, 6554 (1986).
[91] S. Schmitt-Rink, K. Miyake and C.M. Varma. Phys. Rev. Lett. 57, 2575 (1986).
[92] B. Arfi, H. Bahlouli and C.J. Pethick. Preprint (1988).
[93] C. Stassis, J. Arthur, C.F. Majkrzak, J.D. Axe, B. Batlogg, J. Remeika, Z. Fisk, J.L. Smith, and A.S. Edelstein. Phys. Rev. B34, 4382 (1986).
[94] C.G. Shull and F.A. Wedgwood. Phys. Rev. Lett. 16, 513 (1966).
[95] T.J. Heal and G.T. Williams, Acta. Crystallog. 8, 494 (1955).
[96] E. Bucher, J. Baumann and J. Hufnagl of the University of Konstanz, D-7750 Konstanz, FRG.
[97] B.C. Frazer, G. Shirane, D.E. Cox and C.E. Olsen. Phys. Rev. 140, A1448 (1965).
[98] W.F. Brinkman and S. Engelsberg. Phys. Rev. 169, 417 (1968) and references therein.
[99] G.G. Lonzarich. J. Magn. Magn. Mater. 54-57, 612 (1986).
[100] R. Konno and Toru Moriya. Quantitative aspects of the theory of nearly ferromagnetic metals. Technical report of ISSP. Ser. A No. 1789 (1987).
[101] L. Taillefer, R. Newbury, G.G. Lonzarich, Z. Fisk and J.L. Smith. J. Magn. Magn. Mater. 63-64, 372 (1987) and Poster presented at the fifth ICVF Bangalore, January (1987).
[102] P.H.P. Reinders, M. Springford, P.T. Coleridge, R. Boulet and D. Ravot. Phys. Rev. Lett. 57, 1631 (1986).
[103] P.H. Frings and A.A. Menovsky. Private communication.
[104] A. de Visser. PhD thesis. University of Amsterdam. (1986). Unpublished.
[105] After our publication of the Antiferromagnetic order in UPt_3 L. Taillefer et al. have found small anomalies in the heat capacity of de Haas van-Alpen quality single crystals at 5 K.
[106] Z. Fisk, D.W. Hess, C.J. Pethick, D. Pines, J.L. Smith, J.D. Thompson and J.O. Willis. Science 239, 33 (1988).
[107] E.S. Makarov and S.I. Vinogradov. Kristallografiya 1, 634 (1956).
[108] C.L. Vold and D.T. Peterson. Ames Laboratory Research and Development Report IS 246 (1961).
[109] A. Iandelli and A. Palenzona. J. Less Common Met. 12, 1333 (1967).

[110] A. Misiuk, J. Mulak and A. Czopnik. Bulletin des Academie Polonaise des Sciences. Serie des sciences chimiques. Vol. XXI 6, 487 (1973).
[111] D.E. Cox, G. Shirane, S.M. Shapiro, G. Aeppli, Z. Fisk, J.L. Smith, J.K. Kjems and H.R. Ott. Phys. Rev. B33, 3614 (1986).
[112] D.E. Cox, G. Shirane, S.M. Shapiro, G. Aeppli, Z. Fisk, J.L. Smith, J. Kjems, and H.R. Ott (1985) unpublished.
[113] U. Walter, M. Loewenhaupt, E. Holland-Moritz and W. Schlabitz. Phys. Rev. B36, 1981 (1987).
[114] T. Siegrist, M. Oliver, S.P. McAlister, and R.W. Cochrane. Phys. Rev. B33, 4370 (1986).
[115] C. Broholm, J.K. Kjems, G. Aeppli, Z. Fisk, J.L. Smith, S.M. Shapiro, G. Shirane, and H.R. Ott. Phys. Rev. Lett. 58, 917 (1987).
[116] M. Wulff, C. Broholm, J.K. Kjems, Z. Fisk, J.L. Smith, and H.R. Ott. (1986) (unpublished).
[117] G.E. Bacon. Neutron Diffraction. Clarendon Press, Oxford (1975). Third Edition.
[118] J. Als-Nielsen and J.K. Kjems. Risø National Laboratory Memorandum No. 1802 (1975). Available on request.
[119] H. Patterson, G. Shirane and R.A. Cowley. Brookhaven National Laboratory Research Memo G 29 (1976) unpublished.
[120] Y. Ishikawa, G. Shirane, J.A. Tarvin and M. Kohgi. Phys. Rev. B16, 4956 (1977).
[121] S. Liang, B. Doucot and P.W. Anderson. Phys. Rev. Lett. 61, 365 (1988).
[122] C.R. Fincher, G. Shirane and S.A. Werner. Phys. Rev. B24, 1312 (1981) and references therein.
[123] A. Auerbqach, Ju H. Kim, K. Levin, and M.R. Norman. Phys. Rev. Lett. 60, 623 (1988).
[124] R.J. Birgeneau and S.M. Shapiro. In Valence Instabilities and Related Narrow-Band Phenomena edited by R.D. Parks. Plenum Press, New York (1977).
[125] G. Aeppli, E. Bucher and G. Shirane. Phys. Rev. B32, 7579 (1985).
[126] An essentially similar model was suggested by G. Aeppli, H. Yoshizawa, Y. Endoh, E. Bucher, J. Hufnagl, Y. Onuki, and T. Komatsubara. Phys. Rev. Lett. 57, 122 (1986).
[127] J. Als-Nielsen. In: Phase Transitions and Critical Phenomena. Eds. C. Domb and M.S. Green. Academic Press (1976).
[128] M.B. Maple, J.W. Chen, Y. Dolichoouch, T. Kohara, C. Rossel, M.S. Torikachvili, M.W. McElfresh, and J.D. Thomson. Phys. Rev. Lett. 56, 185 (1986).
[129] W. Schlabitz, J. Baumann, B. Pollit, U. Rauchachwalbe, H.M. Mayer, U. Ahlheim, and C.D. Bredl. Z. Phys. B62, 171 (1986).
[130] A. de Visser, F.E. Kayzel, A.A. Menovsky, J.J.M. Franse, J. van den Berg, and G.J. Nieuwenhuys. Phys. Rev. B 34, 8168 (1986).
[131] F.R. De Boer, J.J.M. Franse, E. Louis, A.A. Menovsky, J.A. Mydosh, T.T.M. Palstra, U. Rauchswalbe, W. Schlabitz, F. Steglich, and A. de Visser. Physica (Amsterdam) 138B, 1 (1986).
[132] M.W. McElfresh, J.D. Thompson, J.O. Willis, M.B. Maple, T. Kohara, and M.S. Torikachvili. Phys. Rev. B 35, 43 (1987).
[133] A. de Visser, F.R. de Boer, A.A. Menovsky, and J.J.M. Franse. Solid State Comm. 64, 527 (1987).
[134] T.T.M. Palstra, A.A. Menovsky and J.A. Mydosh. Phys. Rev. B33, 6527 (1986).
[135] U. Walter, C.-K. Loong, M. Loewenhaupt, and W. Schlabitz. Phys. Rev. B 33, 7875 (1986).
[136] T.T.M. Palstra. Ph.D thesis. University of Leiden (1986) unpublished.
[137] C. Broholm, J.K. Kjems, W.J.L. Buyers, P. Matthews, T.T.M. Palstra, A.A. Menovsky, and J.A. Mydosh. Phys. Rev. Lett. 58, 1467 (1987).
[138] A.A. Menovsky and J.J. M. Franse. J. Cryst. Growth 65, 286 (1983).
[139] C. Broholm et al. to be published (1989).
[140] K. Hirakawa and H. Yoshizawa. J. Phys. Soc. Jap. 46, 448 (1979).
[141] See also H. Lin, T. Mason, W.J.L. Buyers, C. Broholm, J.K. Kjems, A.A. Menovsky and J.A. Mydosh. In: Proc. of 6th International Conference on Crystal Field Effects and Heavy Fermion Physics. Frankfurt July 1988.
[142] P.A. Lindgård. In Spin Waves and Magnetic Excitations. Vol. 22.1. Eds. A.S. Borovik-Romanov and S. K. Sinha,, North Holland, Amsterdam (1988).
[143] G.J. Nieuwenhuys. Phys. Rev. B 35, 5260 (1987).
[144] T.M. Holden, J.A. Jackman, W.J.L. Buyers, K.M. Hughes, M.F. Collins, P. de V. Duplessis and O. Vogt. J. Magn. Magn. Mater. 63 and 64, 155 (1987).

[145] A. Fetter and Walecka. Quantum theory of many-particle systems. McGraw-Hill (1971).

[146] This distinction was realized in discussions with Dr. G. Shirane.

[147] H. Lin, T. Mason, W.J.L. Buyers, C. Broholm, J.K. Kjems, A.A. Menovsky, J.A. Mydosh. Proc. of the 6th Int. Conf. on Crystal Field Effects and Heavy Fermion Physics, Frankfurt, FRG (1988).

[148] T.M. Holden, W.J.L. Buyers, E.C. Svensson and H.G. Purwins. In Crystal Field Effects in Metals and Alloys. Ed. A. Furrer. Plenum Press, New York (1977).

[149] O. Steinsvoll, C.F. Majkrzak, G. Shirane and J. Wicksted. Phys. Rev. B30, 2377 (1984).

[150] See N.J. Chesser and J.D. Axe. Acta Crystallogr. Sect. A29, 160 (1973) and references therein.

[151] T. Izuyama, D.J. Kim and R. Kubo. J. Phys. Soc. Jap. 18, 1025 (1963).

[152] P. Bak. Ph.D thesis. Technical University of Denmark. Risø Report No. 312 (1974) available on request from: Library, Risø National Laboratory, 4000 Roskilde, Denmark.

[153] I.S. Gradshteyn and I.W. Ryzhik. Table of integrals, series and products (1965). P. 569 formula BI ((354)) (6) 4.319. There is a sign error in the formula: $-\pi$ should read π.

[154] Formula 16.15 of M.R. Spiegel. Mathematical Handbook of Formulas and Tables. Schaums Outline Series, McGraw Hill, New York (1968).

[155] This has also been pointed out by R. Konno and T. Mariya. Quantitative aspects of the theory of nearly ferromagnetic metals. Technical report of ISSP. Ser. A No. 1789 (1987).

[156] B. Lebech and M. Nielsen. Intensity and Resolution of a general space. Neutron Diffraction Conference Petten (1975).

where

$$M_{cell} = \sum_{d} M_d \tag{A.10}$$

We may thus write

$$u_s(0) = \hat{u}_s / \sqrt{M_{cell}} \tag{A.11}$$

where u_s is the vector of unit length along the displacement associated with the mode s. Inserting this in (A.6) we get

$$\frac{e_{d_s}}{\sqrt{M_d}} = \frac{\hat{u}_s}{\sqrt{M_{cell}}} \tag{A.12}$$

finally inserting this in (A.2) we get

$$\left(\frac{\partial^2\sigma}{\partial\Omega\sigma E}\right)_{coh} = \frac{k_f}{k_i}\frac{(2\pi)^3}{2v_o}\cdot\frac{(\kappa\cdot 1m)^2}{M_{cell}} \mid F(\kappa)\mid^2 \cos^2\beta_s \times \sum_{\tau q_s}\frac{\langle n(\hbar\omega_s(q))+1\rangle}{\omega_s(q)}\delta(\omega-\omega_s(q))\delta(\kappa-q-\tau) \tag{A.13}$$

where

$$F(\kappa) = \sum_{d}\bar{b}_d \exp(-W_d)\exp(i\kappa\cdot d) \tag{A.14}$$

and β_s is the angle between κ and u_s.

We have not quantitatively stated what we mean by the long wavelength limit. How small q it is necessary to go to for (A.13) to be a good approximation to the cross section depends on the symmetry of the excited phonon mode, the crystal structure, the variance of atomic masses within a unit cell and their associated scattering lengths. Scattering from high symmetry phonons in simple structures presumably follows (A.13) closely in an appreciable part of the Brillouin zone. In general it is a good practice to measure the same phonon as a function of q so one may extrapolate the integrated intensity to q = 0.

We now calculate the quantity $\tilde{I}(\kappa_o, E_o)$ of A.1, the monitor-normalized scattered intensity originating from coherent creation of the phonon mode, s, at the reciprocal lattice point τ.

$$\tilde{I}(\kappa_o, E_o) = k_i \int d\kappa dE \; \frac{k_f}{k_i}\cdot\frac{(2\pi)^3}{2v_o}\cdot\frac{(\kappa\cdot 1m)^2}{M_{cell}}\cdot \mid F(\kappa)\mid^2\cdot\cos^2\beta_s \times\sum_{q}\frac{\langle n(\hbar\omega_s(q))+1\rangle}{\omega_s(q)}\delta\left(\frac{E}{\hbar}-\omega_s(q)\right)\delta(\kappa-q-\tau) \times R(\kappa_o, E_o, \kappa, E) \tag{A.15}$$

Neglecting slowly-varying factors in integrations and summations

$$\tilde{I}(\kappa_o, E_o) \simeq k_f \cdot \frac{(2\pi)^3}{2v_o} \frac{(\kappa \cdot 1m)^2}{M_{cell}}$$

$$\cdot |F(\kappa)|^2 \cdot \cos^2 \beta_s \frac{(n(\hbar\omega_s(\kappa_o)) + 1)}{\omega_s(\kappa_o)}$$

$$\sum_q \int d\kappa dE \, \delta\left(\frac{E}{\hbar} - \omega_s(q)\right) \delta(\kappa - q - \tau) R(\kappa_o, E_o, \kappa, E) \tag{A.16}$$

Transforming the q summation to an integration by introducing the q state density $V/(2\pi)^3$

$$I(\kappa_o, E_o) \simeq k_f \cdot \frac{(2\pi)^3}{2v_o} \frac{(\kappa \cdot 1m)^2}{M_{cell}}$$

$$\cdot |F(\kappa)|^2 \cdot \cos^2 \beta_s \frac{(n(\hbar\omega_s(\kappa_o)) + 1)}{\omega_s(\kappa_o)}$$

$$\times \hbar \cdot \frac{V}{(2\pi)^3} \int dq R(\kappa_o, E_o, q + \tau, \hbar\omega_s(q)) \tag{A.17}$$

where $N = V/v_0$ is the number of unit cells in the crystal giving rise to the scattering.

This is a function which is strongly peaked whenever κ_0, E_0 lie on the dispersion surface given by $\hbar\omega_s(\kappa_0)$. Integrating this peak as a function of energy at fixed κ_0 one may experimentally determine the volume of the resolution function:

$$\int dE \tilde{I}(\kappa_o, E) = \frac{(\hbar\kappa)^2/2m}{\hbar\omega_s(\kappa_o)} \left(\frac{M_{cell}}{m}\right)^{-1} |F(\kappa)|^2 \cos^2 \beta_s (n(\hbar\omega_s(\kappa_o)) + 1)$$

$$\times k_f \cdot N \cdot B(\kappa_o, \hbar\omega_s(\kappa_o)) \tag{A.18}$$

where m is the neutron mass and

$$B(\kappa_o, E_o) = \int dq dE \, R(\kappa_o, E_o + E, q + \tau, \hbar\omega_s(q))$$

$$\simeq \int dq dE \, R(\kappa_o, E_o, q + \tau, \hbar\omega_s(q) - E)$$

$$= \int dq dE \, R(\kappa_o, E_o, q, E) \tag{A.19}$$

We have neglected the variation of the resolution function over the extent of the energy integration. (A.18) enables us to relate the energy integrated phonon intensity to $N \cdot B(\kappa_0, E_0)$ which, as we shall see later, occurs as a product to the monitor-normalized scattered intensity of eg. diffuse magnetic scattering. A similar formula may be deduced for the integrated monitor normalized scattered intensity as a function of momentum transfer at fixed energy transfer:

$$\int d\kappa \tilde{I}(\kappa_o + \kappa\hat{\kappa}, \hbar\omega_s(\kappa_o))$$

$$= \frac{(\hbar\kappa_o)^2/2m}{\hbar\omega_s(\kappa_o)} \left(\frac{M_{cell}}{m}\right)^{-1} |F(\kappa)|^2 \cos^2 \beta_s (n(\hbar\omega_s(\kappa_o)) + 1)$$

$$\times \frac{1}{|\nabla_{\hat{\kappa}} \hbar\omega_s(\kappa_o)|} k_f \cdot N \cdot B(\kappa_o, \hbar\omega_s(\kappa_o)) \tag{A.20}$$

where $\nabla_{\hat{\kappa}} \hbar\omega_s(\kappa_o)$ is the slope of the dispersion surface in the direction of the integration, $\hat{\kappa}$.

A.3. Magnetic Scattering

In terms of the generalized susceptibility, the magnetic scattering cross section may be written [20]

$$\frac{\partial^2\sigma}{\partial\Omega\partial E} = \frac{k_f}{k_i}\left(\frac{1}{2}r_o\right)^2 \mid F_m(\kappa)\mid^2 \exp(-2W(\kappa))$$

$$(n(\hbar\omega)+1)\frac{N_m}{\pi\mu_B^2} Im\{\chi_\kappa^\perp(\omega)\} \qquad (A.21)$$

$r_o = 0.54 \cdot 10^{-14}$ m is a constant, $|F_m(\varkappa)|^2$ is the magnetic formfactor which satisfies: $|F_m(0)|^2 = 1$, $\exp(-2W(\varkappa))$ is the Deby Waller factor, N_m is the number of magnetic unit cells, $\mu_B = 9.27 \cdot 10^{-24}$ JT^{-1} is the Bohr magneton. Im denotes the imaginary part and

$$\chi_\kappa^\perp(\omega) = \sum_{\alpha\beta}(\delta_{\alpha\beta} - \hat{\kappa}_\alpha\hat{\kappa}_\beta)\chi_\kappa^{\alpha\beta}(\omega) \qquad (A.22)$$

is the part of the generalized susceptibility arizing from dipolar operator components in the normal plane to $\varkappa$. α and β denote the three cartesian components. The generalized susceptibility is defined as [20].

$$\chi_\kappa^{\alpha\beta}(\omega) = \lim_{\varepsilon\to 0^+}\int_o^\infty dt \exp((i\omega t - \varepsilon)t)\phi_\kappa^{\alpha\beta}(t) \qquad (A.23)$$

$$\phi_\kappa^{\alpha\beta}(t) = \frac{(g\mu_B)^2}{N_m}\frac{i}{\hbar}\langle\left[S_\kappa^\alpha(t), S_{-\kappa}^\beta\right]\rangle \qquad (A.24)$$

$$S_\kappa^\alpha = \sum_{\boldsymbol{R}} \exp(-i\kappa\cdot\boldsymbol{R})S_{\boldsymbol{R}}^\alpha \qquad (A.25)$$

where

$$A(t) = \exp(-\mathcal{H}t/\hbar)A\exp(\mathcal{H}t/\hbar) \qquad (A.26)$$

g is the Landé factor of the effective spin $S_{\boldsymbol{R}}^\alpha$, is the Hamiltonian operator of the scattering system, $\chi_{\varkappa}^{\alpha\beta}(\omega)$ has units J/T^2/magnetic unit cell.

The formula is written in the form most suitable for atomic electrons with an effective spin operator given by g and $S_{\boldsymbol{R}}^\alpha$. The formula also holds for itinerant magnets when care is taken to define $S_{\boldsymbol{R}}^\alpha$ as an appropriate spin density operator. [20,151].

Inserting (A.21) in (A.1) and neglecting the variation of the slowly-varying factors over the extent of the resolution function we get

$$\tilde{I}(\kappa_o, E_o) = k_f\left(\frac{1}{2}r_o\right)^2 \mid F_m(\kappa)\mid^2 \exp(-2W(\kappa))(n(E_o)+1)\frac{N_m}{\pi\mu_B^2}$$

$$\times \int d\kappa dE\, Im\left\{\chi_{\kappa_o}^\perp((E+E_o)/\hbar)\right\} R(\kappa_o, E_o, \kappa, E) \qquad (A.27)$$

We treat 3 cases of magnetic scattering starting from this formula.

A.3.1. Broad Magnetic Response

If the susceptibility varies slowly as compared to the resolution function, we may move it outside the integration in (A.27):

$$\tilde{I}(\kappa_o, E_o) \simeq \left(\frac{1}{2}r_o\right)^2 |F_m(\kappa)|^2 \exp(-2W(\kappa)) \langle n(E_o)+1\rangle \frac{1}{\pi\mu_B^2} Im\{\chi^{\perp}_{\kappa_o}(E_o/\hbar)\} \times k_f \cdot N_m \cdot B(\kappa_o, E_o) \quad (A.28)$$

where $B(\kappa_0, E_0)$ is defined in (A.8). So from (A.7) we see that diffuse magnetic scattering is conveniently normalized to the integrated long wavelength acoustic phonon intensity.

A.3.2. Resolution Limited Inelastic Response: Renormalized Singlet-Singlet Transition

As an example of normalizing resolution limited inelastic magnetic scattering we calculate $\tilde{I}(\kappa_0, E_0)$ from a renormalized singlet-singlet transition.

As discussed in 4.3.1 the generalized susceptibility of the renormalized singlet-singlet for small $\beta\Delta$ may be approximated by

$$\chi^{zz}_{\kappa}(\omega) = \lim_{\varepsilon\to 0+}(g\mu_B)^2 \frac{2\Delta\,|\langle 0|J^z|1\rangle|^2 \tanh(\beta\Delta/2)}{\Delta^2_{\kappa} - (\hbar\omega + i\varepsilon)^2} \quad (A.29)$$

where $<0|J^z|1>$ is the transition matrix element,

$$\Delta_{\kappa} = \Delta(\Delta - 2J_{\kappa}(g\mu_B)^2\,|\langle 0|J^z|\rangle|^2 \tanh(\beta\Delta/2)) \quad (A.30)$$

where Δ is the splitting of states $|0>$ and $|1>$ and J_κ is the Fourier transformed exchange constant. Taking the imaginary part we get

$$Im\{\chi^{zz}_{\kappa}(\omega)\} = A\{\delta(\Delta_{\kappa} - \hbar\omega) - \delta(\Delta_{\kappa} + \hbar\omega)\} \quad (A.31)$$

where

$$A = \frac{\pi}{2}\frac{\Delta}{\Delta_{\kappa}}(g\mu_B)^2\,|\langle 0|J^z|1\rangle|^2 \tanh(\beta\Delta/2) \quad (A.32)$$

This is the only component to the susceptibility, so

$$Im\{\chi^{\perp}_{\kappa}(\omega)\} = \sum_{\alpha\beta}(\delta_{\alpha\beta} - \hat{\kappa}_{\alpha}\hat{\kappa}_{\beta})Im\left\{\chi^{\alpha\beta}_{\kappa}(\omega)\right\} = (1-\hat{\kappa}_z^2)Im\{\chi^{zz}_{\kappa}(\omega)\} \quad (A.33)$$

Inserting the excitation creation part of (A.31) in (A.27) we get

$$\tilde{I}(\kappa_o, E_o) = k_f \left(\frac{1}{2} r_o\right)^2 \cdot |F_m(\kappa)|^2 \exp(-2W(\kappa))$$
$$\times (n(E_o)+1) \frac{N_m}{\pi \mu_B^2} \cdot (1-\hat{\kappa}_z^2) A$$
$$\int d\kappa dE \delta(\Delta_\kappa - E) \cdot R(\kappa_o, E_o, \kappa, E)$$
$$= k_f \left(\frac{1}{2} r_o\right)^2 |F_m(\kappa)|^2 \exp(-2W(\kappa))$$
$$\times (n(E_o)+1) \frac{N_m}{\pi \mu_B^2} (1-\hat{\kappa}_z^2) A$$
$$\times \int d\kappa R(\kappa_o . E_o, \kappa, \Delta_\kappa) \qquad \text{(A.34)}$$

As in the phonon case we obtain a number which only depends essentially on the volume of the resolution function by performing an energy integration. Making the usual approximations we get

$$\int dE I(\kappa_o, E)$$
$$\simeq \left(\frac{1}{2} r_o\right)^2 \cdot |F_m(\kappa)|^2 \exp(-2W(\kappa))$$
$$\times (n(E_o)+1) \frac{N_m}{\pi \mu_B^2} (1-\hat{\kappa}_z^2) A$$
$$\times k_f \cdot N_m \cdot B(\kappa_o, \Delta_{\kappa_o}) \qquad \text{(A.35)}$$

A convenient form which may be immediately compared to (A.18) for normalization.

A.4. Bragg Scattering

The nuclear Bragg scattering cross section is

$$\frac{d^2\sigma}{\partial\omega \partial E} = N \cdot \frac{(2\pi)^3}{v_o} \cdot \sum_\tau \delta(\kappa - \tau) |F_N(\tau)|^2 \delta(E) \qquad \text{(A.36)}$$

where the nuclear unit cell structure factor is given by

$$F_N(\tau) = \sum_d \bar{b}_d \exp(i\tau \cdot d) \exp(-W_d(\tau)) \qquad \text{(A.37)}$$

From (A.1) we get the monitor-normalized intensity around the Bragg peak, τ.

$$\tilde{I}(\kappa_o, E_o) = N \frac{(2\pi)^3}{v_o} \cdot |F_N(\tau)|^2$$
$$k_i \int d\kappa dE \delta(\kappa - \tau) \delta(E) \cdot R(\kappa_o, E_o, \kappa, E)$$
$$= N \cdot \frac{(2\pi)^3}{v_o} \cdot |F_N(\tau)|^2 k_i \cdot R(\kappa_o, E_o, \tau, 0) \qquad \text{(A.38)}$$

So we obtain the obvious result that one may measure the instrumental resolution by mapping out the intensity around a Bragg peak. As compared with the various types of inelastic scattering, which are in general extended in several dimensions of momentum and energy space, Bragg peak intensity measures the value of the resolution function of a point. Good knowledge of the resolution function is therefore required when attempting to relate inelastic and Bragg scattering directly. Nuclear Bragg scattering is on the other hand ideal to normalize other elastic cross sections. Often the more reliable quantity to compare is the integrated intensity along a direction passing through the Bragg peak

$$\int d\kappa \tilde{I}(\tau + \kappa\hat{\kappa}, 0$$

$$= N \cdot \frac{(2\pi)^3}{v_o} \cdot | F_N(\tau) |^2 \cdot k_i \cdot \int d\kappa R(\tau + \kappa\hat{\kappa}, 0, \tau, 0) \qquad \text{(A.39)}$$

Such integrals can be calculated numerically in the general case using the formalism of [150] or approximately in certain limiting cases [156].

A.5. Normalization of Inelastic Magnetic Scattering In URu_2Si_2

We normalize the data of Figure 4.6.a to the phonon scattering of Figure A.1. Table A.1 illustrates the calculation of the factor characterizing the sensitivity of the experiment $k_f NB(\varkappa, E)$ of (A.18) or rewritten

$$k_f NB(\kappa_o, \hbar\omega_s(\kappa_o)) = \frac{\hbar\omega_s(\kappa_o) \int dE \tilde{I}(\kappa_o, E) \cdot (M_{cell}/m)}{\frac{(\hbar\kappa_o)^2}{2m} \cdot | F_m(\kappa_o) |^2 \cdot \cos^2\beta_s \cdot \langle n(\hbar\omega_s(\kappa_o)) + 1 \rangle} \qquad \text{(A.40)}$$

Figure A.1. Longitudinal acoustic phonons close to two strong nuclear Bragg peaks in URu_2Si_2. The data were taken at T = 77 K. The broken line is an estimate of the background. The solid lines are guides to the eye.

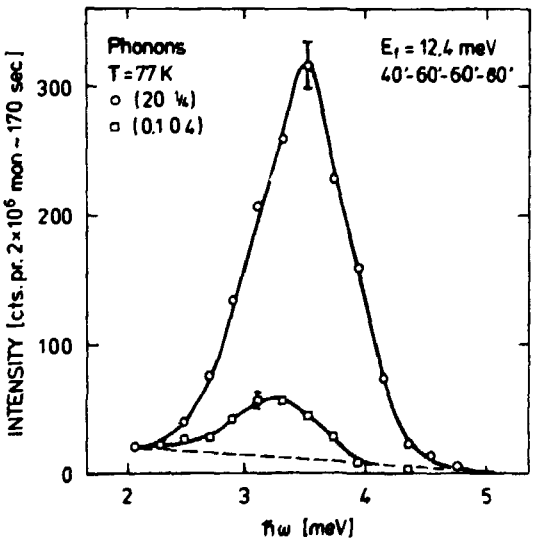

Table A.1. The following constants have been used in the above calculation: $a^* = 1.527\ Å^{-1}$, $c^* = 0.6576\ Å^{-1}$, $(M_{cell}/m) = 2(M_w/m) + 4(M_{Ru}/m) + 4(M_{Si}/m) = 2{\cdot}238 + 4{\cdot}101 + 4{\cdot}28 = 992$, $\hbar^2/2m = 2.072\ meV\,Å^2$, $k_B = 8.62{\cdot}10^{-2}\ meV/K$.

κ_o [r.l.u.]	$\lvert F(\kappa_o)\rvert^2$ [b]	κ_o [Å^{-1}]	$\cos^2\beta$ [unity]	$\Delta E{\cdot}\Sigma int(E)/mon$ [meV]	$(\hbar\kappa_o)^2/2m$ [meV]	$\omega_s(\kappa_o)$ [meV]	$k_BT = 1/\beta$ [meV]	$(1-\exp(-\beta\hbar\omega_s(\kappa_o)))^{-1}$ [unity]	$k_f N{\cdot}B(\kappa_o, \hbar\omega_s(K_o))$ [meV/b]
(20¼)	38.8	3.06	1.0	$1.44{\cdot}10^{-4}$	19.4	3.52	6.90	2.50	$2.7{\cdot}10^{-4}$
(0.104)	8.46	2.63	1.0	$2.52{\cdot}10^{-5}$	14.3	3.23	6.90	2.68	$2.5{\cdot}10^{-4}$

The spectrometer sensitivity changes only very little between (200) and (004) since $|(200)| \sim |(004)|$. This is also borne out by the last column of Table A.1. The magnetic scattering of Figure 4.6.a, which was taken at a monitor of $2{\cdot}10^7$, is separated into the sharp excitonic response and the overdamped high energy response. This separation is physically interesting and also natural from a technical point of view because the two parts of the response are influenced differently by resolution effects. The resolution limited response is normalized by (A.35). We determine the value of A by

$$
\begin{aligned}
A &= \frac{\int d\tilde{E}\tilde{I}(\kappa_o, E)\pi\mu_B^2}{\left(\frac{1}{2}r_o\right)^2 \mid F_m(\kappa)\mid^2 \exp(-2W(\kappa))(n(E_o)+1)(1-\hat{\kappa}_z^2)} \\
&\quad \times \frac{1}{k_f \cdot N_m \cdot B(\kappa_o, \overline{\Delta(\kappa_o)})} \\
&= \frac{1.24\cdot 10^{-4} meV \cdot \pi \cdot \mu_B^2}{\left(\frac{1}{2}\cdot 0.54\right)^2 b \cdot 0.93^2 \cdot 1 \cdot 1 \cdot 1} \\
&\quad \times \frac{1}{2.6\cdot 10^{-4} meV/b} = 24\mu_B^2
\end{aligned}
\qquad \text{(A.41)}
$$

We can now calculate the transition matrix element corresponding to the exciton cross section from A.32.

$$
\begin{aligned}
g\mu_B \mid \langle 0 \mid J^2 \mid 1\rangle \mid &\simeq \sqrt{\frac{2}{\pi}\frac{\Delta\kappa}{\Delta}A} \\
&\simeq \sqrt{\frac{2}{\pi}\frac{1.8}{2.6}24}\mu_B \\
&= 3\mu_B
\end{aligned}
\qquad \text{(A.42)}
$$

where Δ_κ and Δ have been taken from Figures 4.4 and 4.13.f, respectively. Both the Debye-Waller factor and the thermal population are close to 1 at T = 5 K. Furthermore we have without significant loss of accuracy neglected the variation of the spectrometer effectivity between the present momentum transfer (100) and that at which the phonons were measured. We have utilized that $N_m = N$ in this case since the magnetic unit cell is equivalent to the nuclear unit cell.

The high energy overdamped response is normalized using A.28:

$$
\begin{aligned}
Im\chi^{zz}_{\kappa}(\omega) &= \frac{\tilde{I}(\kappa,\hbar\omega)\cdot\pi\mu_B^2}{\left(\frac{1}{2}r_o\right)^2\cdot\mid F_m(\kappa)\mid^2\exp(-2W(\kappa))\langle n(\hbar\omega)+1\rangle} \\
&\quad\times\frac{1}{k_f\cdot N_m\cdot B(\kappa,\hbar\omega)} \\
&= \frac{\tilde{I}(\kappa,\hbar\omega)\cdot\pi\mu_B^2}{\left(\frac{1}{2}\cdot 0.54\right)^2 b\cdot 0.93^2\cdot 1\cdot 1}\cdot\frac{1}{2.6\cdot 10^{-4}meV/b} \\
&= 1.92\cdot 10^5\tilde{I}(\kappa,\hbar\omega)\cdot\mu_B^2/meV \qquad \text{(A.43)}
\end{aligned}
$$

from Figure 4.6.a

$$
\begin{aligned}
Im\{\chi_{(100)}(10meV)\} &= 1.92\cdot 10^5(100/2\cdot 10^7)\mu_B^2/meV \\
&= 1.0\mu_B^2/meV \\
&= 3\cdot 10^{-2}emu/mole \qquad \text{(A.44)}
\end{aligned}
$$

The total moment sum rule (1.3) enables us to make a crude estimate of the amount of moment participating in the quasielastic magnetic fluctuations. Since the response is polarized along c*

$$
Im\chi^{\perp}_{\vec{q}=(100)}(\omega) = Tr\chi_{q=100}(\omega) \qquad \text{(A.45)}
$$

We have not measured the detailed q dependence of the quasielastic response in the whole Brillouin zone, but from Figure 4.7 estimate is to occupy about $(\frac{1}{2})^3 \sim 10\%$ of this volume, so finally

$$
\begin{aligned}
\langle M^2\rangle &= 10\%\frac{1}{\pi}\int_{-\infty}^{\infty}d\omega\langle n(\hbar\omega)+1\rangle Im\{T_r\chi_q(\omega)\} \\
&= (0.6\mu_B)^2 \qquad \text{(A.46)}
\end{aligned}
$$

Appendix B: The Generalized Susceptibility of Exchange Enhanced Overdamped Magnetic Fluctuations

The RPA formula for the interacting susceptibility of a non-Bravais lattice can be written [152]

$$\chi_q(\omega) = \chi_o(\omega) + \chi_o(\omega)J(q)\chi_q(\omega) \tag{B.1}$$

where the matrices are indexed after each site in the unit cell. $\chi_o(\omega)$ is the diagonal matrix of non-interacting susceptibilities associated with each such site. $\mathbf{J(q)}$ is defined as

$$\{J(q)\}_{ij} = \sum_{R} J(R + d_i - d_j)\exp(q \cdot (R + d_i - d_j))$$

where R are all Bravais lattice vectors and d_i is the displacement vector to the i'th site, within the unit cell. $\mathbf{J(q)}$ is hermitian and thus has real eigenvalues, $\tilde{J}_{ii}(q)$. The eigenvectors of $\mathbf{J(q)}$,U, constitute a unitary transformation that diagonalizes (B.1). If each site is equivalent, i.e. $\chi_o(\omega) = \chi_o(\omega)\mathbf{1}$. The resulting diagonal interacting susceptibility is

$$\left\{\tilde{\chi}_q\right\}_{ii} = \frac{\chi_o(\omega)}{1 - \chi_o(\omega) \cdot \tilde{J}_{ii}(q)}$$

Note that in the antiferromagnetically ordered phase the assumption of site equivalency only holds for the longitudinal response. For the transverse response the cartesian structure of $\chi_0(\omega)$ becomes important due to the broken symmetry. To avoid further phenomenological parameters in this simplified model we, however, choose to ignore these complications.

The generalized susceptibility, whose imaginary part is a factor in the magnetic neutron scattering cross section is

$$\begin{aligned} \chi_q(\omega) &= \sum_{ij}\left\{\chi_q(\omega)\right\}_{ij} = e^T\chi_q(\omega)e \\ &= \tilde{e}^T\tilde{\chi}_q(\omega)\tilde{e} \\ &= \sum_{i}\left\{\tilde{\chi}_q(\omega)\right\}_{ii} |\,\tilde{e}_i\,|^2 \end{aligned} \tag{B.2}$$

where

$$\begin{aligned} e^T &= (1 \quad 1), \\ \tilde{e} &= U^{\dagger}e \end{aligned}$$

and $U^{\dagger}$ is the hermitian conjugate of U.

In the special case of a 2-sublattice model $\mathbf{J(q)}$ has the form:

$$\mathbf{J}(\mathbf{q}) = \begin{pmatrix} J_{\mathbf{q}} & J'_{\mathbf{q}} \\ J'^{*}_{\mathbf{q}} & J_{\mathbf{q}} \end{pmatrix}$$

so

$$\tilde{J} = \begin{pmatrix} J_{q}+ \mid J'_{q} \mid & 0 \\ 0 & J_{q}- \mid J'_{q} \mid \end{pmatrix}$$

and

$$U = \frac{1}{\sqrt{2}} \begin{pmatrix} 1 & 1 \\ e^{-i\phi q} & -e^{-i\phi q} \end{pmatrix}$$

where $\varphi_{\mathbf{q}}$ is the phase angle of $J'_{\mathbf{q}}$ which is complex in structures which do not have inversion symmetry

$$J'_{q} = \mid J'_{q} \mid \cdot \exp(i\phi_{\mathbf{q}})$$

from this we calculate

$$\tilde{e} = U^{\dagger} \begin{pmatrix} 1 \\ 1 \end{pmatrix} = \frac{1}{\sqrt{2}} \begin{pmatrix} 1 + e^{i\phi q} \\ 1 - e^{i\phi q} \end{pmatrix}$$

and for inserting in (B.2),

$$\mid \tilde{e}_i \mid^2 = 1 \pm \cos\phi_{\mathbf{q}}$$

and finally we obtain

$$\chi_{\mathbf{q}}(\omega) = \sum_{\pm} \frac{\chi_o(\omega)(1 \pm \cos\phi_{\mathbf{q}})}{1 - \chi_o(\omega)(J_{\mathbf{q}}\pm \mid J'_{\mathbf{q}} \mid)}$$

Inserting $\chi_o(\omega) = \chi_o\Gamma/(\Gamma - i\omega)$ we get

$$\begin{aligned} \chi_q(\omega) &= \sum_{\pm} \frac{\chi_o\Gamma(1 \pm \cos\phi_q)}{\Gamma_{q\pm} - i\omega} \\ &= \sum_{\pm} \frac{\chi_o\Gamma(1 \pm \cos\phi_q)}{\Gamma^2_{q\pm} + \omega^2}(\Gamma_{q\pm} + i\omega) \end{aligned} \qquad \text{(B.3)}$$

where

$$\Gamma_{q\pm} = \Gamma(1 - \chi_o(J_q \pm | J'_q |))$$

In particular the imaginary part of the generalized susceptibility occurring in (1.1) is

$$Im\{\chi_q(\omega)\} = \sum_{\pm} \frac{\chi_o \Gamma \omega (1 \pm \cos\phi_q)}{\Gamma^2_{q\pm} + \omega^2} \tag{B.4}$$

and the bulk susceptibility is

$$Re\{\chi_{q=0}(0)\} = \chi_o \cdot \sum_{\pm} \frac{\Gamma}{\Gamma_{q=0,\pm}} (1 \pm \cos\phi_{q=0}) \tag{B.5}$$

B.1. Application to the magnetic fluctuations in U_2Zn_{17}

In our model for U_2Zn_{17} we include only an intrasublattice coupling to the 4 nearest neighbours (see Figure 3.1) so for q = (hkl), where h, k and l are coordinates in the reciprocal lattice,

$$\mathbf{J_q} = J'_o \begin{pmatrix} 0 & e^{-i\frac{\pi}{3}} + e^{i\frac{\pi}{3}(h-k)} + e^{-i\frac{\pi}{3}(2h+k)} + e^{i\frac{\pi}{3}(h+2k)} \\ c.c. & 0 \end{pmatrix}$$

where J'_0 is negative for antiferromagnetic coupling. We get:

$$\begin{aligned} | J'_q |^2 = | J'_o |^2 [4 + 2 \; [& \cos\tfrac{2\pi}{3}(-h+k-l) + \cos\tfrac{2\pi}{3}(2h+k-l) \\ & + \cos\tfrac{2\pi}{3}(h+2k+l) + \cos 2\pi h \\ & + \cos 2\pi k + \cos 2\pi(h+k)]] \end{aligned}$$

$$\cos\phi_q = sign(J'_o) \frac{\cos\frac{2\pi}{3}l + \cos\frac{2\pi}{3}(h-k) + \cos\frac{2\pi}{3}(2h+k) + \cos\frac{2\pi}{3}(h+2k)}{| J'_q | / | J'_o |}$$

The imaginary part of the generalized susceptibility and the bulk susceptibility are now determined by insertion in (B.4) and (B.5), respectively.

In particular, we calculate some of these properties at the antiferromagnetic zone centre

$$J'_{q=(102)} = 4 | J'_o |$$

$$\cos\phi_{q=(102)} = \frac{1}{2}$$

$$Im\{\chi_{q=(102)}(\omega)\} = \sum_{\pm} \frac{\chi_o \Gamma \omega (1 \pm \frac{1}{2})}{[\Gamma(1 - \chi_o \cdot 4 | J'_o |)]^2 + \omega^2}$$

Note that this response diverges when $4\,\chi_o|J'_o| = 1$. The factor of 4 accounts for the four nearest neighbours to which each uranium atom is coupled. At $q = 0$ we get

$$|J'_{q=0}| = 4\,|J'_o|$$

$$\cos\phi_{q=0} = -1$$

$$Re\,\{\chi_{q=0}(0)\} = \chi_o \cdot \frac{2}{1 + 4\chi_o\,|J'_o|}$$

The factor of 2 in the expression for the bulk susceptibility arises since $\chi_q(\omega)$ is the generalized susceptibility for a magnetic unit cell consisting of 2 uranium atoms. Note that the antiferromagnetic exchange coupling reduces the bulk susceptibility as one would expect.

Appendix C: The Contribution of Magnetic Fluctuations to The Low Temperature Specific Heat

In contrast to the rigorous relations beteeen the generalized susceptibility and both the bulk susceptibility (1.2) and the total fluctuating moment (1.3), relating the generalized susceptibility to the free energy associated with the magnetic fluctuations requires knowledge of the Hamiltonian of the fluctuating system.

An approximative expression for the free energy associated with a relaxational magnetic fluctuation spectrum is [98,99,100]

$$F_{sf} = \sum_{\nu q} \int_0^\infty d\omega F_{osc}(\beta\hbar\omega) \frac{\Gamma_\nu(q)/\pi}{\omega^2 + \Gamma_\nu(q)^2} \qquad \text{(C.1)}$$

where

$$F_{osc}(\beta\hbar\omega) = \beta^{-1} ln[1 - \exp(-\beta\hbar\omega)] \qquad \text{(C.2)}$$

is the free energy of a harmonic oscillator and $\Gamma_\nu(q)$ is the relaxation frequency of the magnetic fluctuations with a modulation q and polarization ν. The contribution from zero-point fluctuations is omitted since our interest is the low temperature dependence of F_{sf}.

(C.1) is quite general, in particular we mention that if the low q expansion of $\Gamma_\nu(q)$ contains a term proportional to q, F_{sf} gives rise to the famous so-called paramagnon contribution to the specific heat $T^3 \ln(T/T_{sf})$ [98,99,100]. Here we shall only calculate the thermodynamic properties of a q independent relaxation response.

First of all in the high temperature limit of (C.1) we obtain

$$\lim_{\beta\hbar\Gamma \to 0} F_{sf} = 3 \lim_{\beta\hbar\omega \to 0} F_{osc}(\beta\hbar\omega) = 3\beta^{-1}$$

where the factor of 3 arises from the three modes of polarization, ν. (C.1) thus associates one degree of freedom with each polarization mode. In the case of magnetic fluctuations in an isotropic system with ground state degeneracy 2J + 1, a prefactor ⅓ ln(2J + 1) should be applied to (C.1) to give the correct high temperature limit of the free energy. Obviously in a complicated anisotropic system with unknown ground state degeneracy the prefactor to (C.1) is also unknown. It is however enough for our purpose here to note that the prefactor is of order 1.

For the simple q independent relaxation response the integral (C.1) may be calculated analytically:

$$\begin{aligned} F_{sf} &= \frac{3N}{\beta} \int_0^\infty d\omega \ln(1 - e^{-\beta\hbar\omega}) \frac{\Gamma/\pi}{\omega^2 + \Gamma^2} \\ &= \frac{3N}{\beta} \int_0^\infty dx \ln(1 - e^{-2\pi a x}) \cdot \frac{1}{1 + x^2} \\ &= \frac{3N}{\beta} \left[\frac{1}{2} ln 2a\pi + a(lna - 1) - ln\Gamma(a + 1) \right] \end{aligned} \qquad \text{(C.3)}$$

where N is the number of unit cells in the sample, $a = \beta\hbar\Gamma/2\pi$ and

$$\Gamma(z) = \int_0^\infty e^{-t}\, t^{z-1} dt \qquad [Re\ z > o]$$

is the gamma function. The last equation in (C.3) is due to reference [153].

In the low temperature limit: $a = \beta\hbar\Gamma/2\pi \rightarrow \infty$ we can expand (C.3) using Stirlings asymptotic series for $\Gamma(a + 1)$ [154]. We get

$$F_{sf} = -\frac{N}{4\beta a} = -\frac{\pi}{2}\frac{N}{\beta^2\hbar\Gamma} \tag{C.4}$$

We may now calculate the entropy and heat capacity from F_{sf}. Since we have already assumed $\beta\hbar\Gamma/2\pi \rightarrow \infty$ it is also reasonable in most cases to neglect the temperature dependence of Γ, and we obtain ($\beta = 1/k_B T$):

$$S_{sf} = -\frac{\partial F_{sf}}{\partial T} = \gamma \cdot T$$

$$C_{sf} = T\frac{\partial S}{\partial T} = S = \gamma T$$

where

$$\gamma = \pi\frac{N k_B^2}{\hbar\Gamma} = \frac{2.25 meV \cdot J/mol\ K^2}{\hbar\Gamma(in\ meV)}$$

the magnetic fluctuations with relaxation energies $\hbar\Gamma$ in the 1 - 10 meV range thus correspond to values of γ in the range 0.1 - 1 J/mole-K^2 (Table 1.1) [155].

Bibliographic Data Sheet **Risø-M-2731**

Title and authors

Magnetic fluctuations in Heavy Fermion Systems - A Neutron Scattering Study of UPt_3, U_2Zn_{17} and URu_2Si_2

Collin Leslie Broholm

ISBN	ISSN
87-550-1445-3	0418-6435

Dept. or group	Date
Physics Department	June 1989

Groups own reg. number(s)	Project/contract no.

Pages	Tables	Illustrations	References
79	9	37	158

Abstract (Max. 2000 characters)

Magnetic order and fluctuations in the heavy Fermion systems UPt_3, U_2Zn_{17} and URu_2Si_2 have been studied by neutron scattering. Single crystalline samples and triple-axis neutron-scattering techniques with energy transfers between 0 and 40 meV and energy resolutions between 0.1 meV and 4 meV have been employed.

UPt_3 developes an antiferromagnetically ordered moment of $(0.02 \pm 0.005)\ \mu_B$ below $T_N = 5$ K which doubles the unit cell in the basal plane and coexists with superconductivity below $T_c = 0.5$ K The magnetic fluctuations are relaxational, and enhanced at the antiferromagnetic zone center in a low-energy regime. The characteristic zone center relaxation energy is 0.3 meV. The temperature- and field-dependence of the antiferromagnetic order in the superconducting phase suggest a close relation between these two properties in UPt_3. U_2Zn_{17} has a broad spectrum of magnetic fluctuations, even below $T_N = 9.7$ K, of which the transverse part below 10 meV is strongly enhanced at the antiferromagnetic zone center. The system has an anomalously extended critical region and the antiferromagnetic phase transition seems to be driven by the temperature-dependence of an effective RKKY interaction, as anticipated theoretically. URu_2Si_2, a strongly anisotropic heavy Fermion system, has a high-energy regime of antiferromagnetically-correlated overdamped magnetic fluctuations. Below $T_N = 17.5$ K weak antiferromagnetic order, $\mu = (0.04 \pm 0.01)\mu_B$, with finite correlations along the tetragonal c axis, develops, along with a low-energy regime of strongly dispersive singlet-singlet excitations. Below $T_c = 1$ K antiferromagnetism coexists with superconductivity. A phenomenological model describing the exchange-enhanced overdamped magnetic fluctuations of heavy Fermion systems is proposed. Our experimental results are compared to the anomalous bulk properties of heavy Fermion systems, and to magnetic fluctuations in other metallic magnets.

Descriptors INIS/EDB

Available on request from Risø Library, Risø National Laboratory, (Risø Bibliotek, Forskningscenter Risø), P.O.Box 49, DK-4000 Roskilde, Denmark. Telephone + 45 42 37 12 12, ext. 2262. Telex 43 116. Telefax + 45 42 36 06 09.

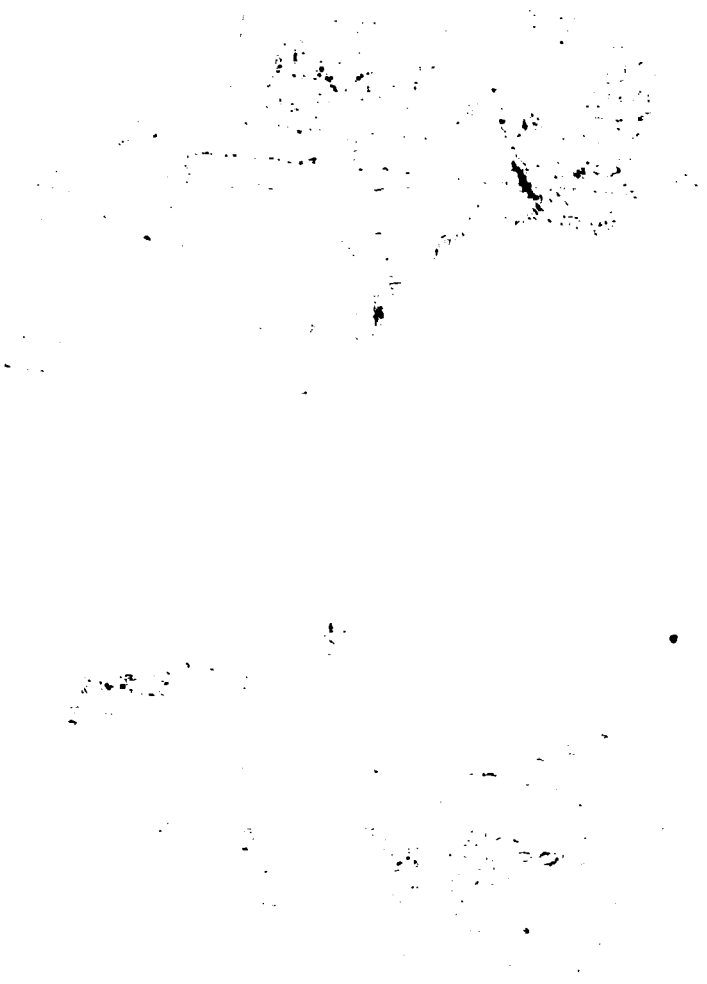

Available on exchange from:
Risø Library,
Risø National Laboratory,
P.O. Box 49, DK-4000 Roskilde, Denmark
Phone + 45 42 37 12 12, ext. 2268/2269,
Telex 43116, Telefax + 45 46 75 56 27

ISBN 87-550-1445-3
ISSN 0418-6435